E.O. Paton Electric Welding Institute of the National Academy of Science of Ukraine
International Association “Welding”

The Paton Welding Journal

10
2025

International Scientific-Technical and Production Journal ♦ Founded in January 2000 (12 Issues Per Year)

Address of Editorial Office:
E.O. Paton Electric Welding Institute, 11 Kazymyr Malevych Str., 03150, Kyiv, Ukraine
E-mail: office@paton.kiev.ua; https://paton.org.ua/en/

Address of Publisher:
International Association “Welding”, 11 Kazymyr Malevych Str., 03150, Kyiv, Ukraine
Tel.: (38044) 205 23 90, E-mail: patonpublishinghouse@gmail.com; journal@paton.kiev.ua
https://patonpublishinghouse.com/eng/journals/tpwj

The Journal was registered by the National Council of Ukraine on Television and Radio Broadcasting on 09.05.2024, carrier identifier R30-04569
ISSN 0957-798X (Print), ISSN 3041-2293 (Online)
DOI: https://doi.org/10.37434/tpwj, from #01, 2020 to now; DOI: https: //doi.org/10.15407/tpwj from #01, 2014 to #12, 2019.

Subscriptions, 12 issues per year:
348 Euro — annual subscription for the printed (hard copy) version, air postage and packaging included;
288 Euro — annual subscription for the electronic version (sending issues in pdf format or providing access to IP addresses).

Representative Offices of “The Paton Welding Journal”:

BRAZIL, Arc Dynamics
Address: Nova Iguacu, Rio de Janeiro, Brazil
Daniel Adolpho, Tel.: +55 21 9 6419 5703,
E-mail: dadolpho@arcdynamics.com.br

CHINA, China-Ukraine Institute of Welding, Guangdong Academy of Sciences
Address: Room 210, No. 363 Changxing Road, Tianhe, Guangzhou, 510650, China
Zhang Yupeng, Tel.: +86-20-61086791,
E-mail: patonjournal@gwi.gd.cn

BULGARIA, Bulgarian Welding Society
Address: Blvd. Asen Yordanov No.10, Sofia 1592, Bulgaria
Pavel Popgeorgiev, Tel.: +359 899 96 22 20,
E-mail: office@bws-bg.org

POLAND, PATON EUROPE Sp. z o. o.
Address: ul. Kapitałowa 4, 35-213, Rzeszów, Poland
Anton Stepakhno, Tel.: +38067 509 95 67,
E-mail: Anton.Stepakhno@paton.ua

The content of the Journal includes articles received from authors from around the world in the field of welding, cutting, cladding, soldering, brazing, coating, 3D additive technologies, electrometallurgy, material science, NDT and selectively includes translations into English of articles from the following journals, published in Ukrainian:

- «Avtomatychne Zvaryuvannya» (Automatic Welding), https://patonpublishinghouse.com/eng/journals/as;
- «Suchasna Elektrometalurhiya» (Electrometallurgy Today), https://patonpublishinghouse.com/eng/journals/sem;
- «Tekhnichna Diahnostyka ta Neruinivnyi Kontrol» (Technical Diagnostics & Nondestructive Testing), https://patonpublishinghouse.com/eng/journals/tdnk.

CONTENTS

ORIGINAL ARTICLES

*Translated Article(s) from “Avtomatychne Zvaryuvannya” (Automatic Welding), No. 4, 2025.

**Translated Article(s) from “Suchasna Elektrometalurhiya” (Electrometallurgy Today), No. 3, 2025.

Indexing: The electronic edition of the Journal is stored in the V.I. Vernadsky National Library of Ukraine (eVerLib), included in the OPEN UKRAINIAN CITATION INDEX database and international databases: CROSSREF, EBSCO, Google Scholar, INDEX COPERNICUS, ULRICHSWEB.

DOI: https://doi.org/10.37434/tpwj2025.10.01

PROSPECTS OF ULTRASOUND APPLICATION IN THE PRODUCTION OF DISPERSED GRANULES BY GAS AND PLASMA-ARC ATOMIZATION OF METAL MELTS AND COMPACT MATERIALS (REVIEW)

V.M. Korzhyk, O.S. Tereshchenko, D.V. Strohonov, O.I. Demianov, O.V. Ganushchak

E.O. Paton Electric Welding Institute of the NASU
11 Kazymyr Malevych Str., 03150, Kyiv, Ukraine

ABSTRACT

The technological features of ultrasonic vibrations utilizing for the atomization of microvolumes of metal melts in production technologies of dispersed spherical powders are considered, such as: gas atomization, ultrasonic atomization on sonotrode, plasma arc atomization by means of ultrasonic standing wave, electric arc atomization with the application of ultrasound to the wire, and plasma arc atomization with the application of ultrasonic vibrations to the atomized material. The influence of ultrasonic vibrations on the process of melt droplet formation and detachment for the aforementioned methods is analyzed. It is established that the superposition of ultrasound promotes a refinement of the initial melt droplets, intensifies dispersion due to putting additional pressure on the melt droplets, and, as a result, contributes to the narrowing of the particle size distribution. It has been found that among the analyzed approaches for obtaining spherical powders using high-frequency acoustic vibrations, the most promising is the technology of plasma arc atomization of wires and rods under the condition of applying ultrasound directly to the billets. An analysis of the efficiency and prospects of using plasma-arc atomization technologies with the introduction of ultrasonic vibrations into the atomized billets has been conducted, and it is hypothesized that this approach will allow increasing the yield of –63 μm fraction powders up to 80–90 %, which is promising for application in the production of powders for additive manufacturing technologies.

KEYWORDS: ultrasonic atomization, dispersion, plasma arc atomization, gas atomization, spherical powders, particle size distribution

INTRODUCTION

Influence of acoustic vibrations in the ultrasonic range is widely applied in engineering and industry to solve the tasks on non-destructive testing (flaw detection, determination of coating thickness, medical research), for ecological cleaning of materials in special baths for degreasing or deburring for the surface activation prior to coating deposition, for soldering and welding of metals and alloys, for dispersion of liquids in analytical equipment and of metal melts in powder production, in metal treatment for reducing the friction coefficient and in finish treatment of holes after drilling and milling [1]. In addition, ultrasound application in industrial technologies includes impact treatment of welds for relaxation of internal stresses and surface hardening, ultrasonic wire drawing with reciprocating oscillatory motion of the wire die, solution homogenizing and formation of suspensions and emulsions [2]. A separate important feature of ultrasonic vibrations is intensification of motion of the environment through which they propagate, which can be applied to improve the efficiency of currently available technologies, which is especially true for welding and related processes [3].

It is known that in the electric arc welding technologies application of ultrasonic vibrations to the parts proper, to the molten metal or to the consumable electrode leads to active stirring of the weld pool due to mechanical vibrations, improvement of heat conductivity of the particles in the arc at increase of thermal diffusion coefficient and increase of pressure generated by the electric arc [4–6]. The arc proper under the influence of vibrations is constricted with increase in its energy density, which enhances the heat input into the metal particles [7]. More over, due to high-frequency vibrations the ionized particles stay in the arc longer after passing the resonant frequency [8]. Use of ultrasound in the technology of semi-automatic consumable electrode welding demonstrates a more active transfer of the melt particles from the wire tip: drop flight velocity rises by 10–20 % in case of 3 times increase of the frequency of drop detachment due to the melt film resonating at the wire tip, and to its surface fluctuations, and further imparting additional acceleration to the drops forming on the melt surface, which leads to reduction of the force required for drop detachment and to intensification of the processes of mass transfer in the electric arc, respectively [7–14].

Considering the above-mentioned influence of ultrasonic vibrations, use of these effects can be prom-

ising in such an application, as powder atomization in additive manufacturing (AM) technologies, which require spherical particles of narrow classes. At present the problem of producing powders of -63 μm class with a high sphericity coefficient has not been solved completely by technological implementation. The most promising technologies for producing fine spherical particles with a high sphericity coefficient and purity and chemical composition reproducibility are the plasma atomization (PA) processes [15, 16]. Proceeding from the fact that PA technologies traditionally use wires as feedstock materials for atomization, superposition of ultrasonic vibrations on them, owing to the influence on the electric arc and the melt, can be potentially applied to increase the yield of finely dispersed fraction of –100 μm class, improve the atomization process efficiency and increase the sphericity coefficient of the produced powders.

Accordingly, the objective of this work is establishing the influence of ultrasonic vibrations when producing the powders by gas and plasma-arc atomization of metal melts and compact materials on the dispersity and particle size distribution of the produced powders.

In connection with the fact that this aspect of application of high-frequency acoustic vibrations in melt atomization technologies requires further detailed investigation, this study addresses the following tasks: conducting a critical review of the currently available technologies of dispersion of metal melt microvolumes using ultrasound; assessment of the prospects for and conducting analysis of the effectiveness of ultrasound application in plasma-arc atomization of wire and rod materials and prospects for application of such an approach.

APPLICATION OF ULTRASONIC VIBRATIONS IN THE PROCESSES OF DISPERSION OF METAL MELT MICROVOLUMES

Ultrasonic generators are widely used for dispersion (atomization) of liquids and producing aerosols for medical applications and in analytical equipment to conduct investigations of chemical composition of liquids or dissolved solids by the method of emission spectroscopy. Unlike other dispersion methods, ultrasonic atomization is not related to formation of high-speed flows due to drop breakup by gas jets, and it requires more than 100 times lower power to produce drops of the required diameter. The main atomization mechanisms here are cavitation and resonance. The main variable, which determines the produced drop size, is the frequency of vibrations, which, in its turn determines the vibration amplitude [17–20].

The authors of work [21], which studied the influence of the oscillatory circuit elements on the average size of atomized particles, confirmed this hypothesis in practice and derived an empirical formula (1), from which is follows that the parameters, influencing the mean size of atomized particles are the liquid surface tension σ, density ρ and vibration frequency *f*, which is the main variable of the process:

$$D_{\text{av}} = 0.73\left(\frac{\sigma}{\rho f^2}\right)^{1/3}. \quad (1)$$

The authors of [19] established that in order to initiate the process of melt dispersion due to excitation of standing waves at the resonant frequency, it is necessary to reach a certain value of vibration amplitude. It follows from the proposed model that the minimal vibration amplitude depends on dynamic viscosity μ, density ρ, liquid surface tension σ and vibration frequency *f*:

$$A_m = \frac{2\mu}{\rho}\sqrt[3]{\frac{\rho}{\pi\sigma f}}. \quad (2)$$

A separate application of ultrasound spraying of liquids is spray drying. The method consists of spray drying, during which a liquid flow is injected into a reactor blown by hot air or heated gas, through an injector to which high-frequency vibrations are applied. This flow is a suspension or liquid dissolved using the respective solvent. When passing through the injector nozzle, the flow is broken up into small particles due to cavitation, their size being determined by the vibration frequency and liquid characteristics. After that, the solvent evaporates due to convection. The result of this is superfine particles with a narrow particle size distribution, which is an impossible task for conventional spray drying. However, the main applications of this method are food industry, pharmaceutical production and producing powder granulate for powder metallurgy. The latter allows solving the problem of producing composite nanopowders and significantly increasing the adaptability to fabrication of submicron powders, while also reducing the transportation losses through entrainment [20–25].

The above-mentioned regularities lead to the conclusion that atomization with application of ultrasonic vibrations, can be used not only for liquids, but also for metal melts. Accordingly, ultrasonic vibrations can be regarded as the method of improving the quality, and dipersity and increasing the yield of the most needed product in the technologies of producing dispersed powders by atomization.

GAS ATOMIZATION OF METAL MELTS WITH ULTRASOUND APPLICATION

Melt atomization by cold gas jets is a long-known and very common technology of producing metal powders. The atomization system consists of the crucible heating system, into which the feedstock material is charged, intermediate ladle with a special nozzle for pouring, gas supply system and process chamber. The first stage of gas atomization process is pouring the molten metal from an intermediate ladle through a special nozzle. Then, the liquid metal is broken up by inert gas jets, which promote melt separation into fine drops and their cooling, which occurs during drop falling into the hopper-collector [26].

The traditional gas atomization technology has significant imperfections: wide range of powder particle size distribution from 25 to 500 μm, low sphericity coefficient of up to 0.7, satellite formation on the surface of large particles and closed porosity [27]. In order to solve these problems, work was performed to optimize the gas atomization process, using ultrasonic vibrations, applied to the melt pouring tube, which is inserted into the nozzle, and which is the sonotrode for ultrasonic vibration transmission [28–30]. Figure 1 gives the schematic of such a process.

Local researchers [31] used the approach with ultrasonic vibration transmission to the melt through atomization gas with application of an intermediate nozzle, operating on the principle of an acoustic radiator. Vibrations in the intermediate nozzle arise due to gas flow cutting by the upper edge, which promotes vibration excitation in the gas before collision with the melt flow. Using a standard injection assembly for gas atomization with an ultrasonic intermediate nozzle and without it the authors determined that at atomization of NM79 alloy the yield of <80 μm fraction was not less than 75 % against 58 % without ultrasound application.

However, the technology of gas atomization with ultrasonic vibrations has not been implemented in industry, due to impossibility to eliminate the main drawbacks of the process, such as formation of close gas porosity and developed surface of the particles.

ULTRASONIC ATOMIZATION OF THE METAL MELT ON THE SONOTRODE

One of the newest methods for production of high-quality metal powders is melt atomization in a crucible, which is part of an ultrasonic oscillatory circuit.

So, the authors of work [32] developed a technological approach, which allows producing spherical powders of metals and alloys, using the feedstock in the form of a lumpy material, placed into the crucible of the induction furnace, from which the melt drops,

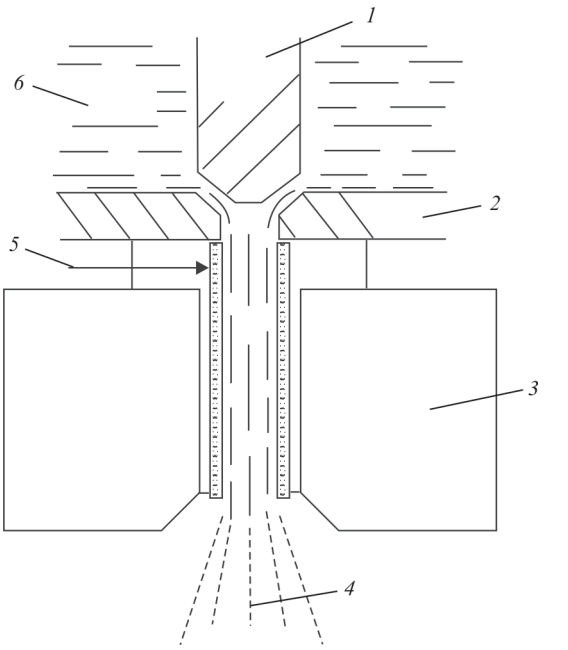

Figure 1. Ultrasonic gas atomization [28]: *1* — locking rod; *2–3* — ultrasonic injector; *4* — atomization cone; *5* — ceramic pouring tube; *6* — melt

flowing out through the nozzle, freely fall onto the sonotrode, to which vibrations of 20 kHz frequency are applied, and the electric arc is used to maintain the liquid state of the material (Figure 2). The atomization process chamber proper is filled with argon, and the drops, broken up by the capillary waves, which separate from the melt, are blown off by the argon flow and solidify. Removal of atmospheric gases before chamber filling with argon is performed using the vacuum pumps.

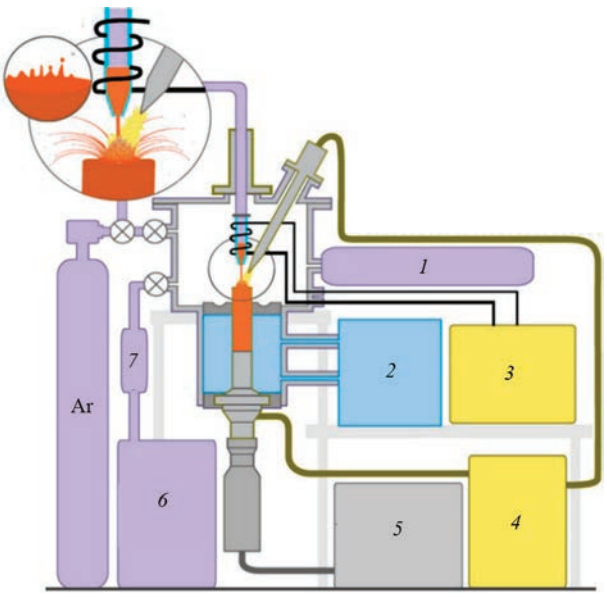

Figure 2. Schematic of ultrasonic atomization of the melt on the sonotrode with additional heating by an electric arc [32]: *1* — pressure sensor; *2* — water cooling; *3* — high-frequency generator; *4* — arc remelting system; *5* — ultrasonic generator; *6* — vacuum pump; *7* — filter

In work [33] researchers showed that atomization of metal melt of iron alloys on the sonotrode allows producing particles of less than 100 μm size, the yield of 32–45 and 45–63 μm fractions being not less than 60 % of the total powder yield. In work [34] it is shown that for titanium alloys Ti–6Al–4V and Ti25Al12Nb this technology allows ensuring particle sphericity coefficient of 0.9 and increasing the yield of the composition of –63 + 20 μm class, compared to gas atomization: gas atomization provides the yield of –63 μm fraction at the level of 30 % of the total volume, while ultrasonic atomization on the sonotrode has the yield of the order of 80–90 %, depending on vibration frequency.

During the experiments, researchers [24] found that for metal melt atomization on a surface vibrating at a high frequency, equation (3) is valid, which establishes the dependence of particle mean size on capillary wave length λ and empirical function *f*, which depends on the values of Weber (We), Onezorge (Oh) and intensity (In) criteria. In the majority of melt atomization processes the value of the function is taken equal to a unity (*f*(We, Oh, In) = 1.0):

$$D_{av} = 0.34\lambda f(\text{We, Oh, } In). \quad (3)$$

For calculation of the capillary wave length the authors of [34] propose applying empirical dependence (4), which includes surface tension σ and density ρ of the melt at a given temperature, vibration frequency *f*, as well as melt film thickness *h*:

$$\lambda = \sqrt[3]{\frac{8\pi\sigma \tan h\left(\frac{2\pi h}{\lambda}\right)}{\rho f^2}}. \quad (4)$$

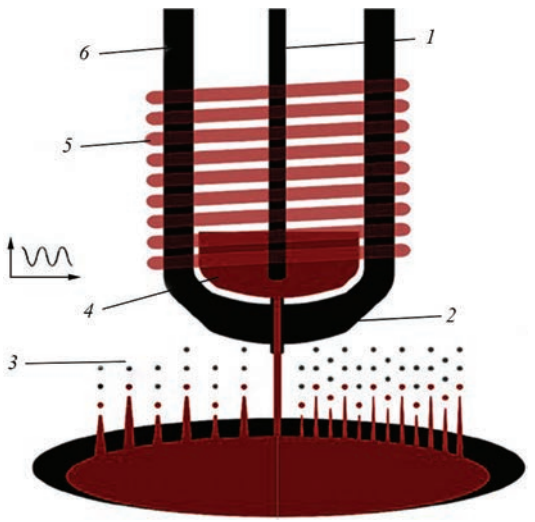

Figure 3. Schematic of ultrasonic atomization of the melt on the sonotrode [35]: *1* — locking graphite rod; *2* — graphite nozzle; *3* — aluminium powder; *4* — aluminium melt; *5* — inductor; *6* — graphite crucible

After substitution of the capillary wave length into formula (3) and assuming the value *f*(We, Oh, In) = 1, we obtain formula (5), which can be used to determine the mean value of the particle size using the value of density and surface tension of the melt at known temperature *T*.

$$D_m = 0.34\sqrt[3]{\frac{8\pi\sigma_T}{\rho_T f^2}}. \quad (5)$$

Conducting studies of the process of atomization of commercial aluminium powders in work [35] the researchers used simplified equipment without application of additional heating of the melt being poured. The process schematic is given in Figure 3, and the atomization technique is as follows: graphite crucible was filled with granulated aluminium powder and placed into the electromagnetic field of the inductor, the crucible was fitted with a graphite nozzle for pouring, the aluminium melt was poured onto the sonotrode from a copper alloy, vibrating at the frequency of 60 Hz. The process chamber was pumped down by a vacuum pump and was filled with argon to the pressure of 100 mbar, while the furnace was pumped down and filled with argon to the pressure of 200 mbar, i.e. pouring occurred at a certain differential pressure in addition to the gravity component. In this study the influence of vibration amplitude on the material particle size distribution was established, and it was shown that lowering of vibration amplitude narrows the particle size distribution and reduces the particle mean size. At 9.9 μm amplitude the mean size of aluminium particles was equal to 41.7 μm, and at 8.55 μm amplitude it was 31.8 μm, respectively.

PLASMA ARC ATOMIZATION DUE TO THE STANDING WAVE

Investigations of the possibility of metal melt atomization using the energy of high-frequency acoustic vibrations, began in the middle of the previous century. However, in 1987 researchers K.Bauckhage, P. Schockenberg and H.Vetters in their Patent 39 178A made an assumption as to the possibility of process intensification through application of two oscillatory circuits, where the sonotrodes are located opposite to each other, and to which ultrasonic vibrations are applied with a slight difference in the frequency. Under such a condition, a standing acoustic wave, close to a spherical shape, is generated between the sonotrodes, and the molten metal is fed from the crucible into the gap between the sonotrodes through the nozzle, its drops being torn apart from within due to cavitation, and the fragmented droplets flying out radially with subsequent cooling.

In further papers the researchers from [36] and [37] demonstrated the potential of the possible technology of atomization due to a standing wave (Ultrasonic Standing Wave Atomization) and defined the theoretical concepts of the processes of acoustic vibration transmission through the gas medium, heat transfer and the assumptions on particle formation from metal melts, giving the conclusion about the possibility of producing powders with mean size less than 15 μm.

However, there is no real data as to implementation of this approach in metal melt atomization, just a tentative schematic of closed-cycle process equipment is available, which is shown in Figure 4.

Despite the lack of technology implementation, potential application of a standing ultrasonic wave in plasma atomization of rod and wire materials is of interest. We assume that acoustic vibrations will propagate through the gas medium to the plasma, and from it — to the feedstock being atomized, which will generate additional pressure of melt drop detachment.

On the other hand we assume that according to investigations of [38], use of sonotrodes directed towards each other, will influence the plasma arc profile, constricting it, and increasing the energy density and heat transfer, optimizing, or intensifying the billet surface melting mode, respectively. This will potentially allow producing finer powders of a narrower fraction with higher productivity.

ELECTRIC ARC ATOMIZATION WITH APPLICATION OF VIBRATIONS TO THE ATOMIZED MATERIAL

Electric arc atomization is a long-known approach, traditionally used for spraying functional coatings by electric arc metallization technology. It is characterized by relative simplicity and affordability of the equipment, which consists of a block of electrode wire feed, atomization gas supply system, electric arc power system and atomization chamber. This technology also features high productivity, which can reach 40 kg/h in some cases. This technology provides a significant yield of the fine fraction (<63 μm) and other advantages. However, despite the numerous advantages, a significant disadvantage of electric arc spraying is the use of cold gas for melt atomization, which forms at the tip of atomized wires. This leads to production of powers with a high content of particles of an irregular shape, satellites and considerable internal porosity because of atomization gas entrapment by the melt, making their application in additive technologies more complicated [39, 40]. The process schematic is given in Figure 5.

Researchers of the work [40] during atomization of wires from stainless steel AISI 630 and melt drop dispersion by argon in the reactor in an argon atmosphere produced powders with particle size distribution from 10 to 160 μm at mean particle size of about 70 μm.

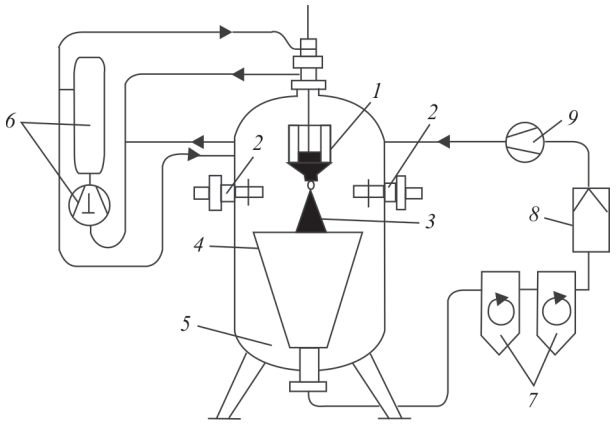

Figure 4. Schematic of the unit of ultrasonic atomization by a standing wave [36]: *1* — crucible with the melt; *2* — sonotrodes; *3* — atomization cone; *4* — device for waste gas removal; *5* — hopper-collector; *6* — tank with working gas; *7* — cyclones and sieves; *8* — filter; *9* — compressor

In work [41] the authors conducted experiments on aluminium wire atomization by an electric arc during melt dispersion by argon in an air atmosphere and obtained particles with sphericity coefficient in the range of 0.71 to 0.81 at mean particle size of 50–80 μm.

Coming back to the possibility of introducing high-frequency vibrations into the wires fed during electric arc atomization, at present there is no data on implementation of this approach. There are, however, several studies of heat- and mass transfer in electric arc MIG/MAG processes with simultaneous supply of ultrasonic vibrations to the welding wire. These investigations showed an active influence of ultrasound, applied to the wire-cathode, on surface tension and acceleration, which is additional to free fall acceleration due to gravity. The established regularities in semi-automatic MIG welding demonstrate that ultrasonic vibrations promote formation of elongated drop-shaped particles as opposed to spherical ones,

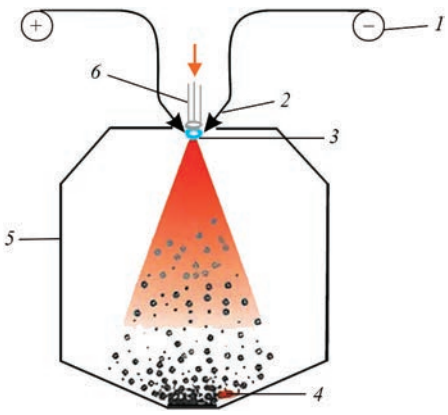

Figure 5. Block-diagram of electric arc atomization of the wire [40]: *1* — wire; *2* — wire feeder; *3* — electric arc; *4* — powder; 5 — atomization chamber; *6* — electric arc torch

forming during wire tip melting without vibrations. This, in its turn, allows narrowing the detachment zone, reducing the required detachment force, and accelerating the detachment proper by 20 %, which was established and modelled in works [11, 12].

On the other hand, ultrasonic vibrations have an essential influence on the electric arc proper: the electric arc becomes narrower, and its energy density increases, respectively. At the same time, heat input into the smallest constituent particles of the metal flow at melting by the arc is much higher, as the ionized particles stay in the arc longer after passing the resonance frequency due to the high-frequency vibrations [7, 8]. The authors of works [9, 10] determined that ultrasound application in the technology of semi-automatic welding by a consumable electrode in the form of wire demonstrates a more active transfer of the melt particles from the wire tip: drop flight velocity rises by 10–20 % with three times increase of the drop detachment. This effect is reached by melt film resonance at the wire tip and its surface fluctuations, leading to intensification of the processes of mass transfer into the weld pool [10].

Accordingly, we can make an assumption about the possible activation of the process of electric arc atomization and reduction of power consumption for it due to narrowing of the arc with increase of its specific energy. On the other hand, such a process will require use of two individual oscillatory circuits to transmit the ultrasound to the wire-anode and wire-cathode. The influence on the atomization process can be also interesting, namely — on formation of the melt drop and its disintegration, cavitation and, possibly, of the standing wave, which will form between the wire tips and will propagate through the gas medium, intensifying the atomization and narrowing the particle size range.

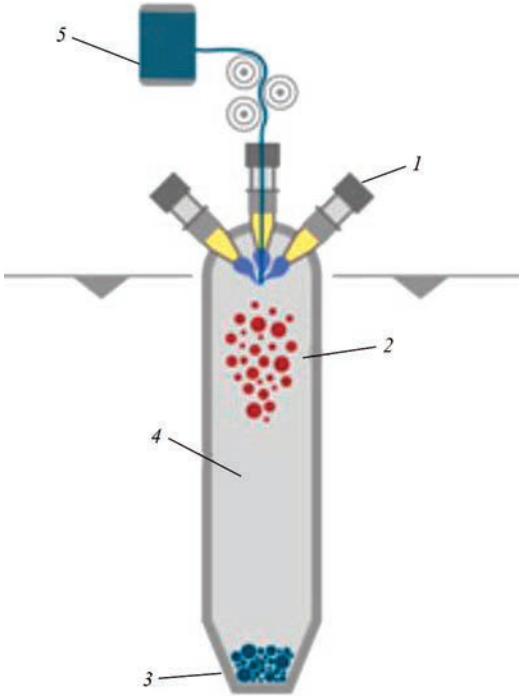

Figure 6. Plasma atomization of wire by PyroGenesiss technology [44]: *1* — plasmatron; *2* — melt drops; *3* — wire; *4* — argon; *5* — wire spool

PLASMA ARC ATOMIZATION WITH ULTRASONIC VIBRATIONS, APPLIED TO THE ATOMIZED MATERIAL

One of the most promising technologies for production of high-quality spherical powders is plasma spraying, which is not without its difficulties: a large number of variable working parameters complicate achieving a repeatable result and productivity. In work [42], investigations were performed and it was established that at least eight working parameters have their influence on the final size of the powder particles during atomization of the current-conducting wire, the influence of arc current, wire feed rate, arc length, accompanying gas flow rate and gap between the plasmaforming and compression nozzles being the strongest.

One of the commercially implemented approaches to plasma atomization was carried out by "PyroGenesis" Company. Three plasmatrons are used during atomization, between which the wire is fed without supplying the electric potential, i.e. material melting occurs due to the plasma arc heat, and atomization — owing to plasma pressure [43]. The schematic of such a process is shown in Figure 6.

Notwithstanding the adaptability-to-fabrication, the productivity of the process of plasma atomization of powders is equal to 2–3 kg/h for titanium alloy powders, and it can be increased to 5 kg/h, when using additional induction heating of the wire material before feeding it into the plasmatron working zone [43].

There exist different approaches to increasing the productivity of plasma atomization process, such as material atomization by a transferred plasma arc, use of accompanying gas jets with supersonic plasma, as well as hybrid technologies [45]. Development and investigation of these technologies are performed by researcher teams all over the world. However, one of the hypothetically feasible, but not realized and not implemented ways of optimization and intensification of plasma arc spraying is application of ultrasonic vibrations to wires or rods fed into the process.

ANALYSIS OF THE EFFECTIVENESS AND PROSPECTS FOR ULTRASOUND APPLICATION IN PLASMA-ARC ATOMIZATION OF WIRE AND ROD MATERIALS

Plasma-arc atomization is one of the effective methods of producing spherical metal powders,

which are widely used in aviation, rocket and additive manufacturing industries. Improvement of this process by introducing ultrasonic vibrations can considerably improve the powder characteristics, in particular, their particle size distribution and sphericity. Plasma-arc atomization is based on the use of high-temperature plasma heat for surface melting of the tip of metal wires or rods, melt drop detachment and their dispersion by the plasma jet. The main parameters of the process are plasma temperature, flow velocity, electric parameters of the arc and atomized material properties. The influence of all these parameters determines the final characteristics of the produced powder.

Moreover, promising is introduction of another kind of influence, namely ultrasonic vibrations, which during propagation through the atomized material lower the surface tension of the melt film, cause intensification of the heat- and mass transfer, generate additional pressure on the melt drop accelerating its detachment, promote refinement of the initial drop and improvement of atomization homogeneity. According to investigations, conducted in work [34], where comparison of ultrasonic atomization on the sonotrode is compared to the traditional gas atomization, addition of high-frequency vibrations into the metal melt promotes an increase of the yield of fine particles with a narrow particle size distribution of –63 + 20 μm to 80–90% due to reduction of the initial size of the melt drop. Here, according to equations (1) and (5), the frequency of vibrations applied to the melt, has a considerable influence on the critical (initial) size of the drop. The particle size becomes smaller with frequency increase.

During investigations the authors of [4] determined that the use of ultrasonic vibrations superposed onto the welding wire, promotes an increase of particle heat conductivity in the plasma arc with increase of the thermal diffusion coefficient and increase of pressure generated by the arc. The latter was mathematically modelled and experimentally confirmed by the authors of works [5, 6]. The proposed mathematical model (6) allows for the influence of the following variables on the arc pressure: arc parameters, nozzle geometrical parameters, process gas density and plasma flow velocity, as well as the sound pressure magnitude. Proceeding from the established regularities, the amplitude of wire tip vibration makes a significant contribution to arc pressure, increasing it by 15–31 %:

$$P(x,y,z)=\frac{\eta_i 3r_{\text{n}}^2\rho_{\text{Ar}}Q_{\text{pl}}}{A_{\text{I}}S_{\text{n}}}\times$$
$$\times\sqrt{\frac{P_{\text{osc}}^2}{\rho_{\text{Ar}}^2c^2}+\frac{2\eta_{\upsilon}IU}{\rho_{\text{Ar}}Q_{\text{pl}}}+\frac{Q_{\text{pl}}^2}{S_{\text{n}}^2}}\frac{\mu_0 I^2}{4\pi^2 r_p^2}\times \qquad (6)$$
$$\times\exp\left(-3\frac{x^2+y^2}{r_p^2}\right).$$

Author teams in works [13, 14] conducted investigations, which agree with theory and are confirmed by high-speed filming. It was established that wire vibrations with the frequency from 1 kHz and higher promote an earlier drop detachment, and the most efficient mode of new drop detachment at each vibration is achieved at the frequency of 20 kHz.

Mathematical modelling which was conducted in work [10], proposes a description of the magnitude of ultrasound force F_U, acting on the melt drop (7), as such which depends on the gas medium density ρ, in which the vibrations propagate, vibration amplitude A, wave number k, particle radius R and coefficient λ, allowing for the relationship between the medium density and melt drop:

$$F_U=\frac{1}{3}\pi\rho A^2(kR)^3\sin(2k)\frac{5-2\lambda}{2+\lambda}. \qquad (7)$$

According to our assumptions and the above investigation results, the experience of introducing ultrasonic vibrations into the melt can be transferred to the process of plasma atomization of compact materials. Superposition of ultrasonic vibrations in plasma-arc atomization offers the prospect of intensification of the dispersion process and increasing the yield of –63 μm fraction to 80–90 %. The most promising appears to be the process of plasma arc atomization of rods and wires with application of ultrasonic vibrations to them, which propagate through the material of the wires and rods as if along a sonotrode, up to the tip with the velocity greatly exceeding that of propagation in the gas medium.

CONCLUSIONS

1. An approach has been substantiated to improvement of melt atomization process by introducing ultrasonic vibrations, which during propagation through the atomized material or gas medium, allows lowering the surface tension of the melt film, intensifying mass transfer, achieving drop refinement and improving the atomization uniformity. The main mechanism of such an influence is generation of capillary forces and cavitation in the melt drops during propagation of

high-frequency vibrations in them, which, in its turn, will put additional pressure on the melt drop and will reduce the force required for the drop detachment. All this significantly improves the technological characteristics of the produced powders, in particular, promotes reduction of particle sizes and increase of the sphericity parameter.

2. Conducted analysis of the effectiveness of ultrasound application in plasma-arc atomization of the wire and rod materials confirmed the good prospects of introducing ultrasonic vibrations not into the gas medium or plasma arc, which is inefficient because of the low velocity of acoustic vibration propagation in gases, but exactly into the atomized feedstock in the form of wires or rods, which promotes more frequent detachment of the melt drops from the atomized tip, with reduced size of the initial drops. In keeping with our assumptions, superposition of ultrasonic vibrations on the wires and rods during plasma arc atomization will increase the yield of fine-dispersed spherical particles of –63 μm class from 40–50 to 80–90 %.

REFERENCES

1. Shoh, A. (1975) Industrial applications of ultrasound — A review I. High-power ultrasound. *IEEE Transact. on Sonics and Ultrasonics*, 22(**2**), 60–70. DOI: https://doi.org/10.1109/tsu.1975.30780
2. Škamat, J., Valiulis, A.V. (2010) About the possibility of using ultrasound in thermal spray technologies. *Mokslas-Lietuvos Ateitis*, 2(**4**), 39–41. DOI: https://doi.org/10.3846/mla.2010.066
3. Kumar, S., Wu, C.S., Padhy, G.K., Ding, W. (2017) Application of ultrasonic vibrations in welding and metal processing: A status review. *J. of Manufacturing Proc.*, **26**, 295–322. DOI: https://doi.org/10.1016/j.jmapro.2017.02.027
4. Li, Y., Wu, C., Chen, M. (2020) Effects of ultrasonic vibration on the transport coefficients in plasma arc welding. *Metals*, 10(**3**), 312. DOI: https://doi.org/110.3390/met10030312
5. Wu, C.S., Zhao, C.Y., Zhang, C., Li, Y.F. (2017) Ultrasonic vibration assisted keyholing plasma arc welding. *Welding J.*, **96**, 279–287
6. Qiao, J., Wu, C-S., Li, Y. (2020) Numerical and experimental investigation of keyholing process in ultrasonic vibration assisted plasma arc welding. *J. of Manufacturing Proc.*, **50**, 603–613. DOI: https://doi.org/10.1016/j.jmapro.2020.01.019
7. Fan, C.L., Yang, C.L., Lin, S.B., Fan, Y.Y. (2013) Arc characteristics of ultrasonic wave-assisted GMAW. *Welding J.*, 92(**12**), 375–380.
8. Fan, C., Zhou, L., Liu, Z. et al. (2018) Arc character and droplet transfer of pulsed ultrasonic wave-assisted GMAW. *Inter. J. Ad. Manuf. Technol.*, **95**, 2219–2226. DOI: https://doi.org/10.1007/s00170-017-1414-7
9. Weifeng, X., Fan, C.L., Yang, C.L. (2016) Pulsed ultrasonic wave assisted GMAW of 7 A 52 aluminium alloy. *Welding J.*, **95**, 239–247.
10. Luo, J., He, Z., Liu, Z. et al. (2024) The influence of coaxial ultrasound on the droplet transfer of high nitrogen steel GMAW process. *Materials*, (**17**), 5509, 14. DOI: https://doi.org/10.3390/ma17225509
11. Fan, Y.Y., Yang, C.L., Sanbao, L. et al. (2012) Ultrasonic wave assisted GMAW: A novel method adds ultrasonic wave to provide an additional force to detach the droplet. *Welding J.*, **91**, 91–99.
12. Zheng, H, Qi, B., Yang, M. (2021) Dynamic analysis of the ultrasonic-frequency pulsed GMAW metal transfer process. *J. of Manufacturing Proc.*, **62**, 283–290. DOI: https://doi.org/10.1016/j.jmapro.2020.12.049
13. Kaiyuan, W., Jing, L., Haoran, Y. et al. (2024) Influence of high-frequency pulse on droplet transfer process and weld formation in double-wire median pulsed GMAW of aluminium alloy. *Research Square*. DOI: https://doi.org/10.21203/rs.3.rs-4308754/v1. https://www.researchsquare.com/article/rs-4308754/v1
14. Ghosh Prakriti, K., Lutz Dorn M.C. Hübner, Vinay K. Goyal (2007) Arc characteristics and behaviour of metal transfer in pulsed current GMA welding of aluminium alloy. *J. of Materials Proc. Technology*, **194**, 163–175.
15. Shanthar, R., Chen, K., Abeykoon, C. (2023) Powder-based additive manufacturing: A critical review of materials, methods, opportunities, and challenges. *Adv. Eng. Mater.*, (**25**), 2300375, 43. DOI: https://doi.org/10.1002/adem.202300375
16. Fatemeh, A.T., Zobaideh, H., Kahrizsangi, S. et al. (2024) Spreadability of powders for additive manufacturing: A critical review of metrics and characterisation methods. *Particuology*, **93**, 211–234. DOI: https://doi.org/10.1016/j.partic.2024.06.013
17. Barreras, F., Amaveda, H., Lozano, A. (2002) Transient high-frequency ultrasonic water atomization. *Experiments in Fluids*, **33**, 405–413. DOI: https://doi.org/10.1007/s00348-002-0456-1
18. Lozano, A., García, J., Alconchel, J. et. al. (2017) Influence of liquid properties on ultrasonic atomization. In: *Proc. of 28th European Conf. on Liquid Atomization and Spray Systems (ILASS2017)*. DOI: https://doi.org/10.4995/ILASS2017.2017.4588
19. Rajan, R., Pandit, A.B. (2001) Correlations to predict droplet size in ultrasonic atomization. *Ultrasonics*, 39(**4**), 235–255. DOI: https://doi.org/10.1016/s0041-624x(01)00054-3
20. Camacho-Lie, M., Antonio-Gutiérrez, O., López-Díaz, A.S. et al. (2023) Factors influencing droplet size in pneumatic and ultrasonic atomization and its application in food processing. *Discover Food*, 3(**23**). DOI: https://doi.org/10.1007/s44187-023-00065-5
21. Dobre, M., Bolle, L. (2002) Practical design of ultrasonic spray devices: Experimental testing of several atomizer geometries. *Experimental Thermal and Fluid Sci.*, **26**, 205–211. DOI: https://doi.org/10.1016/S0894-1777(02)00128-0
22. Patil, M.N., Pandit, A.B., Thorat, B.N. (2007) Ultrasonic atomization assisted spray drying. In: *Proc. of the 5th Asia-Pacific Drying Conf.*, 255–261. DOI: https://doi.org/10.1142/9789812771957_0036
23. Khaire, R., Gogate, P. (2020) Novel approaches based on ultrasound for spray drying of food and bioactive compounds. *Drying Technology*, 39(**12**), 1832–1853. DOI: https://doi.org/10.1080/07373937.2020.180492639
24. Marie, A., Tourbin, M., Robisson, A.C. et al. (2021) Wet size measurements for the evaluation of the deagglomeration behaviour of spray-dried alumina powders in suspension. *Ceramics Inter.*, 48(**6**), 7926–7936. DOI: https://doi.org/10.1016/j.ceramint.2021.11.340
25. Nandiyanto, A., Okuyama, K. (2011) Progress in developing spray-drying methods for the production of controlled morphology particles: From the nanometer to submicrometer size ranges. *Advanced Powder Technology*, 22 (**1**), 1–19. DOI: https://doi.org/10.1016/j.apt.2010.09.011
26. Zhou, K., Han, C. (2023) Metal powder-based additive manufacturing. **319**. DOI: https://doi.org/10.1002/9783527822249

27. Chen, G., Zhao, S., Tan, P. et al. (2018) A comparative study of Ti–6Al–4V powders for additive manufacturing by gas atomization, plasma rotating electrode process and plasma atomization. *Powder Technology*, **333**, 38–46. DOI: https://doi.org/10.1016/j.powtec.2018.04.013
28. Rai, G., Lavernia, E., Grant, N. J. (1985) Powder size and distribution in ultrasonic gas atomization. *JOM*, 37(**8**), 22–26. DOI: https://doi.org/10.1007/bf03257674
29. Baram, J. (1988) Pressure characteristics at the pour-tube orifice in ultrasonic gas atomization. *Materials Sci. and Eng*., **98**, 65–69. DOI: https://doi.org/10.1016/0025-5416(88)90128-0
30. Anand, V., Kaufman, A.J., Grant, N. (1978) Rapid solidification of a modified 7075 aluminium alloy by ultrasonic gas atomization. *Rapid Solidification Processing, Principles and Technologies, II*, Claitor, Baton Rouge, LA, 273–286.
31. Orlov, Y., Mamedov, B. (1983) Ultrasonic atomization of liquid metals. *Powder Metallurgy and Metal Ceramics*, 22(**4**), 254–255. DOI: https://doi.org/10.1007/bf00795594
32. Żrodowski, Ł., Wróblewski, R., Choma, T. et al. (2021) Novel cold crucible ultrasonic atomization powder production method for 3D printing. *Materials*,14(**10**), 2541, 11. DOI: https://doi.org/10.3390/ma14102541
33. Halapi, D., Varga, L. (2023) Ultrasonic powder atomization for additive manufacturing. *Inter. J. of Eng. and Management Sci*., 8(**2**), 69–75. DOI: https://doi.org/10.21791/IJEMS.2023.2.8
34. Bałasz, B., Bielecki, M., Gulbiński, W., Słoboda, Ł. (2023) Comparison of ultrasonic and other atomization methods in metal powder production. *J. of Achievements in Materials and Manufacturing Eng*., 116(**1**), 11–24. DOI: https://doi.org/10.5604/01.3001.0016.3393
35. Priyadarshi, A., Shahrani, S., Choma T. et. al. (2024). New insights into the mechanism of ultrasonic atomization for the production of metal powders in additive manufacturing. *Add. Manuf.*, 83(**1**), 104033, 20. DOI: https://doi.org/10.1016/j.addma.2024.104033
36. Bauckhage, K., Andersen, O., Hansmann, S. et al. (1996) Production of fine powders by ultrasonic standing wave atomization. *Powder Technology*, 86(**1**), 77–86. DOI: https://doi.org/10.1016/0032-5910(95)03040-9
37. Andersen, O., Hansmann, S., Bauckhage, K. (1996) Production of fine particles from melts of metals or highly viscous fluids by ultrasonic standing wave atomization. *Particle & Particle Systems Characterization*, 13(**3**), 217–223. DOI: https://doi.org/10.1002/ppsc.19960130308
38. Irisarri, J., Ezcurdia, I., Iriarte, N. et al. (2025) Electric plasma guided with ultrasonic fields. *Sci. Advances*, 11(**6**): eadp0686. 6. DOI: https://doi.org/10.1126/sciadv.adp0686
39. Korzhyk, V.M., Strogonov, D.V., Burlachenko, O.M. et al. (2024) Development of hybrid technology of producing spherical powders from wire materials using high-speed plasma jets and electric arc. *Suchasna Elektrometalurhiya*, **3**, 36–44. DOI: https://doi.org/10.37434/sem2024.03.05
40. Chen, D., Daoud, H., Scherm, F. et al. (2020) Stainless steel powder produced by a novel arc spray process. *J. of Materials Research and Technology*, **9**, 8314–8322. DOI: https://doi.org/10.1016/j.jmrt.2020.05.076
41. Dietrich, S., Zaeh, M.F. (2019) Arc-based powder production of AlSi7Mg0.6. *Procedia Manufacturing*, **40**, 27–31. DOI: https://doi.org/10.1016/j.promfg.2020.02.006
42. Strogonov, D.V., Korzhyk, V.M., Jianglong, Yi et al. (2022) Influence of the parameters of the process of plasma-arc spheroidization of current-conducting wire from low-carbon steel on the granulometric composition of the produced powders. *Suchasna Elektrometalurhiya*, **3**, 29–37. DOI: https://doi.org/10.37434/sem2022.03.05
43. Dion, C., Carabin, P., Kreklewetz, W. (2021) *Plasma apparatus for the production of high quality spherical powders at high capacity*. European Pat. EP3302855B1.
44. https://pyrogenesisadditive.com/#plasmaAtomization
45. Korzhyk, V.M., Strohonov, D.V., Burlachenko, O.M. et al. (2023) Development of plasma-arc technologies of spherical granule production for additive manufacturing and granule metallurgy. *The Paton Welding J*., **12**, 3–18. DOI: https://doi.org/10.37434/tpwj2023.12.01

ORCID

V.M. Korzhyk: 0000-0001-9106-8593,
O.S. Tereshchenko: 0009-0003-4021-0758,
D.V. Strohonov: 0000-0003-4194-764X,
O.I. Demianov: 0000-0001-7184-3839,
O.V. Ganushchak:0000-0003-4392-6682

CONFLICT OF INTEREST

The Authors declare no conflict of interest

CORRESPONDING AUTHOR

V.M. Korzhyk
E.O. Paton Electric Welding Institute of the NASU
11 Kazymyr Malevych Str., 03150, Kyiv, Ukraine.
E-mail: vnkorzhykn@gmail.com

SUGGESTED CITATION

V.M. Korzhyk, O.S. Tereshchenko, D.V. Strohonov, O.I. Demianov, O.V. Ganushchak (2025) Prospects of ultrasound application in the production of dispersed granules by gas and plasma-arc atomization of metal melts and compact materials (Review). *The Paton Welding J*., **10**, 3–11. DOI: https://doi.org/10.37434/tpwj2025.10.01

JOURNAL HOME PAGE

https://patonpublishinghouse.com/eng/journals/tpwj

Received: 23.04.2025
Received in revised form: 22.07.2025
Accepted: 25.10.2025

DOI: https://doi.org/10.37434/tpwj2025.10.02

MECHANICAL PROPERTIES OF METAL IN AREAS OF WELDED JOINTS OF MEDIUM-CARBON ALLOY STEELS HEATED TO TEMPERATURES FROM 350 TO 800 °C

V.D. Poznyakov, O.V. Korieniev

E.O. Paton Electric Welding Institute of the NASU
11 Kazymyr Malevych Str., 03150, Kyiv, Ukraine

ABSTRACT

During welding, two characteristic areas are formed in the heat-affected zone (HAZ) of welded joints of medium-carbon alloy steels with hardened (located in the HAZ areas of overheating, normalization and partial recrystallization — high-temperature area) and tempered metal (located mainly in the HAZ areas of recrystallization and blue brittleness — low-temperature area). In welded joints made using manual arc and mechanized gas-shielded welding with small-diameter wires, the width of these areas can reach 2.5 and 8 mm, respectively. The influence of thermal cycles, characteristic for the high-temperature area of the HAZ, on the mechanical properties of the metal is well covered in technical literature. There is much less information on the influence of thermal cycles of welding on the mechanical properties of the low-temperature area of the HAZ. This paper presents the data on the course of the heating and cooling process of the HAZ metal of butt welded joints 12 mm thick, which were heated to temperatures of 780, 550 and 350 °C, and on the effect of such heating on the mechanical properties (hardness, strength, ductility, impact toughness) of medium-carbon alloy steels with different content of alloying elements.

KEYWORDS: medium-carbon alloy steels, mechanical properties, thermal cycles, alloying elements

INTRODUCTION

Medium-carbon alloy heat-strengthened steels with high hardness (*HB* > 5000 MPa) and strength (σ_t > 1400 MPa) can be used both to manufacture military products, exposed to considerable shock impact, and to produce heavy-duty components and mechanisms of machines for civil purposes, such as quarry excavator buckets, bodies of heavy trucks, etc. The above-mentioned steels acquire the required set of mechanical properties, high hardness, strength and impact toughness due to alloying with manganese, silicon, chromium, molybdenum, and nickel; microalloying with boron, titanium, aluminium, vanadium, etc., as well as a result of heat treatment, which consists in quenching and low-temperature (at not higher than 250 °C temperature) tempering of steel [1–6].

The majority of the products, manufactured with application of heat-strengthened medium-carbon alloy steel of a high hardness are welded. Arc processes are usually used for welding such products. They envisage local heating of the steel rolled stock up to temperatures, exceeding that of the steel tempering, and in the near-weld zone the temperature is close to its melting temperature. The HAZ of the welded joints can be conditionally divided into two areas: high- and low-temperature. The HAZ high-temperature area includes the area of overheating (temperature varies within 1100–1500 °C), area of normalization (temperature varies in the range of 930–1100 °C) and of partially incomplete recrystallization (temperature varies within 720–930 °C). In this area of the welded joint the metal transforms into austenite at heating, and at cooling, depending on the chemical composition and degree of metal overcooling, phase-structural transformations take place in it with formation of ferrite-bainite-martensite or mixed structures. The HAZ low-temperature area includes the areas of recrystallization (temperature varies within 450–720 °C) and of blue brittleness (temperature varies within 200–450 °C). The size and distance to the weld axis in the areas heated to the above-mentioned temperatures in the welded joint depend on many factors. The main of them are the welding mode, metal thickness and joint type. For the processes characteristic for manual, stick electrode and gas-shielded mechanized welding, the width of the HAZ high-temperature area can reach 2.5 mm and that of the low-temperature one is 8 mm.

At present, the questions of the influence of the welding modes and conditions of welded joint cooling on the structural transformations, occurring in the metal of the HAZ overheating area are quite well highlighted in technical publications [4–8]. The data on the influence of the above factors on the mechanical properties of the metal are presented in the scientific publications to a lesser extent, but also well [9–12]. As to the HAZ low-temperature areas, where the metal is heated to temperatures, higher than A_{c1} temperature, the amount of such information is limited, and it mainly concerns the metal hardness values.

THE OBJECTIVE

of this work consisted in having determined the coordinates of the HAZ tempering area, assessing the running of the thermal processes of welding in it

Table 1. Chemical composition of the studied medium-carbon alloy steels

Steel marking	Weight fraction of elements, %									
	C	Si	Mn	Cr	Ni	Mo	V	S	P	B
"1"	0.23	0.25	0.82	0.50	0.90	0.30	0.030	0.004	0.016	0.003
"2"	0.31	0.16	0.74	1.66	2.26	0.30	0.202	0.010	0.016	–
"3"	0.21	0.45	0.92	0.58	0.38	0.20	0.010	0.005	0.023	0.004

(heating–cooling of metal, depending on the welding modes), reproducing these processes on model samples and establishing how the above-mentioned changes influence the mechanical properties of the tempered metal.

MATERIALS AND METHODS OF INVESTIGATIONS

Investigations were performed using several medium-carbon alloy steels with the yield point above 1200 MPa, differing by their chemical composition (see Table 1).

Welding of butt welded joints 12 mm thick was performed by mechanized method in shielding gas atmosphere (82 % Ar + 18 % CO_2) with 1.2 mm wire of ChORDA 307 Ti brand (08Kh20N9G7T alloying system), using the following mode: welding current I_w = 160–180 A; arc voltage U_a = 23–25 V; welding speed V_w = 10–12 m/h.

Location of the tempering area was determined based on measurement of metal microhardness in the welded joint HAZ. Measurement step was equal to 1 mm.

Impact toughness of the metal in the tempering area was assessed by the results of impact bend tests of standard samples of 10×10×55 mm size with a round notch of Mesnager type, cut out of the welded joints. Sample tests were conducted at the temperature of 20 °C.

The thermal cycle of welding was recorded for three areas of the welded joint tempering zone, namely, areas heated up to temperatures of 780, 550 and 350 °C. Chromel-alumel thermocouple of 0.5 mm diameter was used for this purpose.

Values of strength ($\sigma_{0.2}$ and σ_t) and ductility (δ_5 and ψ) were determined by the results of tensile tests of standard samples, processed in keeping with the thermal cycles characteristic for the tempering zone of the HAZ metal of the joints, which were welded in the above-given modes. Heating of model samples of 12×12×120 mm size was conducted in MRS-75 unit by current flowing through the sample by the preset program [13]. The cooling rate of the samples was regulated by their blowing with air with different intensity.

TESTING RESULTS AND THEIR DISCUSSION

Measurements of microhardness of the metal of welds, HAZ and steel rolled stock (Figure 1) showed that the weld metal hardness is almost the same in all the cases, and it is in the range of *HB* 230–260. This is natural, as the same wire and welding modes were used for welding. As regards the metal microhardness in the areas of HAZ and steel, which are located at different distances from the weld, these indices depend on the steel chemical composition. The highest values of hardness (approximately, *HB* 530) are characteristic for the strengthened area of overheating of the HAZ (located at 1 mm distance from the fusion line of welded joints of steels "2" and "3"). Somewhat lower hardness values (*HB* 450) are found in the metal of the overheating area of the HAZ of welded joints on steel "1". Hardness of the tempering area (located in the range of 4–9 mm), as that of the base metal (located in the range of 10–13 mm) is also the lowest in the joints of steel "1". The highest *HB* values, almost at the level of base metal hardness, are characteristic for the tempering area of welded joints of steel "2".

Thus, by the results of these studies it was determined that depending on the chemical composition of steels, the high hardness of the metal which it acquires through heat treatment of the steel, can be reduced as a result of heating by the thermal cycle of welding. The smaller is the concentration of alloying elements in the steel, the lower the values of metal hardness in the HAZ tempering area.

The data on the conditions of heating and cooling of individual tempering areas of the HAZ metal are given in Figure 2. Three tempering areas are considered, which were heated to temperatures of 780, 550 and 350 °C as a result of the effect on the metal of the heat from welding arc burning. For this purpose, the thermocouples were mounted at the distance of 4, 6 and 9 mm from the fusion line. Analysis of the obtained results showed that the intensity of reduction

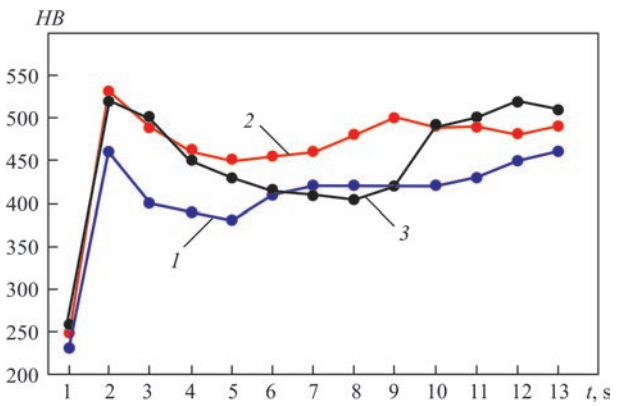

Figure 1. Microhardness values of the weld metal, HAZ and base metal of butt welded joints 12 mm thick of steels: "1" — Row 1; "2" — Row 2; "3" — Row 3

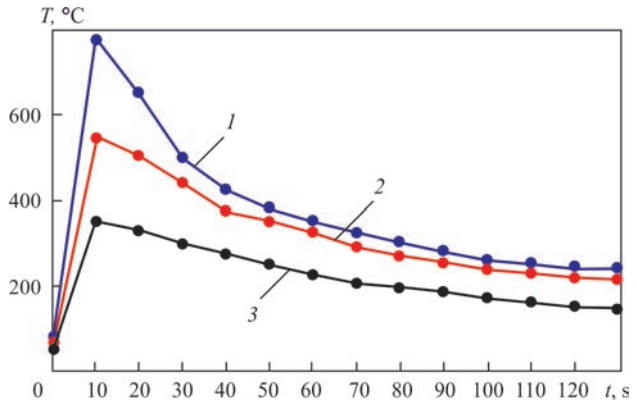

Figure 2. Thermal cycles of welding the tempering areas of the HAZ in butt welded joints 12 mm thick, which were heated to temperatures of: 780 °C — Row 1; 550 °C — Row 2; 350 °C — Row 3

of the metal temperature at the initial stage of its cooling is significantly different. The higher the heating temperature, the higher is the cooling rate. In the temperature range of 400–300 °C the intensity of metal cooling is equalized in all the HAZ tempered areas.

The data given in Figure 2 were furtheron used for modeling the thermal cycles of welding during treatment of the above-mentioned samples by these cycles.

Results of testing samples for tension (made from heat-treated model samples) and for impact bending (made from welded joints) are given in Table 2.

As indicated by the data given in Table 2, the values of strength ($\sigma_{0.2}$ and σ_t) of the HAZ metal heated up to temperatures from 350 to 780 °C, in all the cases decrease relative to the initial strength of steel. The extent of these changes depends on the steel chemical composition and on the temperature, to which the HAZ metal was heated during welding. The lower the concentration of the alloying elements and boron in steel, or the higher the heating temperature, the more significant is the reduction of the metal hardness. So, $\sigma_{0,2}$ and σ_t values of the HAZ metal which was heated up to the temperature of 780 °C during welding, decrease by almost 40 % for welded joints of steel "1" relative to the base metal, and for steels "2" and "3" — by 20–25 %, which is two times smaller. The smallest changes in the strength values are observed in the metal, heated to the temperature of 350 °C during welding: they decrease by 10 % in the welded joints of steel "1" and "3" and remain almost unchanged in joints of steel "2".

As regards the ductility properties (δ_5 and φ) of the metal, unlike the strength values, they grow by 30–50 % in welded joints of steels "1" and "3", irrespective of the temperature to which the metal was heated, and almost do not change in joints of steel "2".

As to the impact toughness values, these characteristics of the metal essentially depend both on the temperature to which the metal was heated during welding, and on temperatures, at which the samples were tested. The most essential changes of *KCU* values are observed in the metal tested at the temperature of 20 °C. In samples, where the notch was made in the areas where the metal was heated to temperatures of 550 and 780 °C, the impact toughness values increased 1.3–2.2 times. The highest values are characteristic for samples cut out of welded joints of steel "1" with a notch located in the zone, where the metal was heated to the temperature of 780 °C. As regards the results of testing samples, in which the notch was made in the metal heated to the temperature of 350 °C during welding, their impact toughness turned out to be lower relative to base metal. As was noted above, this temperature belongs to the temperature range, where metal blue brittleness occurs with reduction of its impact toughness values, characteristic for this phenomenon. It should be noted that *KCU* reduction is characteristic both for samples tested at the tem-

Table 2. Mechanical properties of medium-carbon alloy steels, which were studied and of the metal of HAZ areas heated to temperatures of 780, 550 i 350 °C

Steel marking	Heating temperature, °C	*HB*	$\sigma_{0,2}$	σ_t	δ_5	φ	*KCU*, J/cm²	
			MPa		%		+20 °C	–40 °C
"1"	0	450	1447	1690	11.0	47.2	93	85
	350	420	1294	1497	21.0	63.0	89	76
	550	380	937	1044	20.0	69.1	176	173
	780	400	892	981	23.2	68.5	208	183
"2"	0	490	1475	1835	14.1	46.1	61	59
	350	500	1409	1773	13.6	45.4	50	37
	550	450	1378	1620	13.9	46.4	85	57
	780	490	1210	1463	14.8	47.0	98	62
"3"	0	520	1542	1844	11.5	44.3	52	51
	350	500	1402	1594	14.6	61.3	36	32
	550	430	1389	1520	14.9	60.0	74	52
	780	420	1242	1383	15.0	57.2	83	55

perature of 20 °C, and for those which were tested at the temperature of –40 °C.

CONCLUSIONS

Results of investigations of the influence of the thermal cycles of welding on the mechanical properties of the metal in the low-temperature areas of the HAZ of welded joints of medium-carbon alloy steels of high hardness (*HB* 500) with different chemical composition showed the following:

1. High hardness of the metal which it acquires heat treatment of the steel during manufacturing of the rolled stock, can be reduced as a result of metal heating by the thermal cycles characteristic for HAZ low-temperature areas. The smaller is the concentration of the alloying and microalloying elements in steel, the lower the values of metal hardness in the HAZ tempering area.

2. The strength of the metal in the HAZ areas of welded joints of heat-strengthened medium-carbon alloy steels heated up to temperatures of 350–780 °C, decreases, while ductility increases relative to the base metal.

3. Impact toughness of the metal of HAZ areas of welded joints of heat-strengthened medium-carbon alloy steels, heated to temperatures of 550–780 °C, is increased relative to the base metal, and in the case of heating to the temperature of 350 °C, it decreases. The latter is related to the fact that the temperature of 350 °C is included into the range of blue brittleness temperatures of the studied steels.

REFERENCES

1. Tekin Özdemir (2020) Mechanical and microstructural analysis of armor steel welded joints. *Inter. J. of Eng. Research and Development UMAGD*, 12(**1**), 166–175. DOI: https://doi.org/10.29137/umagd.488104
2. Konat, Ł., Białobrzeska, B., Białek, P. (2017) Effect of welding process on microstructural and mechanical characteristics of Hardox 600 steel. *Metals,* 7(**9**), 349. DOI: http://dx.doi.org/10.3390/met7090349
3. Gaivoronskyi, O.A., Poznyakov, V.D., Zavdoveyev, A.V. et al. (2023) Prevention of cold cracking in armour steel welding. *The Paton Welding J*., **5**, 3–10. DOI: https://doi.org/10.37434/tpwj2023.05.01
4. Oskwarek, M. (2006) Structural features and susceptibility to cracking of welded joints of Hardox 400 and Hardox 500 steels. In: *Proc. of the IV Students' Science Conf. on Human-Civilisation-Future, Wroclaw, Poland, 22–24 May 2006*. Vol. 2, 115–120.
5. Cabrilo, A., Geric. K. (2016) Weldability of high hardness armor steel. *Advanced Materials Research*, **1138**, 79–84. DOI: https://doi.org/10.4028/www.scientific.net/AMR.1138.79
6. Kuzmikova, L. (2013) *An investigation of the weldability of high hardness armor steel.* Faculty of Engineering, University of Wollongong. http://ro.uow.edu.au/theses/3853
7. Shchudro, A., Laukhin, D., Pozniakov, V. (2020) Analysis of the effects of welding conditions on the formation of the structure of welded joints of low-carbon low-alloy steels. *Key Eng. Materials*, **844**, 146–154. DOI: https://doi.org/10.4028/www.scientific.net/KEM.844.146
8. Maksimov, S.Yu., Prilipko, O.O., Berdnikova, O.M. et al. (2021) Controlling the parameters of the metal crystal lattice of the welded joints made underwater. *Metalofizyka ta Novitni Tehnologiyi*, 43(**5**), 713–723 [in Ukrainian]. DOI: https://doi.org/10.15407/mfint.43.05.0713
9. Poznyakov, V.D., Gajvoronskij, A.A., Kostin, V.A. et al. (2017) Features of austenite transformation and mechanical metal properties in the of heat affected zone steel joints of grade 71 at arc welding. *Mehanika ta Mashynobuduvannya*, **1**, 254–260 [in Russian].
10. Zavdoveev, A., Poznyakov, V., Baudin, T. et al. (2021) Effect of nutritional values on the processing properties and microstructure of HSLA rod processed by different technologies. *Materials Today Communications*, **2**, 102598. DOI: https://doi.org/10.1016/j.mtcomm.2021.102598
11. Konat, Ł., Białobrzeska, B., Białek, P. (2017) Effect of welding process on microstructural and mechanical characteristics of Hardox 600 steel. *Metals*, 7(**9**), 349. DOI: https://doi.org/10.3390/met7090349
12. Özdemir, T. (2020) Mechanical and microstructural analysis of armor steel welded joints. *Inter. J. of Eng. Research and Development*, 12(**1**), 166–175. DOI: https://doi.org/10.29137/umagd.488104
13. Sarzhevsky, V.A., Sazonov, V.Ya. (1981) Installation for simulating thermal cycles of welding based on the MCS-75 machine. *Avtomaticheskaya Svarka*, **5**, 69–70 [in Russian].

ORCID

V.D. Poznyakov: 0000-0001-8561-3526,
O.V. Korieniev: 0009-0007-3533-1247

CONFLICT OF INTEREST

The Authors declare no conflict of interest

CORRESPONDING AUTHOR

O.V. Korieniev
E.O. Paton Electric Welding Institute of the NASU
11 Kazymyr Malevych Str., 03150, Kyiv, Ukraine.
E-mail: korenew@ukr.net

SUGGESTED CITATION

V.D. Poznyakov, O.V. Korieniev (2025) Mechanical properties of metal in areas of welded joints of medium-carbon alloy steels heated to temperatures from 350 to 800 °C.
The Paton Welding J., **10**, 12–15.
DOI: https://doi.org/10.37434/tpwj2025.10.02

JOURNAL HOME PAGE

https://patonpublishinghouse.com/eng/journals/tpwj

Received: 02.06.2025
Received in revised form: 01.10.2025
Accepted: 21.10.2025

DOI: https://doi.org/10.37434/tpwj2025.10.03

MODERN APPROACHES TO OBTAINING CONTINUOUS COOLING TRANSFORMATION DIAGRAMS FOR WELDING (REVIEW)

V.V. Zhukov, V.A. Kostin, S.G. Hrygorenko, R.S. Gubatyuk

E.O. Paton Electric Welding Institute of the NASU
11 Kazymyr Malevych Str., 03150, Kyiv, Ukraine

ABSTRACT

The article presents a review of modern approaches to constructing CCT diagrams and special diagrams formed on the basis of the results of a dilatometric experiment for the analysis of structural-phase transformations in steels during cooling. The methodology of physical modeling of thermal cycles on Gleeble installations, as well as typical heating and cooling parameters, is considered. Special attention is paid to the influence of the cooling rate on the formation of the microstructure in the heat-affected zone of welded joints. Approaches using constant and variable (nonlinear) cooling modes are compared with an emphasis on their compliance with real welding conditions. The advantages of nonlinear thermal cycles for increasing the reliability of modeling and correctness of constructing CCT diagrams when assessing the weldability of steels are substantiated.

KEYWORDS: physical modeling, phase transformations, microstructure, austenite, martensite, CCT and DCCT diagrams, Gleeble, welded joints

INTRODUCTION

Continuous cooling transformation (CCT) diagrams of overcooled austenite decomposition are an important tool for analysis of the structural-phase transformations in steels during cooling. They reflect how the austenite structure changes at different cooling rates, i.e. how the phase (ferrite, pearlite, bainite or martensite) is formed, depending on the temperature and time [1–3].

Using the CCT diagrams specialists can:

- Predict the structure in each HAZ — know whether martensite (leading to brittleness) or ferrite/pearlite (ensuring the ductility) are formed;
- Assess the risk of cold cracking, which is often associated with appearance of martensite at rapid cooling;
- Select the welding modes (current, welding speed, preheating/additional heating), so as to reduce the harmful structural changes;
- Determine the need for postweld heat treatment.

Thus, CCT diagrams are extremely important in welding critical structures — from pipelines to armour, where control of the metal structure and properties in the HAZ is required.

A dilatometric experiment is the base of experimental plotting of CCT diagrams. This is a method of studying phase transformations in materials based on measurement of changes in the linear dimensions of the sample during the thermal cycle (heating or cooling). It is conducted using a dilatometer — a high-precision instrument, which records the material deformation with micron accuracy at temperature change. A steel sample is heated up to austenitization temperature (above A_{c3}), and held for a certain time for structure stabilization. Then, the sample is cooled down at a constant specified rate (for instance, 1 °C/s). During cooling, the dilatometer records the change in sample length in real time. In the phase transformation points (austenite-ferrite, pearlite, bainite, etc.) jumplike or characteristic changes of the deformation curve occur, which are recorded by the instrument [4]. In Ukraine, unfortunately, there is still no standard which specifies the CCT diagram construction, as well as conducting the dilatometric experiment.

ASTM A1033-18 (2023) Standard [5] entitled “Standard Practice for Quantitative Measurement and Reporting of Hypoeutectoid Carbon and Low-Alloy Steel Phase Transformations”, describes a procedure for quantitative measurement and presentation of phase transformations in hypoeutectoid carbon and low-alloy steels, using high-speed dylatometry. In Section 1.3 of this Standard it is noted that the procedure is used to determine the behaviour of phase transformations in steels, both under the isothermal conditions and under the conditions of continuous cooling. Although the CCT diagram term is not used directly, the described methods allow obtaining data, required to plot such diagrams. Thus, the Standard does not contain any direct reference to CCT diagrams, but provides a methodology, which allows obtaining information for their construction.

In ASTM A1033-18 Standard (2023) the procedure for plotting these phase transformations envisages using linear (i.e. constant) cooling rates. If it is impossible to control the constant rate, (for instance,

in the real technological process), it is necessary to record the instantaneous cooling rate at 700 °C and cooling duration in the range of 800–500 °C.

THE OBJECTIVE OF THE WORK

is to analyze the modern methods of construction of CCT diagrams of phase transformations under the conditions of welding, with the purpose of taking into account the complex temperature-mechanical influences and the nonlinear nature of the thermal cycle of welding.

Quite often the CCT diagrams, plotted with application of constant cooling rates, are used to assess the structural-phase composition of steels in the HAZ. For instance, in [6] the microstructural transformations in the HAZ of pipeline steel X70 (C — 0.06 %; Mn — 1.28 %; Si — 0.26 %; Nb — 0.045 %; Ti — 0.014 %; Mo — 0.17 %.) during the thermal cycles of welding were studied. Experiments were conducted in Gleeble 3500 installation. To study the phase transformations, the samples were heated at the rate of 10 °C/s up to the maximal temperature of 1300 °C, then cooled to 900 °C in 1 s, held for 16 s at this temperature, and then cooled to room temperature at constant cooling rates from 60 to 0.1 °C/s. It should be noted that the diagram was plotted at the temperature of 900 °C. The authors conclude that the optimal cooling rate to ensure the HAZ strength and toughness is equal to 10–20 °C/s (Figure 1).

Work [7] presents the construction of a CCT diagram for the HAZ of carbon steel SA106 Grade B (C — 0.3 %; Mn — 0.7 %; Si — 0.1 %; Cr — 0.4 %; Cu — 0.4 %; Mo — 0.15 %; Ni — 0.4 %; V — 0.08 %). The objective of the study was evaluation of the phase transformations and the microstructure, which form in the HAZ at different cooling rates, which reproduces the arc welding conditions.

The dilatometric experiment was conducted in Gleeble 3500 installation. Samples were heated at the rate of 100 °C/s up to 1200 °C, held at this temperature for 1 s and cooled to room temperature at the specified constant rates from 0.1 to 100 °C/s. The general conclusions indicate that the optimal cooling range to form a favorable structure is 10–20 °C/s. The derived CCT diagram is recommended for development of technologies for welding steel SA106 Grade B (Figure 2).

In work [8] the influence of different cooling rates on the HAZ microstructure was studied and a CCT-diagram was constructed for the conditions of welding CLAM steel (China Low Activation Martensitic, C — 0.093 %; Cr — 8.39 %; W — 1.499 %; V — 0.196 %; Ta — < 0.01 %; Mn — 0.44 %), which is a ferritic-martensitic steel designed for application in nuclear reactors.

Physical modeling was performed in Gleeble-1500 installation. The thermal cycle included heating up to the temperature of 1623 K (~ 1350 °C) in 2 min, holding for 1 min and cooling to room temperature at constant cooling rates in the range of 3600–1 K/min (60–0.017 °C/s). The plotted CCT diagram has only two regions of phase transformations: ferritic and martensitic. The authors note that that the diagram allows predicting the HAZ structure, and it is a useful tool to assess the weldability of CLAM steel (Figure 3).

Although the authors present the above-considered works on CCT diagram construction as studies of the HAZ influence on the steel structure in welding, the cooling rate ranges used during CCT diagram construction in these works are very similar to those applied in the works on CCT diagram construction for determination and optimization of the heat treatment cycles.

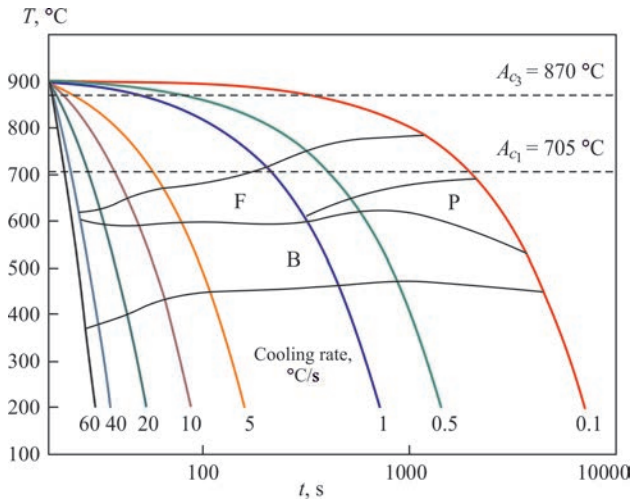

Figure 1. CCT diagram of pipe steel X70. Microstructures: F — ferrite; B — bainite; P — pearlite [6]

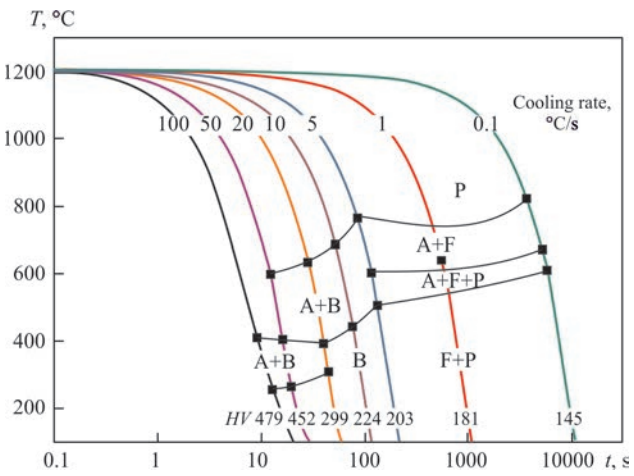

Figure 2. CCT diagram of steel SA106 Grade B. Microstructures: A — austenite; F — ferrite; B — bainite; P —pearlite; M — martensite [7]

In [9] the behaviour during continuous cooling of steel similar to the ferritic-martensitic CLAM steel in [8] was studied. The main objective is construction of CCT diagram and studying the influence of the cooling rate on phase transformation and microhardness. In this work, however, the efforts were focused on development of heat treatment of this steel.

Physical modeling was conducted in Gleeble 1500 installation. The samples were heated to 1253 K (≈ 980 °C) in 15 min, held for 30 min, and then cooled to room temperature at the rates from 240 K/min (4 °C/s) to 1 K/min (0.017 °C/s). All the thermal cooling cycles were conducted at a constant rate. The authors note that the obtained results can be used to develop heat treatment modes with predicted phase composition in the critical zones of nuclear reactor structures (Figure 4).

The conditions of plotting the CCT diagrams differ for each case, and conducting the dilatometric experiment essentially is physical modeling of the technological influence on the material. If during the technological processing of the material, the thermal influence is accompanied by deformational impact, it should be taken into account, when studying the kinetics of the phase-structural transformations.

A description of the so-called DCCT diagrams (Deformation Continuous Cooling Transformation) is sometimes found in publications. Such diagrams are used for optimization of the modes of thermodeformational treatment and they appeared due to the need to allow for the influence of thermodeformational treatment on the kinetics of structural-phase transformations. So, work [10] is a study of the influence of prior plastic deformation on the nature of CCT diagram of spring steel 51CrV4 (C — 0.47–0.55 %; Si — ≤ 0.40 %; Mn — 0.70–1.10 %; P — ≤0.025 %; S — ≤0.035 %; Cr — 0.90–1.20 %; V — 0.10–0.25 %).

Both a standard CCT diagram and a DCCT diagram, which allows for the deformation before cooling of 51CrV4 steel (Figure 5) were plotted in Gleeble 3800 simulator.

To construct the CCT diagrams without deformation, the samples were heated to 850 °C, held for 120 s and were cooled at constant rates in the range of 0.16–12 °C/s. In the cycles with deformation, the samples after similar holding were uniaxially compressed at 850 °C with true deformation of 0.35 at the rate of 1 s^{-1}, and then cooled at the same rates. The cooling rate was constant for all the cooling cycles.

DCCT diagram showed a shift of the curve of the start of pearlitic transformation to the left (to the region of higher cooling rates), i.e. pearlite formed faster. The curve of the start of the bainitic transformation somewhat shifted upwards (to higher temperatures),

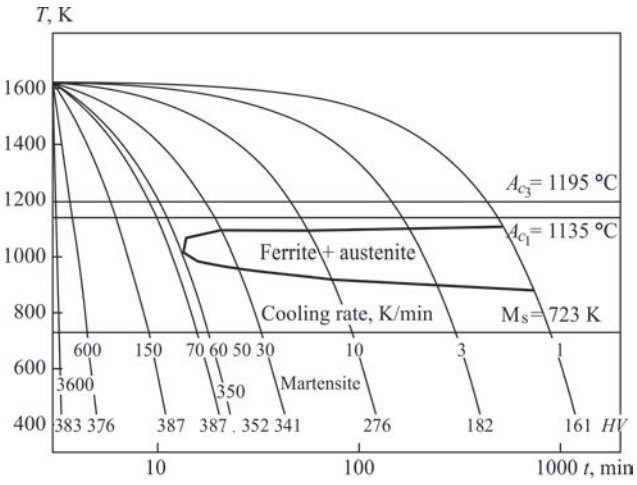

Figure 3. CCT diagram of CLAM steel HAZ [8]

and there appeared also the curve of the end of bainitic transformation. The curve of the start of martensitic transformation has declined a little in the zone of high rates. On the whole, deformation accelerates the anisothermal decomposition of austenite for this steel, which is particularly noticeable for the pearlitic component.

Note that for deformed metal there is a tendency for the transformation acceleration under the conditions of continuous cooling, compared to metal without deformation.

For instance, in [11] the authors studied the influence of chromium content and prior deformation of austenite on the shape of CCT and DCCT diagrams for low-carbon bainitic steels. The objective of the work was to asses how the structure and hardness change, depending on the composition, cooling temperature and deformation. Three steels with the same content of carbon (~ 0.033 %), manganese (~ 0.9–1 %) and niobium (~ 0.06 %), but with different chromium concentration: 3.97 % (A), 2.52 % (B) and 1.02 % (C) were studied (Figure 6). All the samples were heated up to the temperature of 1100 °C at the rate of 10 °C/s and were held for 3 min. In order to construct the CCT

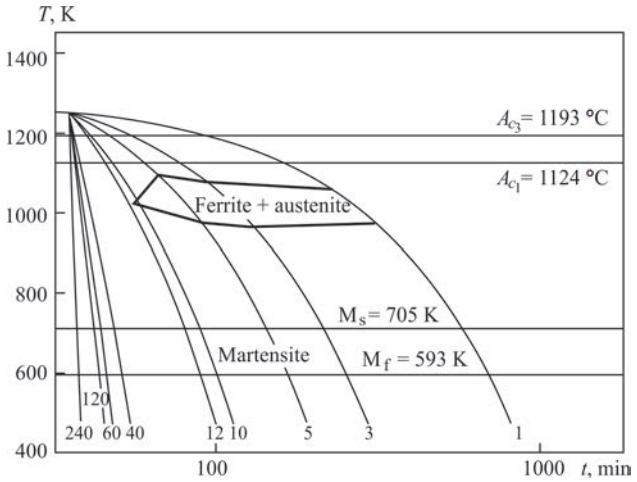

Figure 4. CCT diagram of CLAM steel for heat treatment [9]

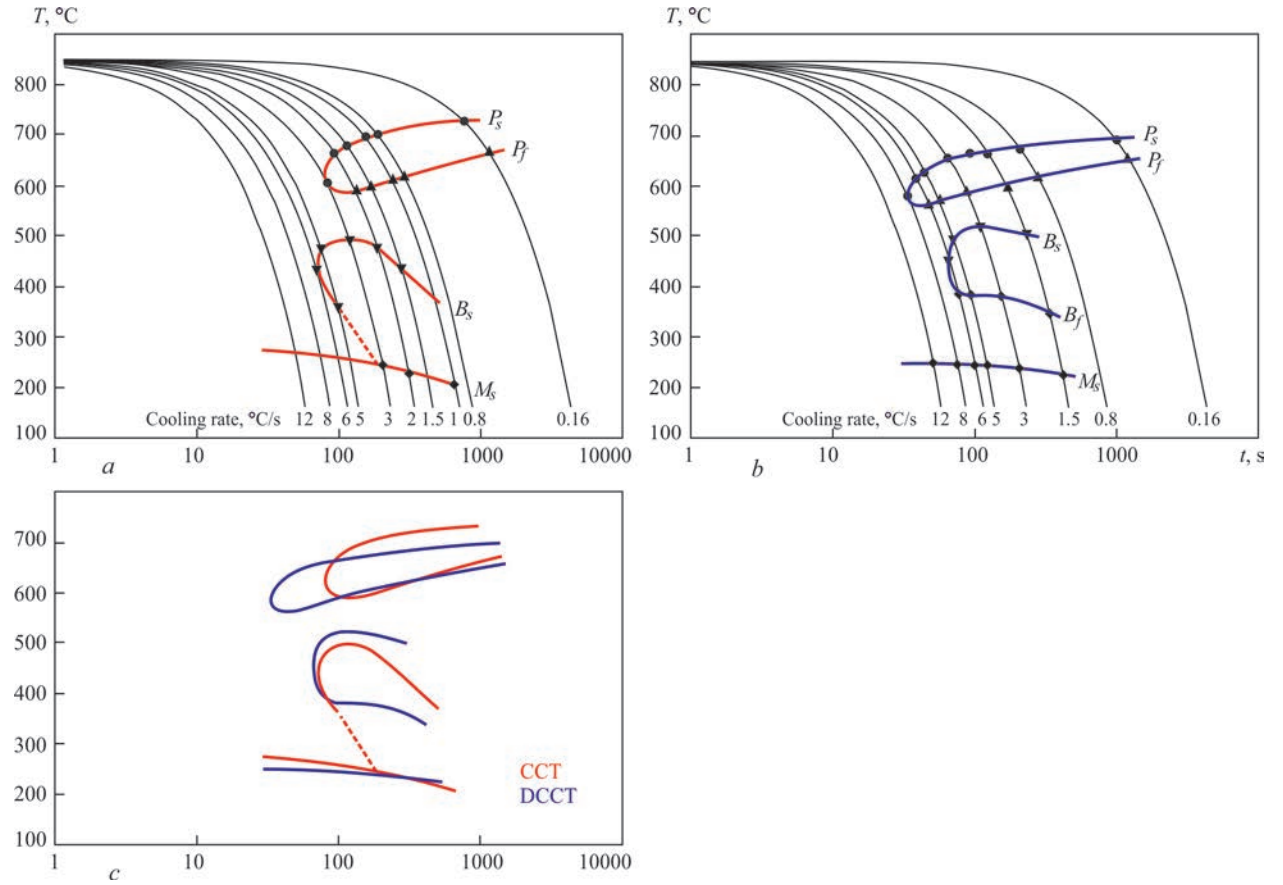

Figure 5. Influence of prior plastic deformation on the kinetics of austenite transformation for 51CrV4 steel: *a* — CCTdiagram of steel without deformation; *b* — DCCT diagram of steel with prior deformation; *c* — comparison of CCT and DCCT diagrams. Temperatures: P_s — start of pearlitic transformation; P_f — finish of pearlitic transformation; B_s — start of bainitic transformation; M_s — start of martensitic transformation [10]

diagrams, the samples were cooled to room temperature after holding with different cooling rates, which varied from 2 to 80 °C/s. For plotting the DCCT diagrams, the samples were cooled after holding at the rate of 2 °C/s to the temperature of 880 °C. The samples were held at this temperature for 15 s, and then compressive deformation was applied to them with 0.6 total strain and strain rate of 1 s^{-1}. After deformation, the samples were soaked for another 20 s, and then cooled to room temperature at different cooling rates in the range from 2 to 80 °C/s.

It should be noted that the deformational impact leads to lowering of the temperatures of the start of austenite transformation and to shifting of the ferrite phase appearance towards higher cooling rates (Figure 6). Increase of chromium content improves the hardenability, lowers the phase transformation temperatures, increases the fraction of bainite and reduces the structure sensitivity to deformation. Contrarily, at a low Cr content the deformation stimulates the ferrite formation and essentially changes the transformation kinetics. The authors note that in order to form a completely bainitic structure it is necessary to avoid ferrite and pearlite, which can be achieved at Cr content in the range of 2.5–4 % and cooling rates above 20 °C/s (Figure 6).

Allowing for deformational impact on the nature of structural-phase transformations is of direct importance in welding. Thermal deformations arising in welding, depending on the structural features of the product being welded, can influence the kinetics of austenite transformation.

For instance, work [12] presents a new approach to analysis of material proneness to developing residual stresses in the welded joint HAZ – so-called "welding thermal stress diagrams" (WTSD). Unlike the classical CCT diagrams, which describe the phase transformations, without taking into account the mechanical limitations, the WTSD diagrams allow directly assessing how the real welding temperature cycles influence the development of stresses in the metal.

Selected for analysis was a high-strength low-alloy steel of ferritic-bainitic class (C — 0.12 %; Si — 0.07 %; Mn — 1.73 %; P — 0.023 %; S — 0.003 %; Al — 0.042 %). The samples were fixed in rigid grips of thermomechanical simulator Gleeble 3550-GTC, which allowed completely blocking the sample elongation during heating and cooling. This ensured development of internal stresses, similar

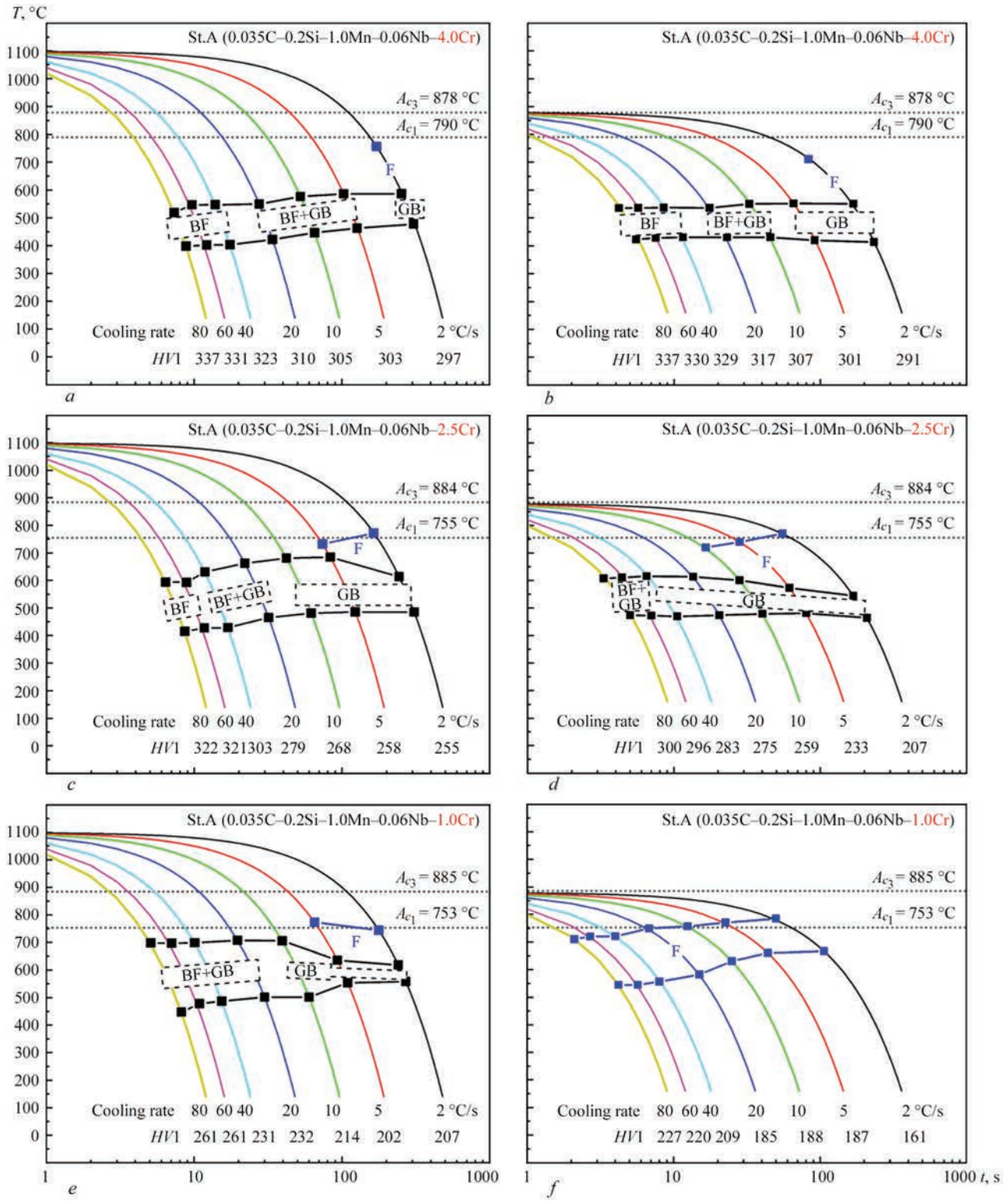

Figure 6. Influence of chromium content and prior plastic deformation on the kinetics of austenite transformation in low-carbon bainitic steels with different chromium content of 3.97 % (A), 2.52 % (B) and 1.02 % (C): *a*, *c*, *e* — CCT diagrams; *b*, *d*, *f* — DCCT diagrams of steels. Microstructures: BF — bainitic ferrite; GB — granular bainite; F — ferrite [11]

to those formed in the real welded joints. In the work modeling of various HAZ subzones was conducted, which differed by the maximal heating temperature: 1350 °C for coarse-grained HAZ (CGHAZ), 1100 °C for fine-grained HAZ (FGHAZ), 900 °C for intercritical HAZ (ICHAZ) and 700 °C for subcritical HAZ (SCHAZ). After the maximal heating temperature has been reached, cooling was performed at different cooling rates, equal from 10 to 100 °C/s (in the range of 800–500 °C). It should be noted that for modeling the cooling the authors of the work used not only the constant cooling rates, but temperature cycles based on modified Rozenthal equations [13] — analytical solutions for temperature fields during weld-

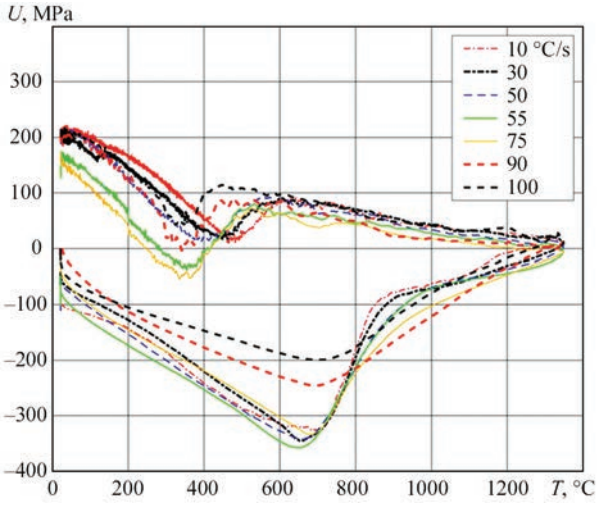

Figure 7. WTSD diagram for high-strength low-alloy steel [12]

ing, allowing for the speed of heat source movement, material thermal conductivity and other parameters. During the experiment, the reactive forces, i.e. the force generated in response to the thermal expansion and compression of the sample, were recorded. These characteristics were used to determine the magnitudes of mechanical stresses (thermal and residual), plotted as the function of temperature. This allowed obtaining diagrams of σ–*T* type (stress — temperature) for each mode (Figure 7).

Result analysis revealed (Figure 7) that the maximal residual stresses do not always arise at the highest or lowest cooling rates, as is commonly believed. For examples, maximal stresses were recorded in the CGHAZ zone at a medium cooling rate of 50 °C/s. The reason for this is a complex interaction between the phase transformations (particularly, formation of martensite) and limitation of thermal expansion.

In the conclusions the authors state that WTSD is an efficient tool for assessment and simulation of residual stresses in welded joints, particularly, when using modern steels sensitive to cracking. This method can be also used for calibration of numerical models of stresses and mechanical properties of the metal after welding.

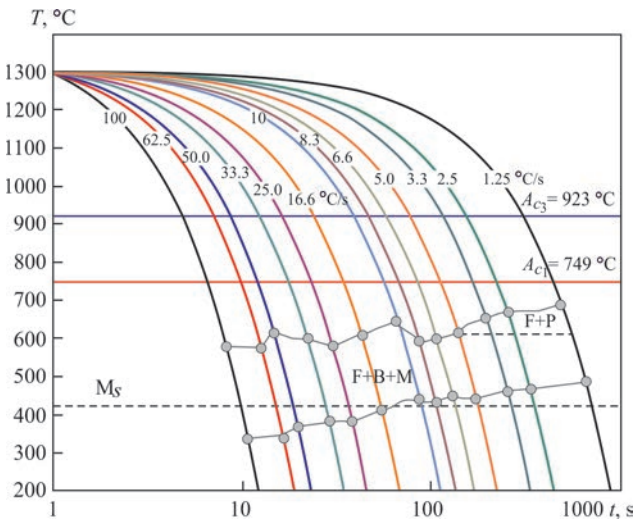

Figure 8. CCT diagram for 700MC steel. Microstructures: F — ferrite; B — bainite; P — pearlite; M — martensite; M_s — start of martensitic transformation [14]

Under the real conditions of the welding process, metal cooling occurs at a changing rate, which depends on the heat removal, joint geometry, welding mode and other factors. Linear modes do not reflect these peculiarities, so they do not allow adequate modeling of the structural transformations in the HAZ. Use of nonlinear cycles close to the real ones ensures higher reliability of the results, and allows a more accurate reproduction of the conditions of microstructure formation in the welded joint.

In [14] application of nonlinear thermal cycles for CCT diagram construction is substantiated by the inconsistencies and errors in the diagrams, plotted using constant cooling rates, and the desire to bring physical modeling closer to the real welding conditions. The work presents the results of physical modeling of the structure and phase transformations in the CGHAZ of structural steel 700MC (C — 0.065 %; Mn — 1.82 %; Al — 0.025 %; Cu — 0.0115 %; Cr — 0.025 %; Ni — 0.037 %; V — 0.014 %; Nb — 0.053 %; Ti — 0.102 %) (Figure 8).

Modeling was performed in Gleeble 3800 installation. Peak temperature of 1300 °C was selected for CGHAZ modeling, which corresponds to the temperature field near the weld. Heating rate was equal to 100 °C/s with soaking for 1 s at maximal temperature. 13 variants of cooling at the rate from 1.25 up to 100 °C/s were realized. The cooling cycles were nonlinear with application of Rykalin model [15]. This model also is an analytical scheme of heat transfer, which allows for temperature distribution in massive welded parts, taking into account the material geometry, heat conductivity and density. Its application is due to the need to accurately model the heterogeneous thermal conditions in thick-walled welded structures, where the linear models give significant errors. The authors came to the conclusion that accurate physical modeling of CGHAZ with application of nonlinear thermal cycles allows reliably plotting the CCT diagrams, specific exactly for welding. In particular, during optimization of the welding modes for 700MC steel the cooling rates above 25 °C/s should be avoided, so as to prevent excess martensite formation, which is accompanied by an increase in hardness and lowering of metal toughness in the HAZ.

The main objective [16] was to study the influence of the cooling mode on the structural-phase composition of the HAZ metal of 15Kh2NMFA steel, used in the bodies of WWER-1000 reactors in arc surfacing.

The authors tried to compare the theoretical concepts based on standard thermokinetic diagrams, with the real conditions of structure formation during welding/surfacing. As the real surfacing process is characterized by nonlinear cooling, which is considerably different from the linear cycles, both physical modeling maximum close to the welding/surfacing conditions, and a number of experiments using the linear cooling cycles were conducted. The authors sought to verify how the real conditions will influence the formation of the final microstructure. In order to plot the classical thermokinetic diagrams the samples of 15Kh2NMFA steel were heated to1000 °C, held at this temperature for 170 min, and then cooled at different constant rates (1, 3, 5 and 7 °C/s).

When modeling cycles close to the real welding conditions, two series of experiments were conducted in which the samples were heated to 1000 or to 1350 °C. Then the samples were cooled at the rates of 3, 4 and 5 °C in the range of 800–500 °C for both the series. All the experimental work was conducted in Gleeble 3800.

A key difference of the real surfacing cycles from the linear ones (for plotting the CCT diagrams) is an extremely short time of the metal staying at the austenitization temperature (~ 1 s). During short holding and further cooling under the conditions close to the surfacing ones, the metal can form a totally martensitic structure, whereas during linear cooling at similar cooling rates a bainitic-martensitic structure is formed.

A change in the maximal heating temperature (1000 against 1350 °C) practically did not influence the kinetics of the martensite phase formation, and only slightly affected the temperatures of the start/finish of phase formation. However, this change influenced the maximal fraction of the phases in the final microstructure, which points to the importance of allowing for the peak cycle temperature.

The authors of the work convincingly showed that the cooling mode, in particular the nonlinearilty and the extremely short time of staying at the austenitization temperature, is of a decisive importance for formation of the structural-phase composition in the HAZ of 15Kh2NMFA steel. Application of standard CCT diagrams constructed on the base of linear cooling cycles with a long holding time does not allow adequately predicting the microstructure under the conditions of the real welding process. For accurate prediction it is necessary to use experimentally plotted CCT diagrams, derived under the conditions maximum close to the actual thermal cycles of surfacing, allowing for the specifics of their nonlinearity and the short time of austenitization.

CONCLUSIONS

1. Continuous cooling transformation diagrams (CCT) are an important tool to predict the structure in the heat-affected zone of welded joints. Their construction is based on dilatometric experiments with a constant cooling rate. Such an approach, however, only partially corresponds to the real welding conditions.

2. The deformation continuous cooling transformation diagrams (DCCT) allow for the influence of plastic deformation, which can significantly change the phase transformation kinetics, in particular, accelerate formation of pearlite and bainite and lower the temperature of martensitic transformation.

3. Allowing for the complex temperature-mechanical effects (residual stresses, real temperature gradients, etc.) enables more accurately predicting the possible level of residual stresses, depending on the material cooling rate.

4. Nonlinear thermal cycles, which model the real cooling during welding, provide more accurate correspondence of the phase transformations with the actual welding conditions. Their application allows construction of more relevant diagrams, and avoiding the errors inherent in linear models.

5. Physical modeling in Gleeble installations remains the key method to investigate the thermal behaviour of steels in welding under the condition of correct setting up of the experiment, allowing for both the temperature and deformation parameters.

REFERENCES

1. Atkins, M. (1980) *Atlas of continuous cooling transformation diagrams for engineering steels*. Rev. U.S. Ed. Metals Park, Ohio, ASM International.
2. Seyffarth, P., Meyer, B., Scharff, A. (1992) *Großer atlas schweiß-ZTU-Schaubilder*. Düsseldorf, Deutscher Verlag für Schweißtechnik, DVS-Verl.
3. Zhang, Z., Farrar, R. A. (1995) *An atlas of continuous cooling transformation (CCT) diagrams applicable to low carbon low alloy weld metals*. London, The Institute of Materials.
4. Kostin, V.A., Zhukov, V.V. (2021) Improvement of the procedure of analysis of thermokinetic diagrams of phase transformations in metal of high-strength low-alloy steel welds. *Suchasna Elektrometalurhiya*, **2**, 40–46 [in Ukrainian]. DOI: https://doi.org/10.37434/sem2021.02.06
5. (2023) ASTM A1033-18: *Standard practice for quantitative measurement and reporting of hypoeutectoid carbon and low-alloy steel phase transformations*. ASTM International. DOI: https://doi.org/10.1520/A1033-18R23
6. Li, H., Liang, J.-L., Feng, Y.-L., Huo, D.-X. (2014) Microstructure transformation of X70 pipeline steel welding heat-affected zone. *Rare Metals*, 33(**4**), 493–498. DOI: 10.1007/s12598-014-0344-x
7. Vimalan, G., Muthupandi, V., Ravichandran, G. (2018) Construction of continuous cooling transformation (CCT) diagram using gleeble for coarse grained heat affected zone of SA106 grade B steel. In: *Proc. of Conf. on AIP*, **1966**, 020013. DOI: https://doi.org/10.1063/1.5038692

8. Zheng, S., Wu, Q., Huang, Q., Liu, S., Han, Y. (2011) Influence of different cooling rates on the microstructure of the HAZ and welding CCT diagram of CLAM steel. *Fusion Eng. and Design*, **86**, 2616–2619. DOI: https://doi.org/10.1016/j.fusengdes.2011.02.072
9. Wu, Q.-s., Zheng, S.-h., Huang, Q.-y., Liu, S.-j., Han, Y.-y. (2013) Continuous cooling transformation behaviors of CLAM steel. *J. of Nuclear Materials*, **44**2, S67–S70. DOI: https://doi.org/10.1016/j.jnucmat.2013.03.072
10. Kawulok, R., Schindler, I., Kawulok, P. et al. (2015) Effect of plastic deformation on CCT diagram of spring steel 51CrV4. In: *Proc. of Conf. on METAL 2015*, 345–350.
11. Ali, M., Kaijalainen, A., Hannula, J. et al. (2020) Influence of chromium content and prior deformation on the continuous cooling transformation diagram of low-carbon bainitic steels. *Key Eng. Materials*, **835**, 58–67. DOI: https://doi.org/10.4028/www.scientific.net/KEM.835.58
12. Mishchenko, A., Scotti, A. (2021) Welding thermal stress diagrams as a means of assessing material proneness to residual stresse. *J. of Materials Science*, **56**, 1694–1712. DOI: https://doi.org/10.1007/s10853-020-05294-y
13. Rosenthal, D. (1946) The theory of moving sources of heat and its application to metal treatments. *Transact. of the American Society of Mechanical Eng.*, 68(**8**), 849–866. DOI: https://doi.org/10.1115/1.4018624
14. Roshan, R., Naik, A.K., Saxena, K.K., Msomi, V. (2022) Physical simulation on joining of 700MC steel: A HAZ and CCT curve study. *Materials Research Express*, 9(**4**), 046522. DOI: https://doi.org/10.1088/2053-1591/ac6792
15. Rykalin, N.N. (1960) Calculation of heat processes in welding. In: *42nd Annual Meeting of the American Welding Society*.
16. Lobanov, L.M., Kostin, V.A., Makhnenko, O.V. et al. (2020) Forecasting of structural transformations in HAZ steel of 15Kh2NMFA at anti-corrosion cladding. *Problems of Atomic Sci. and Technology*, 126(**2**), 89–96. DOI: http://dx.doi.org/10.46813/2020-126-089

ORCID
V.V. Zhukov: 0000-0002-3358-8491,
V.A. Kostin: 0000-0002-2677-4667,
S.G. Hrygorenko: 0000-0003-0625-7010,
R.S. Gubatyuk: 0000-0002-0851-743X

CONFLICT OF INTEREST
The Authors declare no conflict of interest

CORRESPONDING AUTHOR
V.V. Zhukov
E.O. Paton Electric Welding Institute of the NASU
11 Kazymyr Malevych Str., 03150, Kyiv, Ukraine.
E-mail: zhukov.kyiv@gmail.com

SUGGESTED CITATION
V.V. Zhukov, V.A. Kostin, S.G. Hrygorenko, R.S. Gubatyuk (2025) Modern approaches to obtaining continuous cooling transformation diagrams for welding (Review).
The Paton Welding J., **10**, 16–23.
DOI: https://doi.org/10.37434/tpwj2025.10.03

JOURNAL HOME PAGE
https://patonpublishinghouse.com/eng/journals/tpwj

Received: 09.06.2025
Received in revised form: 08.08.2025
Accepted: 21.10.2025

DOI: https://doi.org/10.37434/tpwj2025.10.04

RESTORATION OF BELLS AND ART PRODUCTS MADE OF COPPER ALLOYS

T.B. Maydanchuk, A.M. Bondarenko, V.M. Ilyushenko, E.P. Lukianchenko

E.O. Paton Electric Welding Institute of the NASU
11 Kazymyr Malevych Str., 03150, Kyiv, Ukraine

ABSTRACT

The results of experimental work on the restoration of art castings from copper alloys are presented. It is shown that an individual approach is required during product repair, which is associated with the different chemical composition and presence of defects in the cast metal, the shape and size of the product, the need to adjust the chemical composition of welding consumables, etc. It is determined that when restoring bells, the most appropriate process for performing repair work is the process of manual argon-arc welding with a nonconsumable electrode (TIG process). It is shown that positive results in welding up cracks in church bells while ensuring their high acoustic properties are achieved with the correct choice of filler material. Coated-electrode welding can be recommended for welding up casting defects, as well as for manufacturing welded components of sculptures.

KEYWORDS: foundry bronzes, chemical composition, bell bronze, cracks, repair and welding technologies, metal-cored wire, coated electrodes

INTRODUCTION

Owing to their special physical-mechanical and technological properties, copper and its alloys are finding wide application in different sectors of industry and construction. There is not a single industry, where copper and its low and complex alloys are not used. High casting and decorative properties of the copper alloys have made them indispensable for many centuries (starting with the Bronze age) in the production of art and jewelry products: sculptures, monuments, decorations, etc.

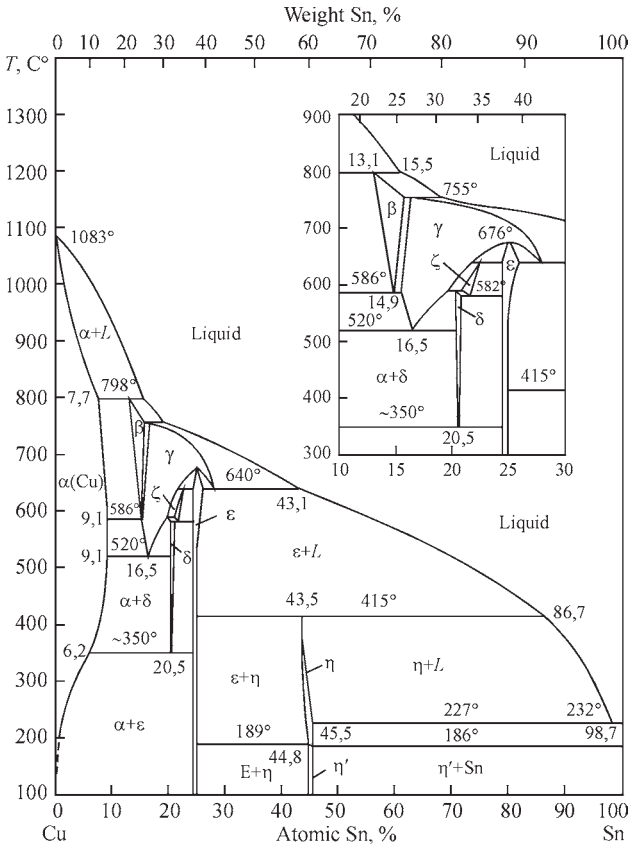

Figure 1. State diagram of Cu–Sn system [1, 2]

The most common alloy for these purposes is tin bronze of Cu–Sn–Zn–Pb system, which in the form of cast material has high fluidity, slight shrinkage, readily fills even complex casting moulds, ensures "bronze colour" of the products and their high corrosion resistance. The state diagram of copper-tin system is shown in Figure 1 [1, 2].

A characteristic feature of the structure of tin bronzes is the fact that during solidification the area of the solid α-solution becomes narrower and (α+β) eutectoid (its base is $Cu_{31}Sn_8$ electron compound with 32.53 wt.% Sn content) appears at Sn concentrations much smaller that it follows from the equilibrium state diagram [2]. This is due to the low rate of tin diffusion into copper, when at rapid transition of tin bronzes from the liquid into the liquid–solid and solid states the tin atoms do not have enough time to occupy all the nodes in the atomic lattice of the centers and crystals of the forming alloy. As a result, the crystals of the solid α-solution contain much less tin than it follows from the equilibrium diagram. Here, the molten alloy which did not crystallize, is enriched in tin in those parts of the ingot, which are the last to crystallize [3, 4]. With increase of the tin content the strength considerably increases and the ductility of the alloy decreases (Figure 2) [5].

Chemical composition of the casting bronzes for art castings is given in Table 1 [6, 7].

According to the current standards, casting bronzes of CuSn5Zn5Pb5, CuSn4Zn7Pb5, CuSn4Zn4Pb17, CuSn3Zn12Pb5, CuSn6Zn6Pb3 grades also belong to

alloys of this system. These bronzes are the best studied, and in our opinion, they can also be used as material for art casting (in one composition or another).

The given bronzes of BKh and CuSnZnPb grades belong to low-tin bronzes (≤5–6 % Sn), and at higher Sn concentration — to high-tin ones (CuSn8Zn4, CuSn10P1, CuSn10Zn2, CuSn108Zn10). Tin increases the mechanical properties (Figure 2) and corrosion resistance of the bronzes. The "bell" bronze well-known from ancient times also belongs to high-tin ones, its optimal composition being 20–23 % Sn, up to 2 % impurities, the balance being Cu [8]. It is this composition of bronze that ensures its sufficient strength and satisfactory sound qualities, which is particularly important in manufacture of such products as church bells.

Low-tin bronzes with zinc and lead additives are usually used for art casting. They improve the alloy casting properties, and facilitate the further machining of the products. A well-suited material for making art products (sculptures of various shapes, souvenirs, decorations, etc.) are also copper-based alloys, less expensive compared to tin bronzes: copper-zinc alloys (brasses), copper-aluminium alloys (aluminium bronzes), and silicon-manganese bronzes.

The given information as regards the alloys for art castings is necessary, first of all, for clear understanding what metal we are dealing with in the case of restoration repair of a product. The need to conduct such repair work arises both in the case of extending the service life of a product, and even at the production stage (welding up casting defects). Practical experience of welding cast bonzes shows that such alloys belong to the category of material with limited weldability, and their welding is a complex and critical operation.

THE OBJECTIVE

of the work is determination of the chemical composition and structural features of the damaged works of art from copper alloys and development of special welding consumables and welding technology on their base to restore the product integrity.

Beginning from the 50s of the previous century, PWI has conducted systematic studies of copper alloy weldability and development of the technological processes of their welding and surfacing. This work was usually performed with the purpose of solving the urgent problems of application of these materials in such sectors as mechanical engineering and shipbuilding, metallurgical and electrical engineering industry.

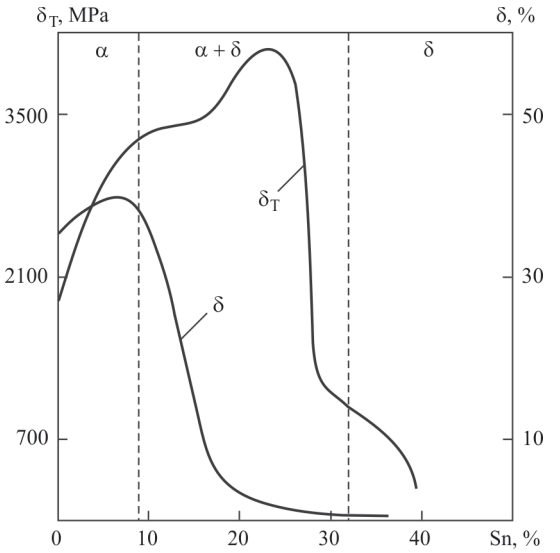

Figure 2. Dependence of mechanical properties of tin bronzes on tin content

Considering the available developments on welding consumables (flux-cored wires, coated electrodes) and technological processes of welding and surfacing of structural copper alloys, PWI Department of general problems of arc welding equipment and technology has conducted scientific-practical works on reconditioning and restoration of art castings from copper alloys. Results of some of them are given below.

RESTORATION OF CHURCH BELLS

Church bells which had to be restored had the characteristic classical shape (Figure 3).

As noted in work [9], the main criteria of the quality of church bells are their melodiousness and art design, as well as absence of defects (pores, cracks, nonmetallic inclusions), which can lead to their fast fracture. A detailed study of bell bronze demonstrated that it is exactly the copper alloy with 20–22.5 % tin (impurity content within 1–2 %) which has high acoustic properties in the cast untreated state. It should be noted that even a slight change of the chemical composition leads to significant changes in the structure and properties of bell bronze (Figure 4) [10].

Table 1. Composition of cast bronzes for art castings [6, 7]

Bronze grade	Sn	Zn	Pb	Cu	Additives				Application
					Sb	Fe	Al	Total	
BKh1	4–7	5–8	1–4	Bal.	1.0	1.0	0.1	3.0	Castings for busts and statues
BKh2	1–5	8–13	1–6		1.0	1.0	0.1	3.0	Large-sized decorative castings
BKh3	0,5–3	25–35	1–3		0.5	1.0	0.5	3.0	Small-sized decorative castings
Bell bronze	20–23	*	*		*	*	*	*	Bell castings

Notes. BKh1 — for producing busts, sculptures; BKh2 — for large-sized decorative castings; BKh3 — for small-sized decorative castings; * — not regulated, but not more than 2 %.

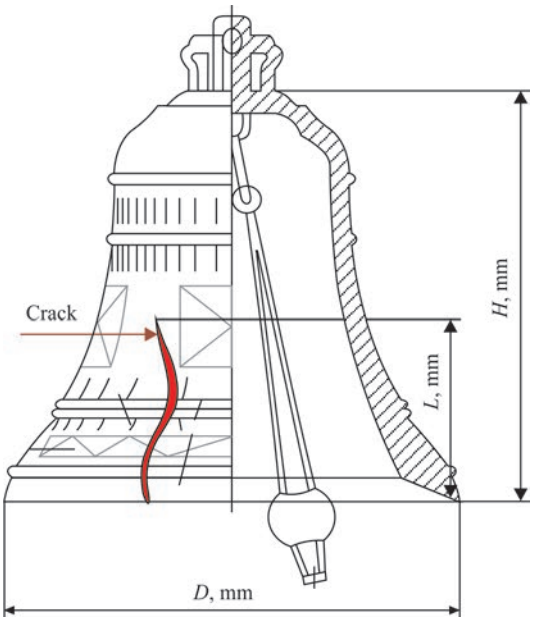

Figure 3. Generalized profile of the bells to be restored [8]

As shown by investigations [11], taking into account the service conditions (impact load, metal aging, atmospheric corrosion, etc.), the acoustic properties of bell bonze decrease abruptly. However, the bells become unfit for purpose the most often because of crack initiation in them (Figure 5).

Several bells of different size (and from different manufacturers) with exactly such defects were submitted for repair. Tables 2 and 3 give the data on overall dimensions of the bells and chemical composition of the bronze.

Visual inspection of the bells showed that the cracks initiate in the bell lower parts (bell percussion belt) and propagate upwards. It should be noted that in terms of design the bell walls have variable thickness: maximal in the percussion belt and much smaller in the upper part. So, the metal of the longest crack in K-2 bell was 8 mm thick in its upper part, and the metal of the percussion belt of K-3 bell was 48 mm thick. Crack welding up actually consists of making a butt weld of metal of a variable thickness, which is under rigid restraint.

It is known from published sources that soldering and welding methods are used in bell repair. The authors of [12] report that they managed to repair a bell with application of soldering, using copper-based powders as the filler material. In work [13], rods of similar bell material produced by casting were used. The authors of [14] in their applied research experiments on restoration of the integrity of bells of the 16th and 19th centuries used both the soldering and welding methods. Here, similar to work [15], prior to repair the bell was completely preheated and slowly cooled. Such a technology, however, is costly, and it does not always yield positive results. Therefore, in our opinion, a more rational and economically sounder welding process for performance of repair work on bell restoration is the TIG-process without preheating with application of special filler wires. Such metal-cored wires provide a weld metal close to the bell bronze by its composition, and to its acoustic properties, respectively.

The crack tip is traditionally drilled out before scraping (Figure 6). Taking into account the metal thickness, crack welding up is performed from both sides by multipass welds formed by deposition of small (8–10 mm) beads (Figure 7), each of them being additionally peened to lower the thermal stresses.

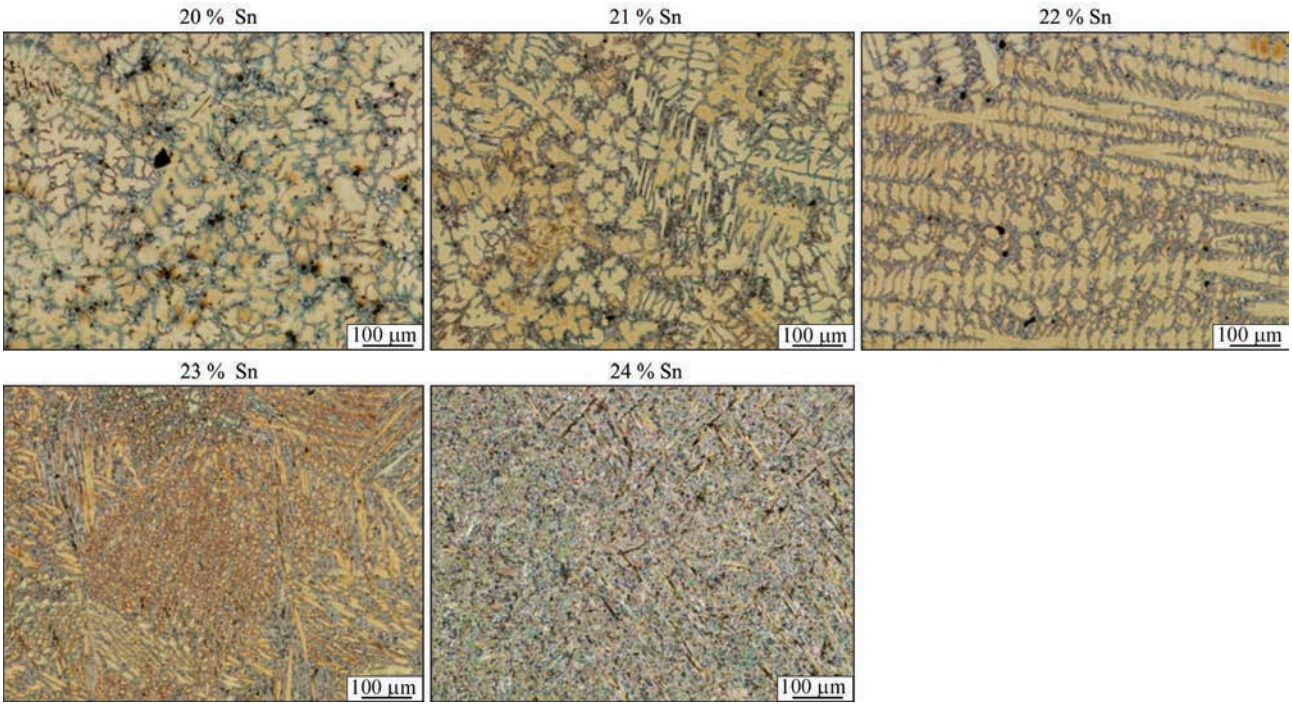

Figure 4. Microstructure of bronze with different tin content [10]

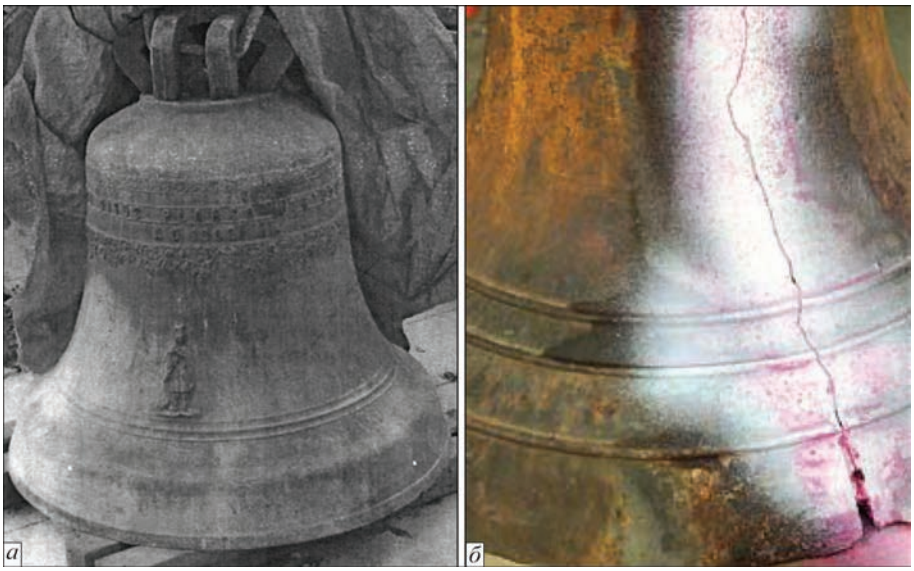

Figure 5. Appearance of a bell with the crack

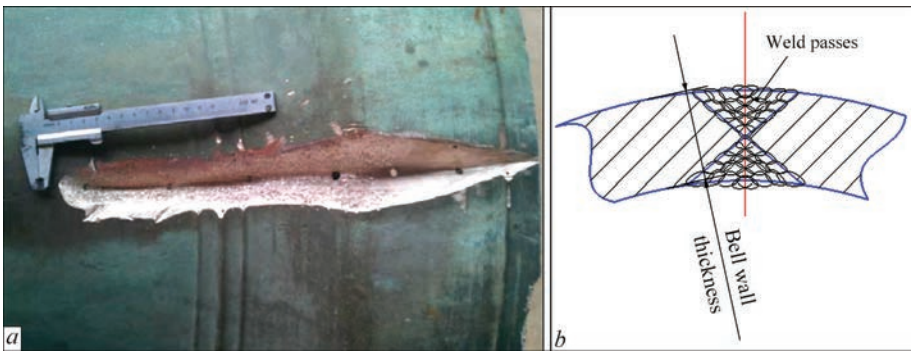

Figure 6. Appearance of a treated crack (*a*) and schematic of crack welding up (*b*)

Used as the shielding gas is argon. The welding mode parameters are as follows: I_w = 140–180 A, U_a = 10–15 V, Q_{Ar} = 10–15 l/min, d_{el} = 3.0–4.0 mm.

Of the three bells provided for repair bells K-1 and K-3 were successfully restored (Figure 8).

In bell K-2 which had the longest crack, a new crack of up to 200 mm length initiated during repair. Additional quality inspection of this bell after welding by the liquid penetrant testing revealed the presence of internal microcracks in the metal, which during welding up of a cut-out crack lead to further cracking of the bell (Figure 9, *a*). More over, pores formed in the HAZ metal (Figure 9, *b*).

Therefore, during assessment of the bell reparability a comprehensive diagnostics of its quality is required. Quality control of the restored bells and evaluation of their acoustic properties (character and

Table 2. Main overall dimensions of the bells

Bell	Height *H*, mm	Diameter *D*, mm	Crack length *l*, mm
K-1	250	300	90
K-2	400	465	230
K-3	490	580	160

Table 3. Chemical composition of the bronze

Bell	Sn, %	Zn, %	Pb, %	Cu, %
K-1	15.6–16.2	–	< 0.5	Bal.
K-2	17.0–17.8	1.3	< 1.0	
K-3	20.4–21.3	< 1.0	–	

Figure 7. Appearance of the weld

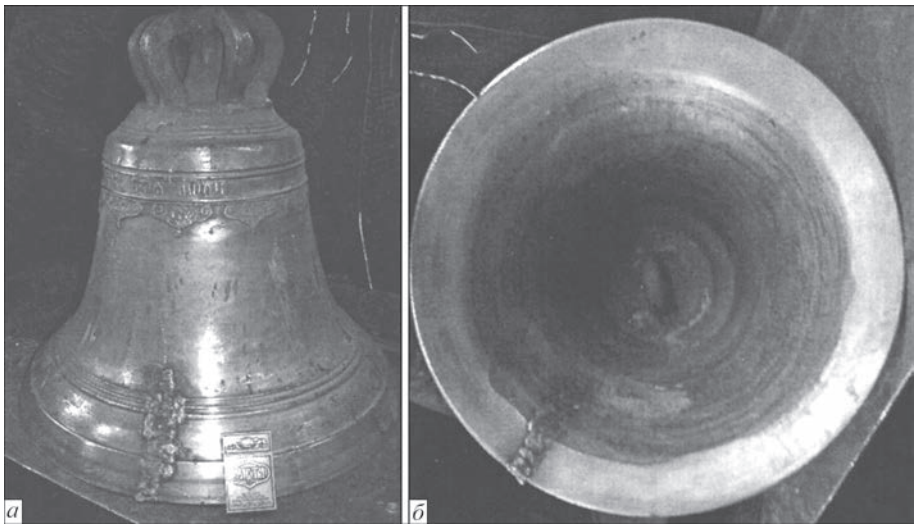

Figure 8. Restored bell K-3 from the outside (*a*) and the inside (*b*)

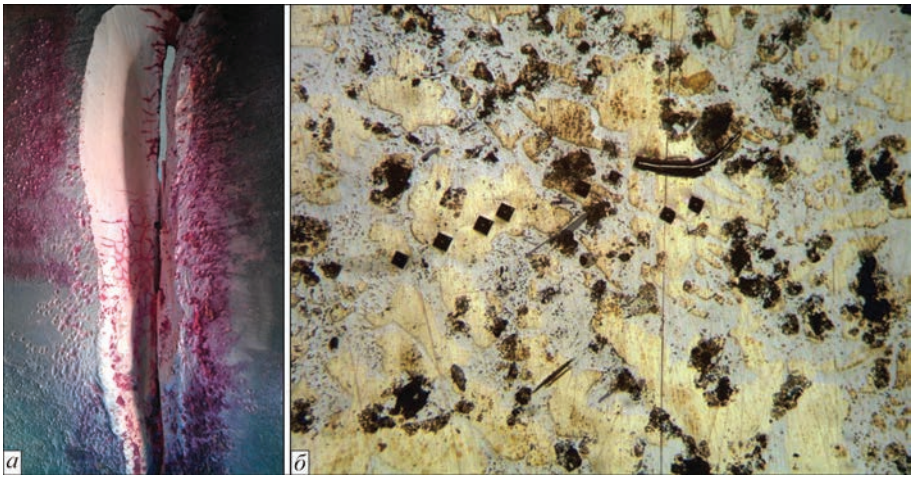

Figure 9. Defects in the HAZ: microcracks (*a*), pores (dark areas of an irregular shape) (*b*)

Figure 10. Statue of Bathing Venus (National Arboretum "Sofiivka", Uman, Ukraine)

melodiousness of the bell's sound) confirmed the possibility and expediency of repairing the church bells by the developed technologies and application of special metal-cored wires.

RESTORATION OF THE BRONZE BOWL OF "SOFIIVKA" ARBORETUM

The management of the National Arboretum "Sofiivka" (Uman) turned to PWI with the request to render technical assistance in restoration of a rare piece of art — the 19th century bronze bowl. This bowl was installed near the statue of Bathing Venus (Figure 10), was filled with spring water, which then by a granite underwater channel flowed to the lower pond. The bowl handles were decoratively made in the form of snakes [16].

"Scrap metal hunters" tore the bowl off its pedestal, and cut up the handles into 14 parts. Several "snakes" parts could not be found (Figure 11).

One of the conditions for repair was the need to achieve a decorative colour of the weld metal close to that of the bowl. In keeping with the data of mass-spectral analysis, the bowl was made from cast bronze of CuSnZnPb type. The most rational for its

Figure 11. Parts of the bronze bowl

Figure 12. Bronze bowl after restoration (*a*) and 5 years after its installation in the National Arboretum "Sofiivka" (*b*)

repair, similar to bell repair, is the use of TIG process with filler material of the type of metal-cored wire of the respective composition.

In addition to welding the damaged parts, the snake fragments which could not be found, were produced. In addition, it was necessary to make a special manual tool to produce "scales" on the surface of welded-in "snake" parts and the welds.

Figure 12 shows a photo of the restored bowl, which returned to its historical place to "Sofiivka" Arboretum.

WELDING OF MONUMENT FRAGMENTS

In the production of castings such as monuments, busts and other large-sized sculptures there arises the need to join their individual fragments. Also urgent is the problem of welding up the casting defects, forming during the product manufacturing. Modern MIG/MAG, TIG, as well as MMA welding technologies are successfully used to perform such work. Under the conditions of individual production — sculptor's workshop, mounting

Figure 13. Monument to V.I.Tolubinskyi with a broken off arm (*a*) and after coated electrode welding (*b*)

site, etc. — the MMA process, not requiring any special equipment, is the most rational. Such is the case, for instance, of repair of the monument to V.I. Tolubinskyi, academician of the AS of Ukr.SSR (Figure 13), from which the arm (in two places) and the scroll were broken off during a fall from the pedestal.

Taking into account the chemical composition of the material from which this monument was made, and PWI achievements on development of copper-based coated electrodes [17–19], a test batch of electrodes was made. Performance of welding operations on repair of this product confirmed the high quality of the weld and coincidence of the weld colour with that of the base metal, which is important in such cases.

CONCLUSIONS

1. The chemical composition and structural features of damaged works of art from copper alloys were studied. It was found that the chemical composition of the sculptures, particularly those, which were produced more than a century ago, does not always correspond to the established regulatory documents of today, leading to the need for an individual approach to development of welding consumables during sculpture repair.

2. Special metal-cored wires and coated electrodes were developed, which ensure both high values of welded joint strength, and their required decorative properties.

3. Conducted research and experimental work on restoration of cast products from copper alloys, including bell bronzes, and derived positive results allow a significant expansion of the application of repair-welding technologies in the practice of restoration of such products.

REFERENCES

1. Liakyshev, N.P. (editor) (1997) *State diagrams of binary metallic systems*: Referbook. Moscow, Mashinostroenie [in Russian].
2. Abramovich, V.R., Demiantsevich, V.P., Efimov, L.A. (1988) *Fusion welding of copper and copper-based alloys*. Leningrad, Mashinostroenie [in Russian].
3. Suchkov, D.Y. (1967) *Copper and its alloys.* Moscow, Metallurgiya [in Russian].
4. Lebedev, K.P., Raines, L.S., Shemtov, H.S. et al. (1973) *Cast bronzes*. Leningrad, Mashsnostroenie [in Russian].
5. Le Jeune Road, N.W. (1997) *Welding copper and copper alloys*. Miami, AWS.
6. Smiriagin, A.P., Smiriagina, H.A., Belova, A.B. (1974) *Industrial non-ferrous metals and alloys*. Moscow, Metallurgiya [in Russian].
7. Savega, V.S., Hrichikov, V.E., Matveeva, M.O. (2014) *Art and jewelry casting*: Tutorial. Dnipro, NMetAU.
8. *Royal Bells Workshop. Przemysl*. https://dzvony.net/home
9. *Varieties of church bells in the Orthodox tradition. Poltava*. http://dzvonar.com.ua
10. Nadolski, M. (2017) The evaluation of mechanical properties of high-tin bronzes. *Archives of Foundry Eng.,* 17(**1**), 127–130. DOI: https://doi.org/10.1515/afe-2017-0023
11. Audy, J., Audy, K. (2009) Analysis of bell materials: Tin bronzes. *China Foundry*, 58(**1**), 77–81. DOI: https://doi.org/1672-6421(2008)03-0199-06
12. Ernesto, Ponce L., José de la Vega (2014) Restoration of ancient bronze bells. Pt I: Powder metallurgy. *Revista Chilena de Ingeniería*, 22(**4**), 460–468. DOI: http://dx.doi.org/10.4067/S0718-33052014000400002
13. Bartocha, D., Baron, C. (2021) Repair of a cracked historic Maryan Bell by gas welding. *Materials*, 14(**10**), 2504. DOI: https://doi.org/10.3390/ma14102504
14. Ernesto Ponce, L. (2015) Restoration of ancient bronze bells. Pt II: Welding. *Revista Chilena de Ingeniería*, 23(**1**), 30–37. DOI: http://dx.doi.org/10.4067/S0718-33052015000100004
15. (2017) *Friends of the Truro Meeting House. Revere bell restoration*. https://www.truromeetinghousefriends.com/wp-content/uploads/2016/06/2016-Spring-Newsletter-05142016.pdf
16. Kosenko, I.S., Pylypiuk, V.V. (2016) *Sofiivka. Arboretum*: Photoalbum. Kyiv, Palyvoda A.V. [in Ukrainian].
17. Iliushenko, V.M., Maidanchuk, T.B., Anoshin, V.O., Skoryna, M.V. (2014) *Composition of electrode coating for welding and surfacing tin bronzes.* Pat. UA 106954, Fill. 18.12.2013, Publ. 27.10.2014 [in Ukrainian].
18. Majdanchuk, T.B., Skorina, N.V. (2014) Improvement of adaptability to fabrication and welding properties of electrodes for tin bronze welding and surfacing. *The Paton Weldong J*., **6–7**, 172–176. DOI: https:/doi.org/10.15407/tpwj2014.06.37
19. Iliushenko, V.M., Lukianchenko, Ye.P. (2013) *Welding and surfacing of copper and copper alloys.* Kyiv, International Association "Welding" [in Russian].

ORCID

T.B. Maydanchuk: 0000-0002-2826-8514,
A.M. Bondarenko: 0000-0003-0506-4444,
V.M. Ilyushenko: 0000-0002-9047-8512,
E.P. Lukianchenko: 0000-0001-7678-5965

CONFLICT OF INTEREST

The Authors declare no conflict of interest

CORRESPONDING AUTHOR

T.B. Maydanchuk
E.O. Paton Electric Welding Institute of the NASU
11 Kazymyr Malevych Str., 03150, Kyiv, Ukraine.
E-mail: pwi_37@ukr.net

SUGGESTED CITATION

T.B. Maydanchuk, A.M. Bondarenko,
V.M. Ilyushenko, V.M. Slyushenko,
E.P. Lukianchenko (2025) Restoration of bells
and art products made of copper alloys.
The Paton Welding J., **10**, 24–30.
DOI: https://doi.org/10.37434/tpwj2025.10.04

JOURNAL HOME PAGE

https://patonpublishinghouse.com/eng/journals/tpwj

Received: 24.04.2025
Received in revised form: 16.06.2025
Accepted: 29.09.2025

DOI: https://doi.org/10.37434/tpwj2025.10.05

THERMODYNAMIC ANALYSIS OF PREPARATION OF TWO KEY REFRACTORY BORON COMPOUNDS

K. Ukleba[1], Z. Mirijanashvili[1], O. Tsagareishvili[1], L. Chkhartishvili[1,2]

[1]F. Tavadze Metallurgy and Materials Science Institute
8b Elizbar Mindeli Str., 0186, Tbilisi, Georgia
[2]Georgian Technical University
77 Merab Kostava Ave., 0160, Tbilisi, Georgia

ABSTRACT

Thermodynamic calculations are performed to determine the optimal conditions for carrying out two chemical reactions to obtain boron carbide and titanium diboride, important refractory boron compounds, in combination with aluminum oxide. The accompanying phase transformations at a fixed pressure are established as a function of temperature.

KEYWORDS: thermodynamic analysis, temperature, enthalpy, Gibbs free energy, chemical reaction, boron carbide, titanium diboride, aluminum oxide

INTRODUCTION

Boron compounds have many promising industrial applications [1]. Many of them are materials based on boron carbide B_4C [2–4]. Perhaps the second most common boron compound is titanium diboride TiB_2, which is often found in composites containing boron carbide as well [5–8]. In this paper, we consider two examples of chemical reactions of the formation of B_4C and TiB_2, respectively, together with aluminum oxide Al_2O_3, an important component of boron-containing composite ceramics.

It should be emphasized that the present introduction of this short communication does not aim to exhaust the vast number of reports on composites containing boron carbide and titanium diboride. The above are only citations of recent works by authors on boron containing composite materials, which led them to the problem considered here.

In general, thermodynamic calculations allow us to determine the conditions for various chemical reactions in a given system of reagents and the nature of the accompanying phase transformations depending on temperature. In this paper, such an analysis is carried out for the processes of obtaining two important refractory boron compounds – boron carbide and titanium diboride – in combination with aluminum oxide.

APPROACH

We used a standard approach in which the energy and spontaneity of chemical reactions are described by thermodynamic parameters. The key parameters are enthalpy H, entropy S, and Gibbs free energy G, which are responsible for heat release, disorder, and overall spontaneity, respectively. They help predict whether a reaction will occur spontaneously and under what conditions.

Enthalpy represents the heat content of a physical system at constant pressure. A negative enthalpy change ΔH indicates an exothermic reaction (heat is released), while a positive ΔH indicates an endothermic reaction (heat is absorbed). Entropy measures the disorder or randomness of a system. A positive entropy change ΔS indicates an increase in disorder, while a negative ΔS indicates a decrease. Gibbs free energy combines enthalpy and entropy to determine the overall spontaneity of a reaction. A negative Gibbs free energy change ΔG indicates a spontaneous reaction, while a positive ΔG indicates a non-spontaneous reaction. The Gibbs free energy equation $\Delta G = \Delta H - T\Delta S$ shows the interplay between enthalpy, entropy, and temperature T in determining spontaneity. A reaction is more likely to be spontaneous at lower temperatures if it is exothermic (negative ΔH) and increases in disorder (positive ΔS).

Understanding these parameters is crucial for:

- Predicting reaction feasibility or determining whether a reaction will occur under given conditions.
- Optimizing reaction conditions or adjusting temperature, pressure, and concentrations.
- Designing chemical processes via developing efficient and sustainable chemical reactions.

As 3 parameters ΔH, ΔS, and ΔG at fixed temperature T are related with each other, only 2 of them are independent. Following a standard approach, we chose ΔH and ΔG to characterize chemical reactions under the study. In particular, a general scheme of possible reactions was developed.

Thermodynamic calculations were carried out using the complex program ASTRA-4 in the temperature range of 800–6000 K at a pressure of 1 atm.

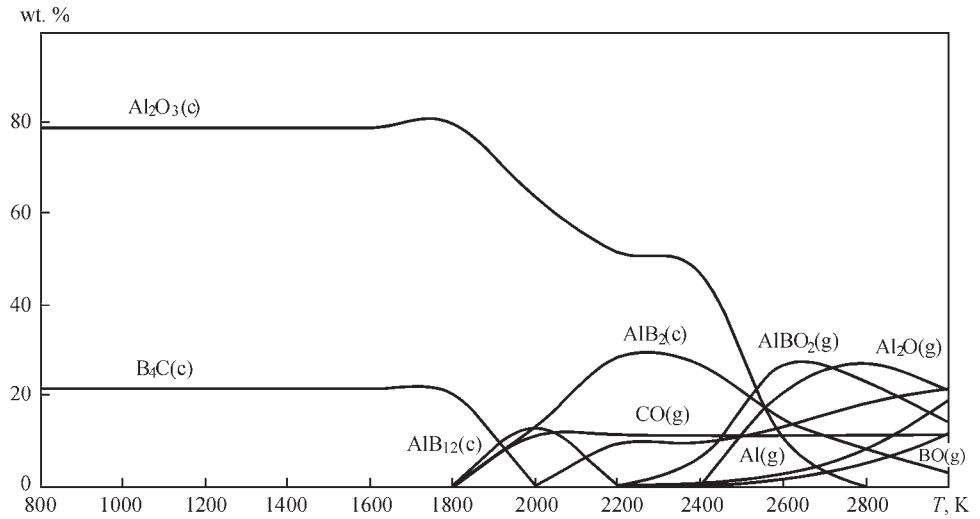

Figure 1. Change in content of gaseous (g) and condensed (c) phases formed during the process of obtaining boron carbide in temperature range of 800–3000 K

RESULTS OF THERMODYNAMIC CALCULATIONS AND THEIR DISCUSSION

The processes of obtaining boron carbide B_4C and titanium diboride TiB_2 selected for investigation are based on the reactions

$$2B_2O_3 + 4Al + C = B_4C + 2Al_2O_3$$

and

$$4TiO_2 + 8B + 4Al + C = 4TiB_2 + 2Al_2O_3 + CO_2,$$

respectively. Below, the results of the thermodynamic analysis performed are presented in the form of diagrams (Figures 1 and 2) and Tables 1, 2, 3 and 4.

The process diagram for obtaining B_4C (Figure 1) shows that the reaction products are mostly released in condensed form in the temperature range of 800–2800 K, while above 1800 K, the gas phases are mainly obtained. The optimal temperature range for synthesizing the target products, i.e. boron carbide and aluminum oxide, is 800–1600 K.

For this case, we calculated the reaction enthalpy ΔH (Table 1) and Gibbs free energy ΔG (Table 4) at some different temperatures, which allowed us to determine the possibility of its conduction and the nature of the process.

From this it can be seen that, on the one hand, the process is exothermic ($\Delta H < 0$) in the entire temperature range of the study: 800–3000 K. On the other hand, in the range 800–2400 K, $\Delta G < 0$ and, therefore, the reaction proceeds, but above 2400 K, when $\Delta G > 0$, it ceases.

The diagram of Figure 2 shows that the main products of the reaction to produce TiB_2 are mostly released in condensed form in the temperature range of 800–4000 K, while above 2400 K, gaseous phases are predominantly obtained. The optimal temperature range for synthesizing the target phases (in this case, titanium diboride and aluminum oxide) can be considered to be 1200–2000 K.

Table 1. Calculated enthalpy of reaction to produce boron carbide

Temperature T, K	Enthalpy ΔH, kcal
800	–201
1000	–203
1200	–211
1400	–230
1600	–267
1800	–332
2000	–437
2200	–594
2400	–821
2600	–1135
2800	–1556
3000	–2104

Table 2. Calculated Gibbs free energy of reaction to produce boron carbide

Temperature T, K	Gibbs free energy ΔG, kcal
800	–183
1000	–178
1200	–173
1400	–165
1600	–154
1800	–136
2000	–109
2200	–69
2400	–12
2600	+68
2800	+176
3000	+317

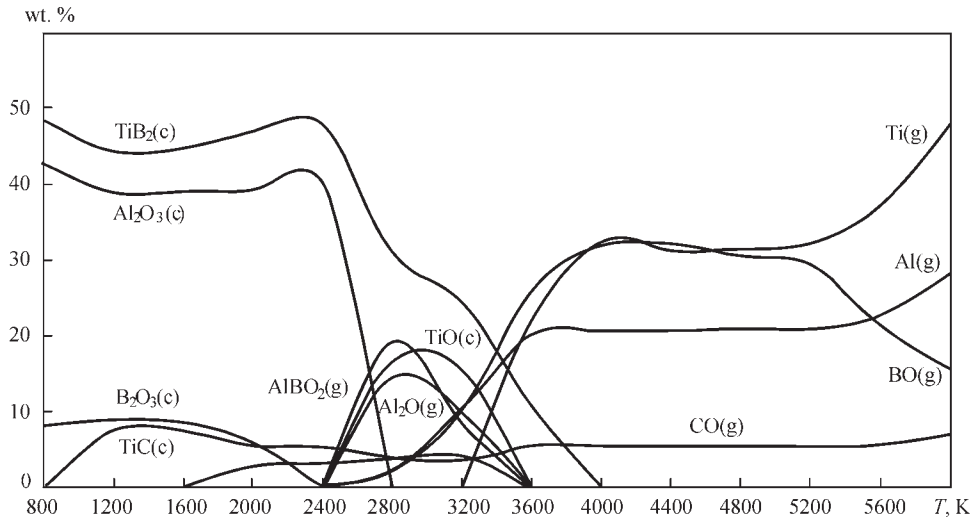

Figure 2. Change in gaseous (g) and condensed (c) phases formed during the process of obtaining titanium diboride in temperature range of 800–6000 K

Table 3. Calculated enthalpy of reaction to produce titanium diboride

Temperature T, K	Enthalpy ΔH, kcal
800	–264
1200	–269
1600	–281
2000	–307
2400	–353
2800	–417
3200	–489
3600	–541
4000	–514
4400	–278
4800	+438
5200	+2119
5600	+5567
6000	+11992

Table 4. Calculated Gibbs free energy of reaction to produce titanium diboride

Temperature T, K	Gibbs free energy ΔG, kcal
800	–269
1200	–271
1600	–271
2000	–265
2400	–253
2800	–232
3200	–200
3600	–161
4000	–119
4400	–88
4800	–97
5200	–201
5600	–494
6000	–1129

The values obtained by calculating the ΔH (Table 3) and ΔG (Table 4) parameters of this reaction determine the possibility of its conduction at different temperatures and the nature of its course.

As can be seen from the results obtained, the process is exothermic in the temperature range of 800–4400 K, where $\Delta H < 0$ (Table 3). The reaction itself proceeds completely in the studied temperature range, since always $\Delta G < 0$ (Table 4).

CONCLUSIONS

The first of above-considered high-temperature reactions, $2B_2O_3 + 4Al + C = 2Al_2O_3 + B_4C$, is often carried out using SHS (Self-propagating High-temperature Synthesis) to efficiently produce boron carbide and its composites. It is a thermite-type metallothermic reduction where boron oxide B_2O_3 is reduced by aluminum Al with carbon C, as a carbide producing reactant, to form boron carbide B_4C and aluminum oxide Al_2O_3. First, aluminum acts as a strong reducing agent for boron oxide, removing oxygen. The carbon then reacts with the boron to form the desired boron carbide product.

The methods of synthesis of boron carbide powders were surveyed in the mini-review [9]. Based on the morphological peculiarities of the products obtained, in particular, by metal- and carbothermic reductions, it was found [10] that the chemical oven method can readily heat reactants used in combustion synthesis of B_4C powder (as well as forming sintered $TiC–Al_2O_3$ as a precursor for composite material). Finer powder of B_4C was formed under higher compacting pressure on green compact. In addition, since the extent of expansion of reactant compact increased as the theoretical density of the reactant compact increased, a higher

packing compact can easily be crushed to powders after combustion reaction.

Composite of B_4C–Al_2O_3 was prepared [11] by SHS from ball-milled powder mixture B_2O_3/Al/C with components ratio corresponding to the reaction: $2B_2O_3 + 4Al + C = B_4C + 2Al_2O_3$. B_4C–Al_2O_3 composite was also produced [12] by aluminothermic reduction in Al/B_2O_3/C system using microwave heating of ball-milled powder.

Using B_4C, Al, and C powders as the raw materials, phase pure $Al_8B_4C_7$ nanoparticles were obtained [13] after firing via a molten-salt-mediated route. The synthesis mechanism can be described as follows. In a eutectic liquid medium, Al partially dissolved and diffused onto the surfaces of C and B_4C to form Al_4C_3 and Al_3BC–AlB_2, respectively. B from the decomposition of AlB_2 also slightly dissolved in the salt, diffused onto the surface of Al_4C_3 formed earlier, and reacted with it to form $Al_8B_4C_7$. On the other hand, the Al_3BC formed earlier also decomposed to give Al, B, and Al_4C_3. The latter two would similarly react to form $Al_8B_4C_7$. Compared to the conventional techniques, the synthesis temperature in this case was significantly (about 500 K) lower.

Another considered high-temperature reaction, $4TiO_2 + 4Al + 8B + C = 4TiB_2 + 2Al_2O_3 + CO_2$, is used to produce titanium diboride and its composites.

In the dissertation [14], an exothermic reaction was designed to synthesize Al_2O_3 and TiB_2 from TiO_2 particles and elemental B in an Al melt, and the mechanism of such boro- and aluminothermic reduction of titanium oxide together with *in situ* synthesis of micro- and nanoparticles via solidification processing was investigated. Microstructural examination in combination with theoretical analysis indicated that the formation of TiB_2 and Al_2O_3 proceeds through several complex non-equilibrium reactions. According to the multi-stage reaction model proposed to describe the process by which the TiO_2 surface reduces to form Al_2O_3 and TiB_2, nanosized TiO_2 powder was found to promote the formation of smaller size reinforcing phases. A solidification route was designed to fabricate *in-situ* aluminum composites reinforced with submicron Al_2O_3 and TiB_2 particulates. In the dissertation [17], the chapter devoted to the synthesis of TiB_2 to be alloyed with Al contains a thermal analysis of the corresponding reaction mixture.

In-situ composite coatings of TiC–Al_2O_3, as well as TiB_2–TiC–Al_2O, were applied [15] on the surface of stainless steel by using combining, welding, and self-combustion synthesis. In all heat inputs, cubic titanium carbide particles formed heterogeneously on Al_2O_3 particles or spontaneously in the austenitic matrix of stainless steel. The reinforcing of TiC and TiB_2 particles formation in both $3TiO_2$–4Al–3C and $3TiO_2$–4Al–B_4C layers led to an increase in surface hardness and wear resistance versus the substrate. The reaction process in an Al–TiO_2–C system was studied in [16]. TiC and Al_2O_3 were finally formed in the Al matrix. $TiAl_3$ and Al_4C_3 were found to be transitional phases during the *in situ* reaction process, which involves two steps: (1) $3TiO_2 + 13Al = 3TiAl_3 + 2Al_2O_3$ and $4Al + 3C = Al_4C_3$ and (2) $3TiAl_3 + Al_4C_3 = 3TiC + 13Al$. Quasi-adiabatic combustion synthesis of optimized $3TiO_2 + 4Al + (3 + x)C$ mixture in the presence of oxygen was carried out [17] to produce TiC–Al_2O_3 composite and the influence of Al_2O_3 diluent in combusted reactant mixture $6TiO_2 + 8Al + 7C + 2yAl_2O_3$ was investigated. Thermodynamics studies showed that self-sustaining mode of combustion wave propagation can occur for large amounts of diluents ($y = 2.5$). Adding Al_2O_3 diluent increased density that resulted in better thermal conductivity and reduced combustion temperature and rate of reaction. The effect of TiO_2 on some of Al_2O_3-containing systems was considered as well [18].

Summarizing these literature data, we can conclude that the study of chemical reactions of aluminothermic reduction to obtain high-temperature boron compounds is an important materials science problem. In this paper, the thermodynamic analysis allowed us to determine the possibilities and conditions for the conduction of specific reactions, $2B_2O_3 + 4Al + C = B_4C + 2Al_2O_3$ and $4TiO_2 + 8B + 4Al + C = 4TiB_2 + 2Al_2O_3 + CO_2$, for the production of two boron compounds of particularly high practical interest — titanium diboride and boron carbide, and also determine the expected phase composition of their products, which allows to optimally select the compositions of the reagents.

REFERENCES

1. Chkhartishvili, L., Mikeladze, A., Tsagareishvili, O. et al. (2018) Boron-containing nanocrystalline ceramic and metal–ceramic materials. In: *Handbook of Nanomaterials for Industrial Applications*. Ed. by Ch.M. Hussain. Amsterdam, Elsevier, 13–35.
2. Chkhartishvili, L., Tsagareishvili, O., Mikeladze, A. et al. (2021) Highly stable boron carbide based nanocomposites. In: *Handbook of Nanomaterials and Nanocomposites for Energy and Environmental Applications*. Eds by O.V. Kharissova, L.M.T. Martinez, B.I. Kharisov. Cham, Springer Nature, 327–351.
3. Chkhartishvili, L., Antashvili, L., Dalakishvili, L. et al. (2021) On modeling of synthesis process of boron carbide based nanocomposites. *Condensed Matter*, 6(**1**), 3(1–13).
4. Chkhartishvili, L., Mikeladze, A., Tsagareishvili, O. et al. (2023) Advanced boron carbide matrix nanocomposites obtained from liquid-charge: Focused review. *Condensed Matter*, 8(**2**), 37 (1–54).
5. Mikeladze, A., Tsagareishvili, O., Chkhartishvili, L. et al. (2019) Production of titanium-containing metal-ceramic com-

posites based on boron carbide in the nanocrystalline state. *Adv. Appl. Ceram.*, 118(**4**), 196–208.
6. Chkhartishvili, L., Mikeladze, A., Chedia, R. et al. (2020) Synthesizing fine-grained powders of complex compositions B_4C–TiB_2–WC–Co. *Solid State Sci.*, **108**, 106439 (1–8).
7. Chkhartishvili, L., Mikeladze, A., Tsagareishvili, O. et al. (2023) Effect of cobalt additive on phases formation in boron carbide matrix composites B_4C–(Ti,Zr)B_2–W_2B_5. *Solid State Sci.*, **145**, 107339 (1–11).
8. Tsagareishvili, O., Mikeladze, A., Chedia, R. et al. (2024) Obtaining of WC–Co- and WC–TiC–Co-based ultradispersive alloys modified with B_4C–TiB_2 quasieutetic. *Recent Prog. Mater.*, 6(**3**), 21 (1–50).
9. Radev, D.D., Ampaw, E. (2015) Classical and contemporary synthesis methods of boron carbide powders. *Comp. Rend. Acad. Bulgare Sci.*, 68(**8**), 945–946.
10. Lee, J.H., Won, C.W., Joo, S.M. et al. (2000) Preparation of B_4C powder from B_2O_3 oxide by SHS process. *J. Mater. Sci. Lett.*, **19**, 951–954.
11. Han, K.R., Kang, D.-I., Kim, Ch.-S. (2003) Preparation of B_4C–Al_2O_3 composite powder by self-propagation high-temperature synthesis (SHS) process under high pressure. *J. Korean Ceram. Soc.*, 40(**1**), 18–23.
12. Shaker, E., Sakari, M., Jalaby, M., Bafghi, M.Sh. (2015) Microwave synthesis of B_4C–Al_2O_3 composite in a mechanically activated Al/B_2O_3/C powder mixture. *Iranian J. Mater. Sci. Eng.*, 12(**4**), 89–99.
13. Liu, Ch. (2019) *Low temperature synthesis and characterization of novel complex carbide- and boride-based materials:* PhD Dissertation. Exeter, Univ. Exeter (ProQuest: 27822589).
14. Moghdam, A.D. (2016) *In-situ synthesis of aluminum-titanium diboride metal matrix hybrid nanocomposite:* PhD Dissertation. Milwaukee, Univ. Wisconsin–Milwaukee, 1137: https://dc.uwm.edu/etd/1137
15. Bahramizadeh, E., Nourouzi, S., Jamshidi Aval, H. (2019) *In-situ* fabrication of TiC–Al_2O_3 and TiB_2–TiC–Al_2O_3 composite coatings on 304 stainless steel surface using GTAW process. *Kovove Mater.*, **57**, 177–188.
16. Wang, Zh., Liu, X., Zhang, J., Bian, X. (2004) Reaction mechanism in an Al–TiO_2–C system for producing *in situ* Al/(TiC+Al_2O_3) composite. *J. Mater. Sci.*, **39**, 667–669.
17. Rahbari, G.R., Saw, L.H., Hamdi, M., Yahya, R. (2009) Combustion synthesis of TiO_2–Al–C/Al_2O_3 mixture in the presence of oxygen. *J. Phys. Conf. Ser.*, **152**, 012055.
18. Velinova, R., Todorova, S., Kovacheva, D. et al. (2023) Effect of TiO_2 on Pd/La_2O_3–CeO_2–Al_2O_3 systems during catalytic oxidation of methane in the presence of H_2O and SO_2. *Materials*, **16**, 6784.

ORCID
L. Chkhartishvili: 0000-0003-3926-4524

CONFLICT OF INTEREST
The Authors declare no conflict of interest

CORRESPONDING AUTHOR
L. Chkhartishvili
Georgian Technical University
77 Merab Kostava Ave., 0160, Tbilisi, Georgia
E-mail: levanchkhartishvili@gtu.ge

SUGGESTED CITATION
K. Ukleba, Z. Mirijanashvili, O. Tsagareishvili, L. Chkhartishvili (2025) Thermodynamic analysis of preparation of two key refractory boron compounds. *The Paton Welding J.*, **10**, 31–35.
DOI: https://doi.org/10.37434/tpwj2025.10.05

JOURNAL HOME PAGE
https://patonpublishinghouse.com/eng/journals/tpwj

Received: 18.08.2025
Received in revised form: 23.09.2025
Accepted: 24.10.2025

DOI: https://doi.org/10.37434/tpwj2025.10.06

METHODOLOGY OF USING STANDARD SPECIMENS WITH DEFECTS FOR EDDY CURRENT INSPECTION: CLASSIFICATION, TYPICAL EXAMPLES, SIGNALS RESEARCH AND STATISTICAL METHOD FOR PARAMETERS ASSESSMENT

V.M. Uchanin

G.V. Karpenko Physico-Mechanical Institute of the NASU
5 Naukova Str., 79060, Lviv, Ukraine

ABSTRACT

The work was aimed at development of a methodology for using reference standards (RS) with defects to ensure high reliability and repeatability of eddy current flaw detection results. A classification of reference standards with defects is proposed and relevant examples are given to confirm the validity of the proposed classification. As an example, designs of composite multi-valued reference standards are presented for simulating surface and subsurface defects in cylindrical and flat objects under eddy current testing. New designs of composite reference standards are shown that simulate defects with different depths of occurrence. A corresponding set of RSs is presented that simulate a subsurface crack of the same size with 4 values of its depth of occurrence, and the corresponding double-differentiation eddy current probe signals are experimentally investigated. A proposed method for manufacturing reference standards for simulating inclined cracks is presented. A number of studies are analyzed that consider possible reasons for the difference between eddy current probe signals from a natural crack and artificial defects. By means of calculations using the method of volume integral equations, it is shown that the main reason for the difference between eddy current probe signals from natural fatigue defects and artificial defects is their width (opening). The influence of the crack length on the features of the parametric type eddy current probe signal is considered, which must be taken into account when choosing the length of the cracks of the reference standards to ensure the sensitivity threshold and reproducibility of the inspection results. A statistically based method for reliable estimation of the parameters of the reference standards with natural defects is presented, which has been successfully used to evaluate reference standards with fatigue cracks in tubular specimens.

KEYWORDS: reference standard, classification, eddy current method, non-destructive testing, eddy current probe, artificial defect, defect parameters

INTRODUCTION AND STATE OF THE PROBLEM

Metrological support methods and means have an important role in achievement of a high validity and repeatability of the results of eddy current flaw detection [1–3], with two approaches being possible here. Most often used for defect simulation are reference standards (RS) with artificial defects (AD) with the specified geometrical parameters, among which the most often normalized is the sensitivity threshold, i.e. the minimal AD depth, which should be revealed by the eddy current flaw detector (ECFD). Parameters of AD in RS should correspond to the requirements of technical documentation as to ECFD sensitivity threshold and conditions of its determination (distance from the eddy current probe (ECP) to the tested object (TO) surface, electrical-physical characteristics (specific electric conductivity and magnetic permeability) of TO material, TO thickness, etc). Scanning the TO surface using ECP, a metrologist or flaw-detection operator can assess the ECFD correspondence to the normalized characteristics as to sensitivity to the defects. Another rare approach is based on the use of electronic defect simulators, the simulation windings of which generate an electromagnetic field or signal, identical to those generated by eddy currents in a TO with a defect.

The problems of metrological support of ECFD using RS are not given due attention. In publications and standards on nondestructive testing (NDT) a great variety of terms could encountered for a long time: “test specimen”, “control specimen’, “standard specimen”, “standard”, “calibration standard”, “standard calibration specimen”, “simulator”, etc., which confirms an absence of common approaches. In English-language publications different terms are also used, in particular “reference standard” [4], or “reference block” [5]. And only in the last decades the term “reference standard” became the most commonly used for flaw detection RS. In keeping with the generally accepted metrological terminology [6], “a reference standard of the composition or properties of a substance (material) is a measurement means in the form of a specified amount of substance or material, designed for reproduction and storage of dimensions of quantities, characterizing the composition or properties of this substance (material), the values of which were determined as a result of me-

trological certification, which is used to transfer the unit size during verification, calibration, graduation of measuring instruments, certification of measurement procedures, and has been approved as RS in accordance with the established procedure". It is obvious that the above term does not take into account the specifics of flaw detection by NDT methods. However, there also exists a metrological term "measure, as a measurement instrument, which implements reproduction and (or) preservation of a physical quantity of the specified value" [6]. This term is more suitable for means for reproducing the physical quantity, used as the base for the NDT method than for specimens with AD. Important examples can be specimens for magnetic structural analysis instruments based on determination of the parameters of the magnetic hysteresis loop [7] or specimens of specific electric conductivity (SEC) for eddy current structuroscopes [8]. Unfortunately, the use of the term "measure"' is not an established practice in NDT metrology yet. This is confirmed by a discussion between the authors of the invention "Measure of the coercive force for metrological support of coercimeters with attached sensors" (authors are V.M. Uchanin, V.G. Rybachuk, S.M. Minakov, R.M. Solomakha) and experts of the State Patent Examination Office, who refused to issue a patent with such a title at first. However, the authors managed to defend their position, and today the patent is pending.

The above definition of the "reference standard" is very general and it does not take into account the features of flaw detection NDT, which is important to ensure a high reliability and repeatability of the obtained results. Therefore, for flaw detection RS used in NDT, the following definition is formulated: "A flaw detection reference standard is a product with normalized metrological characteristics for reproducing the property of TO discontinuities to generate a signal from primary transducer of the specified NDT technique". Such a definition underlines the main requirement to flaw detection RS: to adequately reproduce the features of simulated defects and TO design features. On the other hand, RS for flaw detection is a physical model of the material discontinuity, having a regular geometric shape and adequately replacing the material discontinuity during adjustment or calibration of NDT means. This definition implies a certain contradiction, because the RS, as any model, cannot fully reflect all the properties of the real TO. The adequacy problem should be solved, taking into account the special features of the defined problem and NDT technique. In particular, the RS for NDT should take into account the physical phenomena, on which a specific NDT method is based. As an example, we can give RS for ultrasonic testing, made from materials with the respective acoustic characteristics (for instance, organic glass), neglecting the TO electrophysical characteristics, in particular, their specific electric conductivity and magnetic permeability (MP). Accordingly, the difference in the acoustic characteristics of the RS and TO material can be neglected for eddy current testing. For this method, it is important to ensure the RS electrophysical characteristics, in particular their SEC and MP, which should correspond to TO material characteristics. The simplest way to ensure the adequacy of electrophysical characteristics is to make RS from the same material as the TO. Here, the RS production technology (in particular, the surface and heat treatment) should provide the respective material structure and stability of its electrophysical characteristics in time, which is related to physical aging of the material and to wear of the surface layer. Another requirement to RS is the possibility of making AD with established parameters with the specified accuracy, which is necessary for reproducing them when manufacturing a batch of RS. Not less important is the possibility of measurement of the normalized AD parameters for their metrological evaluation.

Let us remember that a new Law of Ukraine on metrology and metrological activity came into effect since 2016 [9], which changed the meaning of many metrological terms with the purpose of their harmonization with the international metrological practice [10]. The new law introduced the concept of "legislatively regulated metrology", which covers the types of activity, which are subject to state regulation as regards measurements, units of measurement and measuring equipment (ME). Metrological operations in the enterprises are concerned with ME metrological confirmation, which is understood as a set of operations, required to guarantee that ME conforms to the metrological requirements for its intended use. At the national and international levels ME metrological confirmation envisages conducting metrological operations, namely their testing and calibration. The "testing" term corresponds to "verification", which means obtaining objective evidence that this ME corresponds to the established requirements. From 1993 till 2015 the "verification" term referred to ME, which are subject to state metrological supervision. In addition, starting from 2016 there separately exist ME in the sphere of legislatively regulated metrology and other ME, which are not covered by legislatively regulated metrology. There is an analogy with the state and departamental verification of ME, which existed up to 1993. At the same time, there is an expectation that the basic methodology of RS application in eddy current flaw detection defined below will be relevant, irrespective of the changes in the legislation of Ukraine.

This paper is an attempt to initiate the creation of the methodology of RS application in eddy current flaw detection. In particular, an RS classification with the respective examples is proposed, a range of engineering solutions is given for RS for simulation of subsurface and inclined defects, the influence of RS defect width and length on ECP signal was studied and a statistically substantiated method to determine the parameters of RS with natural defects is presented.

CLASSIFICATION OF FLAW DETECTION REFERENCE STANDARDS

To develop the methodology of RS application for metrological support of ECFD, we will consider the possible RS variants based on their classification, where the following features were used as the classification characteristics: type and origin of the defects; AD producing technology; main normalized parameters and number of normalized values; design, as well as the stage at which they are used (Figure 1).

Flaw detection reference standards can be produced using natural or artificial defects (Figure 1). It is obvious that the real conditions of defect detection are best reproduced by RS with natural defects, arising during the production cycles (melting, casting, deformation stamping, heat and chemical-thermal treatment; machining, welding) or during operation (fatigue cracks, corrosion damage of different types, etc.). The disadvantages of RS with fatigue cracks, in particular, is the problem of introducing cracks with specified geometrical parameters with guaranteed accuracy. The possibility of determination of the fatigue crack parameters during metrological evaluation is also limited, because of their small opening (width). Accurate characteristics of RS with natural defects can be determined only after their fracture. That is why in practice RS with AD of a simple shape are traditionally used for testing and tuning of the NDT means [11–13]. An advantage of such RS is the simplicity of their production and metrological evaluation, which is performed by measurement of AD normalized parameters by the methods of linear dimensions measurement.

Irrespective of their origin, the defects are usually divided into elongated (linear) and local (bulk). A defect, for which the ratio $l_{CR} >> a >> c$ is valid, where l_{CR} is the crack length, a is its depth and c is its width, is usually called a crack. These parameters are close for local defects (for instance, pores). Elongated cracklike AD are predominantly simulated by slots (cuts), made by electric spark method or a thin mill. The thinnest slots, which reproduce a natural crack better, are made by electric spark method, which creates defects of up to 0.1 mm width (opening). Pro-

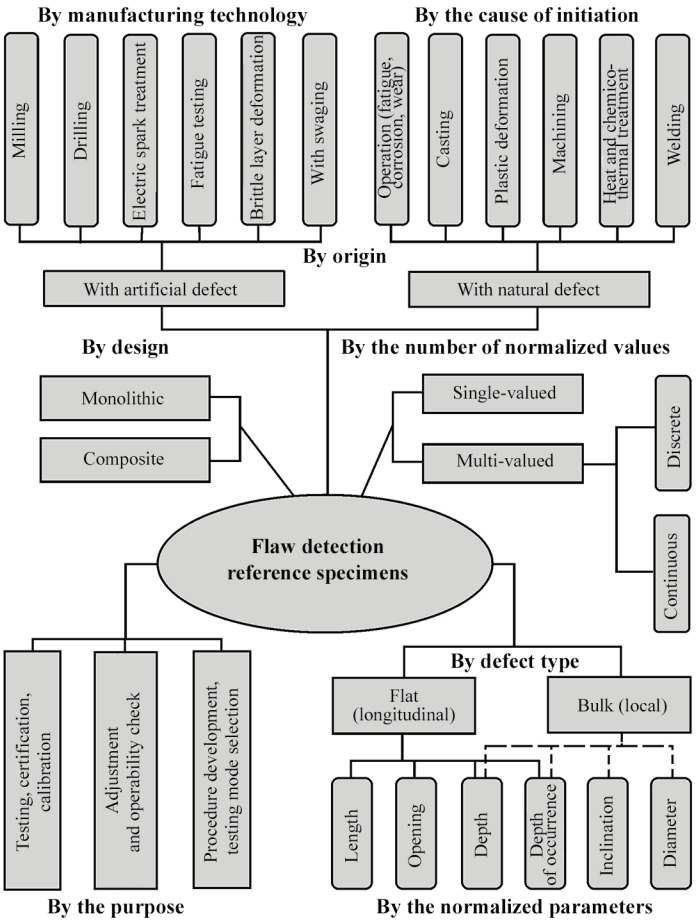

Figure 1. Classification of reference standards in flaw detection

ducing AD by milling is simpler, but it does not allow making AD of less than 0.2 mm width. Opening of such an AD is reduced by swaging, for which the material ductile properties are enhanced by heating [11]. Local volume defects of the type of a pore or corrosion pit are usually simulated by drilling with a flat bottom [14, 15].

A disadvantage of RS with AD is the fact that by their properties, and, what is particularly important, by the ability to form the respective ECP signal they differ from RS with natural defects (in particular, fatigue and corrosion defects). In some cases, in order to reproduce the fatigue crack properties, they are formed by cyclic loading in mechanical testing machines. For longitudinal cracklike defects the main parameters normalized during RS certification can be their depth, depth of occurrence for subsurface defects or inclination of the defect plane relative to the TO surface. For local defects, the normalized parameters are: depth, diameter, depth of occurrence or inclination relative to the controlled surface for subsurface defects.

By the number of values of the reproduced normalized defect parameter, the RS can be single or multi-valued (Figure 1). That is, RS can simulate one or several defects with different values of the normalized dimension. Multi-valued RS can reproduce discrete or continuous values of the normalized defect parameter in the range of its change. In terms of design the RS can be made as a monolithic specimen or they can be composed of two or more parts. Composite RS are most often used to simulate the subsurface defects [16–18].

Figure 2 shows a composite RS for simulation of subsurface defects in cylindrical TO. RS in Figure 2, *a* is made in the form of a layered cylinder with AD in the form of a cut along the cylinder generatrix in one of the layers [16]. The AD depth is assigned by selection of the thickness of a cylindrical layer with a through-thickness AD, and the depth of its occurrence is specified by selection of the outer layer thickness. Such an RS reproduces only one value of AD depth and one value of the depth of its occurrence, i.e. discrete values of AD parameters. It cannot simulate the AD differing by their depth and with different depth of their occurrence. For this purpose, it is necessary to create individual RS, which will simulate discrete values of the respective parameters.

More versatile is a composite RS in Figure 2, *b* in the form of eccentric bushings *1*, *2*, between which cylindrical bushing *3* with AD *4* is located [17]. By turning the bushing of such an RS it is possible to change the depth of AD occurrence in a certain range with the constant dimensions of AD and thickness of the cylindrical TO, i.e. this RS is a multi-valued measure of the depth of defect occurrence. Its disadvantage is the

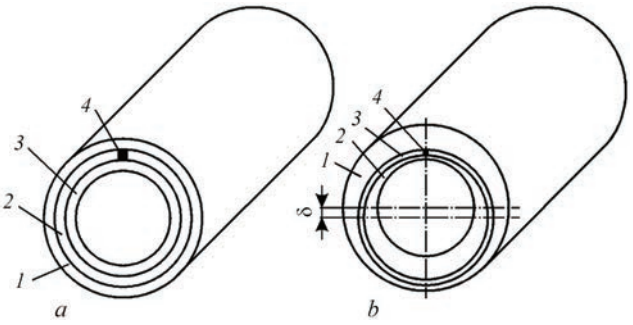

Figure 2. Single-valued discrete (*a*) and multi-valued (*b*) RS of composite type for simulation of the defects of the cylindrical TO: *1–3* — layers of cylindrical RS; *4* — AD; δ — eccentricity

complexity of manufacturing this RS, as to achieve a tight connection of the bushings, it is necessary to ensure their accurate dimensions along the entire specimen length. Otherwise, there will be gaps between the layers, which will influence the ECP signal.

Flaw detection RS can be classified according to their purpose, as they are designed to endure the testing validity by: 1) ECFD testing, certification and calibration; 2) setting up and periodical checking of ECFD operability for performance of a specific testing procedure; 3) selection of the testing modes during development of the procedure, taking into account the TO features and the factors creating interference (Figure 1). The procedures of ECFD testing, certification and primary calibration are an important stage of developing them, during which the metrological characteristics (predominantly, sensitivity threshold and resolution) are normalized. This stage is subject to metrological supervision by accredited institutions using RS, which have passed the respective metrological assessment. Such RS are proposed by the ECFD developer or the accredited institution, so they are often called primary. Checking of ECFD adjustment and its ability to perform the procedure of testing a particular product is conducted directly in the work place. Here, RS are used, which maximally reproduce the TO features. The parameters of AD of such defects are chosen, depending on the selected rejection criterion, which can differ from ECFD sensitivity threshold. These RS should simulate the features of the entire range of the factory TO, and in practice they are most often made by the companies operating the NDT means. Such RS are often defined as secondary RS. They are not always subject to metrological assessment and, in the best case they pass technical inspection for compliance with drawings. At the research stage the fundamental possibility to solve a new NDT task is determined, testing modes are selected (for instance, ECP type, operating frequency, etc) and the testing procedure is optimized, allowing for the TO design features. Here, RS are required

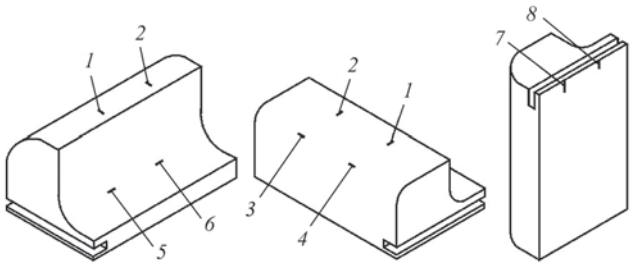

Figure 3. RS of SOP type with surface defects in the plane (*1*, *2*), convex (*3*, *4*), concave (*5*, *6*) and edge (*7*, *8*) sections

which completely reproduce the conditions of testing of a particular product (SEC, MP, availability of the coating, surface curvature, design features, etc.). These RS do not require metrological assessment, as they are not used after research is completed.

In order to implement the technologies of quantitative flaw detection with determination of the parameters of the detected defects, the metrological support (including approaches to RS selection) should change essentially. In today's practical work the ECFD are certified only using RS with AD, which characterizes the sensitivity threshold. For quantitative flaw detection it is necessary to develop RS, which reproduce AD parameters in the range of their change and to assess the error of their determination.

In reality, the conditions of the influence of a number of parameters changing the ECFD limit sensitivity are controlled. Strictly speaking, ECFD sensitivity threshold is a function of many parameters (for instance, the gap between ECP and TO surface, distance to TO edge, SEC and TO thickness). A methodologically correct approach would envisage normalizing these influences to assess the possibility of flaw detection in the real conditions. Such an approach, however, is not applied in practice, as it requires a large set of RS.

In practice, the simplest flat RS are used, with a slot made across their entire width, the depth of which corresponds to ECFD sensitivity threshold. Such an RS evaluates the sensitivity threshold only by depth. An essential drawback is the impossibility to establish ECFD sensitivity threshold only by the defect length. More over, the influence of the surface and edge curvature is not assessed. Better possibilities are provided by RS with surface defects, made from aluminium alloy D16 (SOP 5-1), titanium alloy VT3 (SOP 5-2) and ferromagnetic steel St45 (SOP 5-3), earlier used to fit ECFD of PROBA-5 type (Figure 1) [12]. Slots 2 mm long with up to 0.1 mm opening were made by electric spark method with 0.05 mm thick brass electrode. Slots 0.2 mm and 0.5 mm deep were made on the surface of RS from the aluminium alloy, slots 0.5 and 1.5 mm deep were cut in RS from the titanium alloy and steel. In addition to slots on RS flat surface (Figure 3, defects *1*, *2*), slots were made on the cylindrical convex (defects *3*, *4*) and concave (defects *5*, *6*) sections of 6 mm radius. In addition, two defects 0.5 and 1.0 mm long (defects *7*, *8*) were introduced on RS edge. Thus, such RS enable assessment of ECFD sensitivity by the depth and length of the surface AD on the flat and curvilinear surfaces in ferromagnetic steels and non-ferromagnetic materials with different SEC. A disadvantage of this RS is the complexity of manufacturing and high cost, making it impossible to fit every ECFD with them. Nonetheless, these RS were successfully used by us during state trials of eddy current autogenerator flaw detectors of LEOTEST VD type, which were conducted at SC "Dniprostandardmetrologia" (Dnipro city) [13].

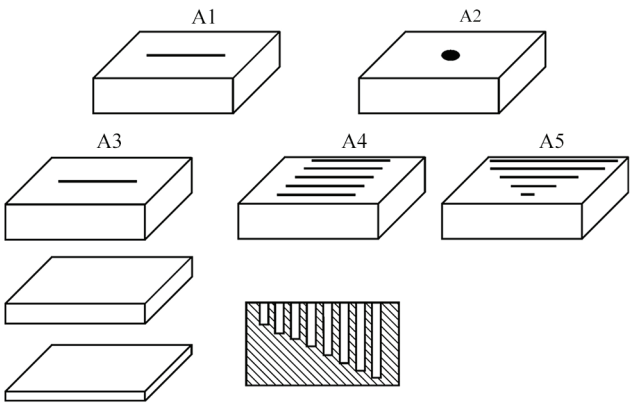

Figure 4. RS for checking the characteristics of put-on ECP in keeping with a European standard [5]

European standard on checking the ECP characteristics proposes the general requirements to RS, the set of which for testing the surface: ECP is given in Figure 4 [5]. Each of the RS should have the length and width minimum ten times greater than that of ECP sensitivity zone. If this characteristic is unknown, it should be replaced by the maximum (active) ECP size in the scanning plane. The distance from the slot to RS edge should be 2.5 times greater than the extent of the edge influence zone. RS thickness should be minimum two times greater than the standard penetration depth of eddy currents at ECP lowest operating frequency. More detailed requirements to each specific RS, in particular slot number, slot width and depth and hole diameter, should be specified in the testing procedure or operating documentation. To study the ECP signals from elongated defects RS of A1 type was proposed (Figure 4) with a slot in the central zone, which should be longer than the minimal length of the slot, exciting the maximal ECP signal, and deeper than the minimal depth of the surface slot, exciting the maximal ECP signal. To study ECP signals from local defects, RS of type A2 with a hole in the central zone was proposed. It is recommended that the hole depth is equal to that of the slot in block A1. RS set of type A3 is proposed to assess the

influence of thickness, in particular, effective depth of eddy current penetration. They are similar to specimen A1 without a slot with different thickness, increasing to three values of standard penetration depth or to two ECP active dimensions. This RS together with such of A1 type, is also used for determination of effective depth of subsurface defect detection. In keeping with the proposed classification a composite RS is used here, in which selection of plate thickness is used to simulate different TO thickness. To assess the influence of slot depth, in particular, to determine the minimal depth, exciting the maximal ECP signal, RS of type A4 are proposed (Figure 4). It is similar to A1 specimen, but it has a set of parallel slots, located in RS center. Here, all the slots have the same length and width (as in RS A1), and the depth is gradually increased with a constant step. The distance between two successive slots should be at least 5 times greater than the size of ECP sensitivity zone. RS of type A5 (4) were proposed to assess the influence of defect length on ECP signal, in particular, to determine the minimal length, ensuring a constant ECP signal. It is similar to specimen A1, but with a series of parallel slots, having the same depth and width as do the slots in specimen A1, but their length gradually increases with a constant step. The distance between the two successive slots should be at least 5 times greater than the dimensions of ECP sensitivity zone.

Let us remind you that in keeping with the European standards these RS are designed for ECP characterization, which is required to select the respective ECP to solve the defined task at the stage of development of the testing procedure, and not for ECFD metrological assessment. They enable determination of the minimal depth and length of the crack, generating the maximal ECP signal. They allow establishing the testing locality (by the sensitivity zone dimensions), studying the influence of ECP orientation relative to the crack, influence of TO thickness, etc. They however, do not provide evaluation of the resolution, which requires RS with defects located at different distance. The resolution in this case can only be assessed indirectly by the dimensions of the sensitivity zone. The European standard also envisages application of a composite RS, where the defect is simulated by a butt of two ground plates. This RS variant has traditionally been used to study ECP signals with different depth of occurrence, as well as to optimize the procedures of testing multilayered aircraft components.

MULTI-VALUED COMPOSITE RS FOR SIMULATION OF THE SURFACE AND SUBSURFACE DEFECTS IN CYLINDRICAL AND FLAT TO

Most of the known RS can be used only for surface defect simulation. Implementation of the technologies of detection and evaluation of hidden subsurface defects at low operating frequencies requires RS with AD, which have been additionally normalized by the depth of their occurrence. We proposed a multi-valued composite RS (Figure 5) to simulate surface and subsurface defects for rotary testing of cylindrical TO (V.M. Uchanin, V.L. Naida, I.I. Kyrychenko, O.M. Gogulya. Standard specimen for adjustment, calibration and certification of eddy current flaw detectors. Pat. of Ukraine No. 39172. Publ. 10.02.2009). RS for surface defect simulation consists of two cylindrical tubular parts *1* and *2* with outer diameter *D*, internal diameter *d* and wall thickness *T*. For simulation (Figure 5, *a*) one end of cylindrical tubular part *1* was treated on end section 3 of length *l* over the conical surface so that the outer diameter of end section *3* increased from the tube end along the length of section *l* at specified angle α° relative to cylinder surface. Part *2* of the specimen was treated on end section *4* of length *l* over the conical surface so that the internal diameter of end section *4* decreased from the tube end along the length of section *l* at the same angle α°. Both the RS parts are connected over the conical surfaces of end sections *3* and *4* so that they form a single cylinder. To simulate the surface cracklike defect, a thin through-thickness cut of length *l* and width *c* is made in the end conical section *4* of RS second part. As a

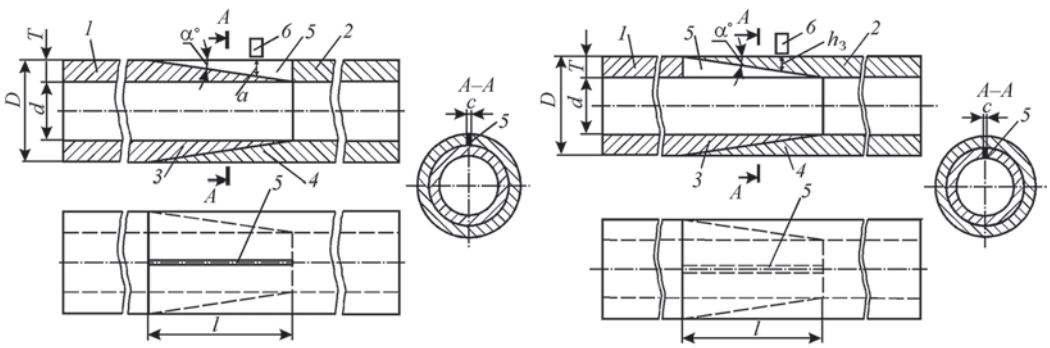

Figure 5. Composite RS for simulation of surface (*a*) and subsurface (*b*) cracklike defects in cylindrical TO: *1*, *2* — RS parts; *3*, *4* — conical end sections of RS part; *5* — defect on the outer (*a*) and inner (*b*) conical sections; *6* — ECP

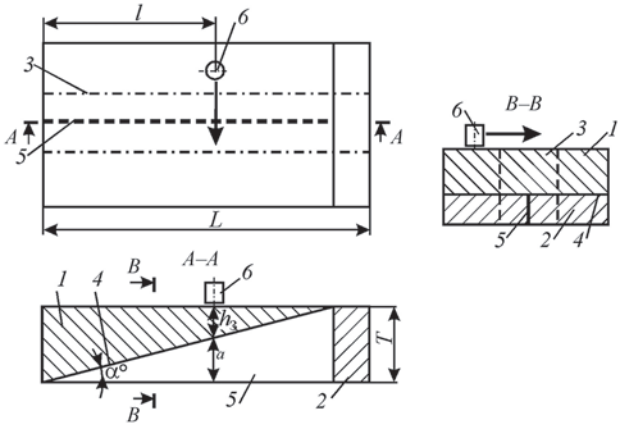

Figure 6. Composite multi-valued RS for simulation of surface and subsurface defects in flat TO with a weld: *1*, *2* — wedge-shaped parts; *3* — weld area; *4* — butt; *5* — AD; *6* — ECP

result, the RS simulates the surface defect, the depth of which *a* changes from 0 to *T*, depending on the position of rotary ECP along the RS (Figure 5, *a*).

To simulate a subsurface crack (Figure 5, *b*) a thin through-thickness cut of length *l* and width *c* is made in end conical section *3* of first part *1*. After joining the RS parts over conical surfaces *3* and *4* a subsurface defect of length *l* and width *c* is simulated, having variable depth of occurrence h_{occ} from 0 to *T*. To simulate a bulk local defect of pore type, holes of different diameter can be drilled out in RS end sections.

RS in Figure 5 are simple to produce and they simulate defects of different type and size, located at different distance from the TO surface. The defect depth or depth of its occurrence in the tested zone are determined by the position of rotary ECP *6* along RS defective section, so that this RS, in keeping with the classification (Figure 1) is a composite multi-valued one.

A composite multi-valued RS (Figure 6) was proposed to simulate subsurface defects of different depth and depth of occurrence in flat TO. It contains two wedge-shaped parts *1* and *2* having the same angle of inclination α (V.M. Uchanin, V.G. Rybachuk. Standard specimen for adjustment and certification of eddy current flaw detectors. Pat. of Ukraine No. 39189. Publ. 10.02.2009). RS parts are abutted in plane *4* so as to form a plate with plane-parallel surfaces. To simulate cracks, thin cut *5* is made in one of the wedge-shaped parts. The cut plane is normal to

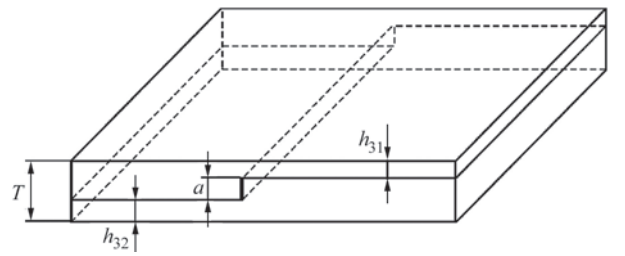

Figure 7. Composite RS for simulation of two discrete values of the depth of defect occurrence

butt plane *4* of wedge-shaped parts. When ECP is installed on RS surface, which belongs to wedge-shaped part *1* without a cut (Figure 6), a subsurface crack is simulated with variable depth of occurrence h_{occ} and variable depth *a*, which depend on distance *l* between the ECP and the RS edge of length *L*. When ECP *6* is installed on RS surface, which belongs to wedge-shaped part *2* with a cut, the AD simulates a surface crack. AD depth a changes, depending on distance *l* between the ECP and the RS edge. One can see from Figure 6 that depth of occurrence h_{occ} of the crack and its depth *a* depend on distance *l* between the ECP and the RS edge, according to relationships $a = l \cdot \mathrm{tg}\alpha$ and $h_{occ} = T - a = T - l \cdot \mathrm{tg}\alpha$. Changing ECP distance *l* from RS edge, we can simulate the surface and subsurface cracks of different depth and depth of occurrence in a certain continuous range of these parameter values. If required, a linear scale of the simulated parameter can be applied to the RS surface.

To simulate defects of the type of lacks-of-penetration in the welds, the RS wedge-shaped parts were produced from plates with a weld made in advance (dashed line in Figure 6). The direction of inclination of RS wedge-shaped parts coincides with that of the weld. AD in the form of a cut was introduced in wedge-shaped part *2* in the weld area.

There exist situations, when it is enough to simulate the discrete values of the defect parameter. In particular, in order to study the influence of the depth of defect occurrence, irrespective of its dimensions, it is possible to use RS, which simulates a defect of the same depth for two discrete values of the depth of occurrence (Figure 7) [19]. The two parts of the RS are put together so that after they are combined, a rectangular plate of thickness *T* formed with a subsurface defect of depth *a*. The defect is a butt of the two parts, normal to the specimen surface. The depths of defect occurrence h_{occ1} and h_{occ2} are different relative to different surfaces of the specimen, in keeping with relationship $h_{occ1} + h_{occ2} + a = T$. Two RS from D16T aluminium alloy 7 mm thick were made: one simulates a 2 mm deep crack, located at depths of 2 and 3 mm; and the other is a 2 mm deep crack located at depths of 1 and 4 mm.

Such a set of RS allows simulation of four values of the depth of occurrence of a defect of the same size, and studying the influence of the depth of its occurrence on ECP signal, irrespective of the plate size and thickness. ECP signals for these RS were studied using an eddy current board EDDYMAX. Figure 8 gives the signals of ECP of MDF 0801 type in a complex plane at operating frequency of 1 KHz. The gain for AD with the depth of occurrence h_{occ} = 1 and 2 mm was equal to 44 dB. For defects with h_{occ} = 3 and 4 mm (Figure 8, *c*, *d*) the gain was increased by 12 dB, con-

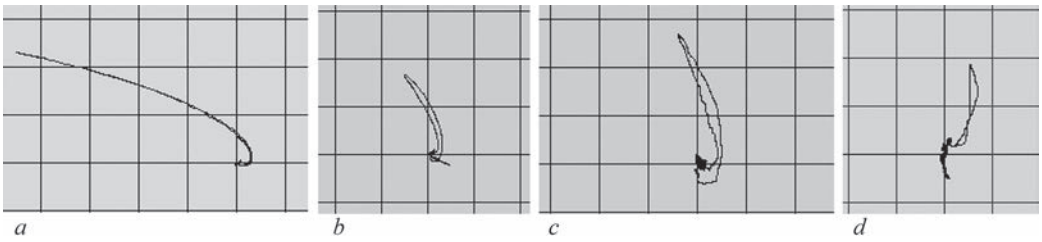

Figure 8. ECP signals from an extended cracklike defect with depth of occurrence h_{occ} (mm): 1 (*a*); 2 (*b*); 3 (*c*); 4 (*d*)

sidering the large difference in the amplitude of the signal for AD with different depth of occurrence.

The given results illustrate the principle of RS application (Figure 7) to determine the potential of eddy current method, in particular, for detection of cracklike defects of depth a = 2 mm, occurring in aluminium alloy products at up to 4 mm depth. One can see that at 1 kHz operating frequency the selected ECP provides a reliable detection of all the RS defects of 2 mm in-depth size, occurring at up to 4 mm depth in aluminium alloys. With increase of AD depth of occurrence, the ECP signal amplitude decreases essentially. Here, with increase of the depth of occurrence, the hodograph of ECP signal rotates clockwise, i.e. the phase of ECP signal changes, which should be taken into account during development of the testing procedure. The described set of composite RS was used to study and develop a procedure for detection of internal defects in multilayer aircraft structures and in welded joints of aluminium alloys.

MANUFACTURE OF RS FOR SIMULATION OF INCLINED DEFECTS

Most of the known RS can only be used to simulate surface defects, oriented normal to TO surface. This can be explained by that such defects are characteristic for the majority of structures, although known are cases of inclined crack formation, in particular, with contact interaction of surfaces during rolling [20]. In a few cases, RS with defects oriented at a specified angle to TO surface are required to detect and evaluate defects of different orientation. The known methods of producing RS do not allow introducing inclined AD with a specified angle of inclination, because when trying to introduce them thin mills are deformed and the cutting process becomes unstable, particularly at smaller (less than 60°) angles of the mill inclination relative to the surface. In order to create RS with inclined defects, a method of their production is proposed (V.M. Uchanin. A method to produce standard specimens for adjustment, calibration and certification of nondestructive testing instruments. Pat. of Ukraine No. 29293. Publ. 10.01.2008). In order to implement it, first a material is selected with electrophysical characteristics (SEC and MP) corresponding to TO, from which billet *1* is made (Figure 9). Wedge-shaped notch *2* is made on the billet surface, the side surface of which is inclined at angle φ relative to the billet surface. After that AD in the form of thin slot *3* is made by electric spark method or a thin mill on the notch side surface (Figure 9, *a*). Then, part of the billet together with the notch is removed along line *4* (Figure 9, *a*), forming the RS surface. The produced RS simulates a cracklike defect inclined at angle φ (Figure 9, *b*). Selection of angle φ, depth of the cut, made on the side surface of the notch, and the thickness of the removed layer of the billet allows simulating defects of different depth with different inclination relative to the surface. Using RS with inclined defects is important for investigation and optimization of eddy current procedures for quantitative evaluation of inclined crack parameters [21].

ANALYSIS OF THE POSSIBLE CAUSES FOR THE DIFFERENCE BETWEEN ECP SIGNALS FROM ARTIFICIAL AND NATURAL CRACKS AND INVESTIGATION OF THE INFLUENCE OF CRACK WIDTH ON ECP SIGNAL

The authors [22] believe that the natural cracks and AD in the form of thin slots create ECP signals close as to their characteristics. At the same time, a large number

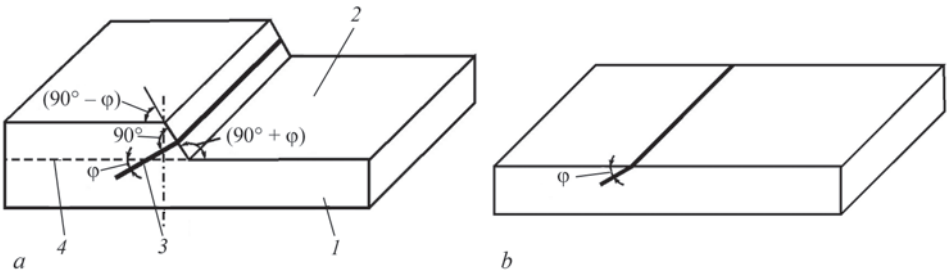

Figure 9. Scheme of implementation of the production method (*a*) of RS for simulating inclined cracks (*b*): *1* — billet; *2* — wedge-shaped notch; *3* — defect; *4* — line of notch removal

of works on this issue report a significant difference in the ECP signals from natural defects and AD [23–27]. Among the causes given to explain the possible discrepancies are: 1) presence of a plastic strain zone in the natural crack zone [23]; 2) greater value of AD opening, compared to a natural crack [24, 27]; 3) possibility of electric contact of the natural crack walls, unlike the AD, where the possibility of such a contact is absent [26]; 4) greater roughness of the natural crack fracture surface, unlike the AD, which has smoother walls [28]. Let us consider the differences in ECP signals from the natural defects and AD in greater detail.

Traditional models of ECP signal formation do not allow for changes in electrophysical parameters of the material in the zone of plastic strains, generated by the fatigue crack. In [23] the authors believe that the width of this zone is large enough, and it can be much greater than the volume of the crack proper. This leads to considerable changes of SEC and MP in the defect zone, which can influence the ECP signal. No experimental proof of such influence is given, however.

Greater roughness of the fatigue crack fracture surface, unlike the AD with smooth walls characteristic for electric-spark AD, also can be one of the causes for the difference in the signals. It is known that the rough surface of the fatigue crack is of a fractal nature [29–31]. In [28] the influence of the fractal nature of the natural crack fracture on ECP signal is considered. One of the variants of Koch surface is used as a simple model of crack fracture [32]. It is shown that increase of fractal dimension D of the natural crack fracture surface (D > 2), compared to the AD smooth surface dimension (D = 2) leads to an increase in electric resistance to eddy currents in the crack zone. However, no experimental proof of the significance of such an influence is given either.

In the majority of the works [24–27] it is shown on the base of experimental studies that the signals from AD are significantly higher than those from natural cracks. In [24], in particular, it is noted that the signal from AD can exceed 2–5 times the signal from the natural crack of the corresponding depth. It is shown that the signals from a natural crack have a higher variability, compared to those from AD, and that there also exists the dependence of discrepancy between the parameters of the signal from AD and from the natural crack on the operating frequency, when the difference between the ECP signals from natural defects and from AD becomes greater with the increase of operating frequency. The authors of these works assume that the main cause of the discrepancy between the signals from the natural defects and AD is the different opening of the defects, as the signals from the natural cracks with a small opening and the AD in the form of slots of a rather large width were compared. Note that the conducted experiments could have given erroneous results, as with the equal depth and length of the compared natural defects and AD a similar value of their width (opening) was not provided, because of the lack of the necessary specimens. To confirm this conclusion on the decisive influence of AD width on ECP signal, it is important to conduct the respective theoretical studies.

To study the influence of the defect width (opening), calculation of the hodographs of the signals of parametric ECP was performed by the method of volume integral equations [33–34] for a crack of the same depth and length with a change of its width. Signals from a crack 5 mm long and 1 mm deep located in a nonmagnetic halfspace with SEC of 20 MS/m at operating frequency of 1 MHz were studied. Winding of the studied ECP consisted of 20 turns 0.5 mm high with internal and outer radii of 0.45 and 0.55 mm, respectively. The obtained values of ECP impedance during its interaction with the defect were normalized relative to ECP impedance, in case of its mounting on a defectfree halfspace with SEC of 20 MS/m (R_{20} = 0.174 Ohm; X_{20} = 1.806 Ohm and L_{20} = 0.287 μH). All the geometrical parameters together with opening c were normalized relative to ECP mean diameter (1 mm). Calculations were performed for relative opening values c' from 0.01 to 2.4, that corresponds to possible opening of the natural and artificial defects. Note that the AD are most often made with up to 0.3 mm opening, which in our case corresponds to the reduced value c' = 0.3. Derived results (Figure 10) indicate that the ECP signal amplitude significantly depends on the crack opening. With its increase from 0.01 to 0.3 the amplitude increases by an order (from 0.0026 to 0.083), and the signal phase changes from 62 to 82°. With increase of the opening from 0.01 to 2.4 the signal amplitude increases by two orders (from 0.026 to 0.26), and the phase changes from 62 to 103°.

The obtained calculation results confirmed the conclusion about the decisive influence of the defect width on the difference in ECP signals from the natural defects and the AD. During preparation of RS simulating the fatigue cracks, it is important to make AD with a small opening. The advantage should be given to methods of swaging the RS with an artificial defect to reduce its width.

INVESTIGATIONS OF THE INFLUENCE OF THE CRACK LENGTH ON ECP SIGNAL

Investigations of the influence of the crack length on ECP signal have a methodological importance for determination of the conditions of reproducibility of

the testing results, when using the AD with cracklike defects. In metrology the reproducibility is a characteristic of measurement quality, which reflects the closeness of the results of measurement of one and the same value taken in different conditions [6]. Reproducibility is not less important for flaw detection, as it is a measure of comparability of testing results, derived at different locations by different flaw detection operators and testing means. Note that in addition to "reproducibility" term, a related term of repeatability is used in more recent documents. It reflects the similarity of measurement results under the conditions of repeatability, when independent test results were obtained by the same method on identical specimens in one laboratory and the same operator using the same equipment within a short time interval [35]. It is obvious that this term reflects the individual characteristics of the operator, in particular the level of his qualification.

The influence of crack length on ECP signal was studied in many works, which reported close results [36–41]. In [36] proceeding from the results of experimental studies on physical models of Wood alloy, it was mistakenly noted that the distribution of ECP signal from a long crack has two maximums in the zone of its ends in the absence of a central maximum, which is attributable to an insufficient accuracy of experimental investigations. It is obvious that the theoretical studies allow revealing the features, which can be overlooked during experimental investigations [37]. In [41] the investigations of ECP signal distribution were conducted in a broad range of the ratio of crack length to ECP diameter, their results being in good agreement with the research results of other authors [37–40]. In [41] a parametric ECP with one winding was studied during scanning of an electrically-conducting nonmagnetic TO with a crack in the form of a surface rectangular slot of length l_{CR}, depth a and width (opening) c ($l_{CR} >> a >> c$), located in the center of the system of coordinates, where coordinates X and Y correspond to the transverse and longitudinal directions relative to the crack, respectively. The changes in the amplitude of ECP signal Z_{CR} introduced by a crack were normalized relative to that of ECP impedance Z_{TO} in case of mounting on TO defectfree part: $Z'_{CR} = \Delta Z/Z_{TO}$. The geometrical parameters were normalized to ECP diameter D_c, i.e. the reduced crack length $l'_{CR} = l_{CR}/D_c$, and the reduced coordinate $y' = y/D_c$. Calculation of amplitude distribution along Y coordinate was conducted for an aluminium alloy with SEC σ = 20 MS/m at operating frequency of 1 MHz. Figure 11 gives the distribution of signal amplitude along the crack along its length by y coordinate for different ratios of the crack length to ECP

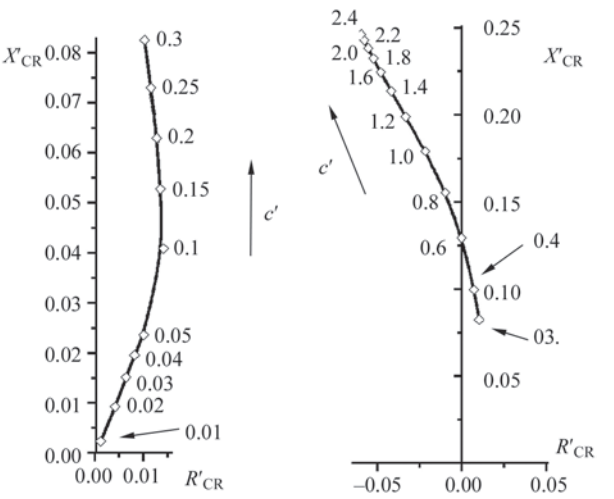

Figure 10. Hodograph of ECP signal from a crack, depending on its opening c' in the range from 0.01 to 0.3 (*a*) and from 0.3 to 2.4 (*b*)

diameter, namely: for short cracks with $l'_{CR} = 0.3$ (0) and $l'_{CR} = 1$ (●) and for long cracks with $l'_{CR} = 4$ (Δ) and $l'_{CR} = 5$ (▼). Obtained distributions of ECP signal amplitude in such a broad range of l'_{CR} thicknesses enable clearly emphasizing an essential influence of the crack length on the nature of spatial distribution of the amplitude of a signal from the crack. For short cracks the signal distribution has a two-hump symmetric character with a minimum at $y = 0$ (ECP over the crack center), which can reach zero for cracks of length $l'_{CR} < 0.3$. The ECP signal reaches its maximal value, when the short crack is located directly under the ECP turns in the zone of maximal eddy currents. The presence of two maximums for short cracks can be interpreted as signals from two separate defects. For long cracks, the distribution has one maximum, which corresponds to ECP position in the crack center. Further increase of the crack length from $l'_{CR} = 4$ will no longer influence the signal amplitude, as the distribution curves in this area actually coincide.

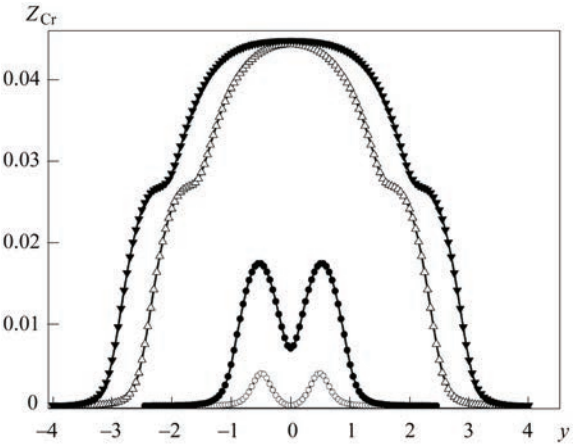

Figure 11. Distribution of the amplitude of a signal along the crack by coordinate y, depending on its length for short ($l'_{CR} = 0.3$ (0) and ($l'_{CR} = 1$ (●)) and long ($l'_{CR} = 4$ (Δ) and ($l'_{CR} = 5$ (▼)) cracks

Analysis of the given dependencies allows us to draw important conclusions as to selection of the crack length during RS development. Short cracks create a large variability of ECP signal during scanning of the crack zone. This makes it impossible to use RS with short cracks to assess the reproducibility or repeatability of the results of eddy current testing, as it is practically impossible to ensure the same conditions for result reproducibility during scanning of the crack zone by different flaw-detection operators. To assess the reproducibility or repeatability of test results, it is rational to use RS with long cracks, during the application of which a slight shifting will not have any significant influence on ECP signal. In this case, it is rational and much simpler to make RS specimens with a cracklike defect across the entire RS width.

At the same time, RS with short cracklike defects should be used to assess the sensitivity limit by the length of the cracks, which should be detected, in those cases, when it is important for the posed flaw detection task (see, for instance, RS in Figure 3).

PROCEDURE FOR STATIC ASSESSMENT OF REFERENCE STANDARD PARAMETERS

In order to create RS, it is possible to use natural defects, or defects formed during fatigue testing (Figure 1). The problem, however, lies in determination of the parameters of such defects, as they can be established with sufficient accuracy by direct measurements only after RS breaking up, when they are no longer suitable for metrological support of NDT instruments.

Known are the procedures of making the RS, where this contradiction is eliminated by studying the RS with breaking up of part of randomly selected specimens and assigning to the intact specimens the controlled parameter value determined by direct measurements [42]. The total number of the specimens and of those which are broken up is determined empirically, and the nominal value of the parameter is assigned to the intact specimens based on an unverified assumption of the homogeneity of the entire specimens. It is obvious that such a procedure is valid only when the scatter of the controlled parameter values is small for the majority of the specimens. In other cases, the controlled parameter value assigned to RS is insufficiently substantiated, as it can differ from the actual one with an undetermined error.

One of the possible variants of a comprehensive solution to the problem is application of a statistical approach, which was used for the first time to create RS for certification and verification of an instrument for measurement of the coefficient of charge filling in the flux-cored wire [43, 44], which was conducted in keeping with our invention (A.Ya. Teterko, O.L. Hodovnik, Yu.V. Pozdnyakov, V.N. Uchanin. A method for adjustment, calibration and verification of an instrument for controlling the flux-cored wire filling with the charge. USSR Auth. Cert. No.1569694. Publ. 07.06. 90). Furtheron a statistical method of RS certification and calibration was developed for other NDT problems, in particular those of flaw detection (V.N. Uchanin, Yu.V. Pozdnyakov, Yu.N. Agapov. A method to produce a measure for calibration of non-destructive testing instruments. USSR Auth. Cert. No. 1753394. Publ. 0.7.08.02). The proposed statistical approach provides assessment of the error of determination of the controlled parameter of intact RS, which were left for use, as it is based on the possibility of application for RS evaluation of a working NDT device which should be calibrated. Note that in flaw detection the defect depth most often in the controlled parameter. For eddy current flaw detection RS with fatigue cracks the proposed procedure can be presented as a sequence of the following operations [45]:

1) At the first stage a set of N specimens is selected which themselves can be the tested products proper or their fragments with natural cracks. The material and geometrical parameters of the selected specimens should be the same. During production of RS with cracks by the fatigue testing method it is desirable to select specimens with the same number of the loading cycles. The sufficient for the group N number of the specimens can be determined in advance, analyzing the scatter of the controlled parameter for specimens of this type.

2) At the next stage an ECFD is used, from which only a certain correlation between the output signal parameters and the controlled parameter of the crack is required (for instance between the signal amplitude and the crack depth). The operating frequency is selected to be such that there exists a dependence of the signal on the crack parameter (for instance, depth) in the specified range of change. RS with AD can be used for this purpose.

3) The selected specimens are controlled using the prepared ECFD and its readings are recorded for each specimen. After that the specimens are organized, arranging them in the order of increasing ECFD readings.

4) The first group of the controlled parameter (crack depth) is formed. For this purpose, W specimens are selected from the initial set N of the specimens, for which the values of instrument readings are close to minimal values. This is enough for the majority of indicator-type ECFD. For quantitative testing groups of specimens having medium and maximal ECFD readings in the range of change are formed similarly. In case of a large dispersion of the values of instrument

readings it is necessary to increase (for instance, double) the size of the specimen primary sample until W similar specimens are obtained for each group from the studied number of specimens.

5) Then, Q out of W specimens are selected randomly from each group, actual values X of the controlled of the parameter defect (depth) are determined by direct methods (for instance, using a measurement microscope) after their breaking up.

6) The estimate of the mathematical expectation of the studied parameter (depth) for each group of similar specimens is calculated by the following formula:

$$W_{ik} = 1/Q\sum_{k=1}^{Q} X_{ik}$$

where i — is the group number; $k = 1, \ldots, Q$.

This estimate is taken as the actual value of the controlled parameter, reproduced by each group measure. After that, the value of mathematical expectation is assigned to the respective RS of the group based on the earlier established homogeneity of the specimens included into it.

Any of the intact specimens can be used for ECFD adjustment. For instrument calibration in the middle and at the end of the range RS of the respective group are used. The main error of the instrument in the calibration points is determined, mainly, by the error of each of the groups, which should be understood to mean the error of the groups reproducing the values assigned to them. This error can be assessed through the error of verification of a group, preliminarily evaluated by accurate direct methods. Significant factors, determining this error, are the accuracy of the direct measurements, number of specimens, making up the group, and degree of their identity by the controlled parameter. The proposed procedure of statistical assessment was used with success during evaluation of RS with fatigue cracks in tubular specimens [45].

CONCLUSIONS

We developed a methodology of metrological support of eddy current flaw detection means using RS. In particular, a classification of RS with artificial defects is proposed and respective examples are given, which confirm the validity of the proposed classification. Given as an example are the designs of composite multi-valued RS for simulation of the surface and subsurface defects in the cylindrical and flat TO. Also presented is the design of a composite RS and the respective set of RS simulating the subsurface crack of the same size with four values of its location depth, and the respective signals of double differentiation ECP are studied experimentally. A method to produce RS for simulation of inclined cracks is proposed. A range of works are analyzed, which consider the possible causes for the difference in ECP signals from a natural crack and AD. Calculations by the method of volume integral equations were used to show that the main cause for the difference in ECP signals from the natural fatigue defects and AD is their width (opening). The influence of crack length on the features of the signal from parametric type ECP is considered, which should be taken into account during selection of RS parameters as regards crack length. A statistically substantiated method of valid evaluation of the parameters of RS with natural defects is presented, which was successfully used to assess tubular specimens with fatigue cracks.

REFERENCES

1. Polishchuk, E.S., Dorozhovets, M.M., Yatsuk, V.O. et al. (2003) *Metrology and measuring equipment*. Lviv, Beskyd Bit [in Ukrainian].
2. Mykytyn, G.V. (2000) Peculiarities of metrological support of non-destructive testing. *Visnyk Ternop. DTU*, 5(**3**), 76–80 [in Ukrainian].
3. Petryk, V.F., Protasov, A.G. (2015) *Metrology, standardization and certification in non-destructive testing*. Kyiv, NTUU KPI [in Ukrainian].
4. Udpa, S.S., More P.O., et al. (2004) *Nondestructive testing handbook*. 3rd Ed. Vol. 5, Electromagnetic Testing, American Society for NDT.
5. EN ISO 15548-2:2013. Non-destructive testing — Equipment for eddy current examination. Pt 2: Probe characteristics and verification (ISO 15548-2:2013).
6. Shevchenko, O.I. (2022) *Metrology. Terms and explanations*. Kyiv, VAITE [in Ukrainian].
7. Solomakha, R., Uchanin, V. (2024) Magnetic hysteresis analysis for non-destructive evaluation of aircraft structural steels. *Transact. in Aerospace Research,* 276(**3**), 1–12. DOI: http://doi.org/10.2478/tar-2024-0013
8. Uchanin, V.M., Ostash, O.P., Bychkov, S.A. et al. (2021) Eddy current monitoring of aluminum alloy degradation during long-term operation of aircraft. *The Paton Welding J.,* **8**, 45–51. DOI: http://doi.org/10.37434/tpwj2021.08.09
9. *On metrology and metrological activities*. Law of Ukraine dated 5.06.2014, No. 1314-VII (as amended) [in Ukrainian].
10. ISO/IEC Guide 99:2007. *International vocabulary of metrology — Basic and general concepts and associated terms* (VIM).
11. Dorofeev, A.L., Kazamanov, Y.G. (1980) *Electromagnetic defectoscopy*. Moscow, Mashinostroenie [in Russian].
12. Bilik, Y.Z., Dorofeev, A.L. (1981) Electromagnetic flaw detectors of the Proba type. *Defectoscopiya*, **6**, 53–58 [in Russian].
13. Uchanin, V.M., Bychkov, S.A., Semenets, O.I. et al. (2022) Self-generator eddy current flaw detectors for operational control of aircraft structures. *Tekh. Diahnost. ta Neruinivnyi Kontrol*, **3**, 22–29 [in Ukrainian]. DOI: https://doi.org/10.37434/tdnk2022.03.04
14. McMaster, R.C. McIntire, P. et al. (1986) *Nondestructive Testing Handbook*. Vol. 4: Electromagnetic Testing (Eddy current, flux leakage and Microwave Nondestructive Testing). 2nd Ed. USA, American Society for NDT.
15. Uchanin, V. (2024) Detecting and estimating local corrosion damages in long-service aircraft structures by the eddy current method with double-differential probes. *Transact. on Aerospace Research,* 275(**2**), 20–32. DOI: https://doi.org/10.2478/tar-2024-0009
16. Kosovsky, D.Y., Shkarlet, Y.M., Khvatov, L.A. et al. *Simulator for setting defectoscopes*. USSR Auth. Cert. 739391, Inc. Cl. G 01 N 27/86. Publ. 06.05.80 [in Russian].

17. Vyakhirev, V.G., Nikulshin V.S., Oleinikov P.P. *Simulator for setting up electromagnetic flaw detectors*. USSR Auth. Cert. 926586, Int. Cl. G 01 N 27/90. Publ. 07.05.82 [in Russian].
18. Vyakhirev, V.G., Nikulshin, V.S., Oleinikov, P.P. *Tuning simulator for eddy current defectoscopes (its variants)*. USSR Auth. Certificate 1006992, Int. Cl. G 01 N 27/90. Publ. 23.03.83 [in Russian].
19. Mook, G., Uchanin, V., Lysenko, Ju. (2024) Studies of eddy current probes for inspection of aluminum alloy structure welds using smartphone-based flaw detector. *The Paton Welding J.,* **12**, 42–48. DOI: http://doi.org/10.37434/tpwj2024.12.07
20. Datsishin, O.P., Marchenko, G.P., Panasyuk, V.V. (1994) Theory of crack growth in rolling contact. *Mater. Sci.,* 29(**4**), 373–383. DOI: https://doi.org/10.1007/BF00566446
21. Uchanin, V.M. (2025) Specific features of double-differentiation eddy current probe signals from inclined cracks. *Physicochemical Mechanics of Materials*, 61(**2**), 139–144. DOI: https://doi.org/10.15407/pcmm2025.02.139
22. Hagemaier, D.A., Register, J.A. (1990) Mock eddy current demonstration: Cracks versus notches. *Materials Evaluation*, **48**, 50–54.
23. Teterko, A.Ya., Nazarchuk, Z.T. (2004) *Selective eddy current flaw detection*. Lviv, PMI [in Ukrainian].
24. Rummel, W.D., Moulder, J.C., Nakagawa, N. (1991) The comparative responses of cracks and slots in eddy current measurements. *Review of Progress in Quantitative Nondestructive Evaluation*, **10A**, Eds by D.O. Thompson and D.E. Chimenti, Plenum Press, New York, 277–283.
25. Hartman, J. (1991) Correlation of eddy current response from EDM notches and tight fatigue cracks in ferromagnetic space shuttle RSRM components. *Review of Progress in Quantitative Non-Destructive Evaluation,* **10A**, Eds by D.O. Thompson, D.E. Chimenti. Plenum Press, New York, 285–290.
26. Beissner, R.E. (1994) Slots vs. cracks in eddy current NDE. *J. of Nondestructive Evaluation,* 13(**4**), 175–183. DOI: https://doi.org/10.1007/BF00742583
27. Randle, W.R, Woody, B.D. (1991) Caution about simulated cracks in steel for eddy current testing. *Materials Evaluation*, **1**, 44–48.
28. Uchanin, V.M., Zhenirovs'kyi, M.I. (2008) Effect of the relief of crack surface on the signal of an eddy current converter. *Mater. Sci.,* **44**, 274–277. DOI: https://doi.org/10.1007/s11003-008-9060-8
29. Usov, V.V., Shkatuliak, N.M. (2005) Fractal nature of brittle metal fractures. *Fiz.-Khimich. Mekhanika Materialiv*, **1**, 58–62 [in Ukrainian].
30. Barenblatt, G.I., Botvyna, L.R. (1986) Similarity methods in the mechanics and physics of destruction. *Fiz.-Khimich. Mekhanika Materialiv*, **1**, 57–62 [in Russian].
31. Ivanova, V.S., Balankin, A.S., Bunin, I.Zh., Oksagoev, A.A. (1994) *Synergetics and fractals in materials science*. Moscow, Nauka [in Russian].
32. Grynchenko V.T., Matsypura V.T., Snarsky A.A. (2005) *Introduction to nonlinear dynamics. Chaos and fractals*. Kyiv, Naukova Dumka [in Russian].
33. Dunbar, W.S. (1985) The volume integral method of eddy current modeling. *J. of Nondestructive Evaluation*, 5(**1**), 9–14. DOI: https://doi.org/10.1007/BF00568758
34. Sabbagh, H.A., Murphy, R.K., Sabbagh, E.H., Aldrin, J.C., Knopp, J.S. (2013) *Computational electromagnetics and model-based inversion — A modern paradigm for eddy-current nondestructive evaluation*. New York, Springer.
35. DSTU GOST ISO 5725-1:2005: *Accuracy (trueness and precision) of measurement methods and results.* Pt 1. Basic provisions and definitions. Kyiv, Derzhspozhyvstandart [in Ukrainian].
36. Beda, P.Y., Vybornov, B.Y., Glazkov, Y.A. et al. (1976) *Non-destructive control of metals and products:* Handbook. Ed. by G.S. Samoilovich. Moscow, Mashinostroenie [in Russian].
37. Beda, P.I. (1970) Investigation of the signal of an overhead sensor in relation to changes in the size and location of crack-type defects. *Defectoscopiya*, **1**, 62–68 [in Russian].
38. Beda, P.I., Putnikov, Y.G. (1994) Modeling of overhead transducer signals caused by a planar defect of arbitrary shape. *Defectoscopiya*, **2**, 19–26 [in Russian].
39. Auld, B.A., McFetridge, G., Riaziat, M., Jefferies S. (1985) Improved probe-flaw interaction modeling, inversion processing, and surface roughness clutter. Eds by D.O. Thompson, D.E. Chimenti. *Review of Progress in Quantitative Nondestructive Evaluation*, **4A**, 623–634. DOI: https://doi.org/10.1007/978-1-4615-9421-5_69
40. Moulder, J.C., Gerlitz, J.C. (1986) Semi-elliptical surface flaw EC interaction and inversion: Experiment. *Review of Progress in Quantitative Nondestructive Evaluation*, **5A**, 395–402.
41. Uchanin, V.M. (2007) Specific features of the space distribution of the signal of an eddy-current converter caused by cracks of different lengths. *Mater. Sci.,* **43,** 591–595. DOI: https://doi.org/10.1007/s11003-007-0068-2
42. Dorofeev, A.L., Nikitin, A.I., Rubin, A.L. (1969) *Induction thickness measurement*. Moscow, Energiya [in Russian].
43. Pokhodnya, I.K., Shlepakov, V.N., Maksimov, S.Yu., Ryabtsev, I.A. (2010) Research and developments of the E.O. Paton Electric Welding Institute in the field of electric arc welding and surfacing using flux-cored wire (Review). *The Paton Welding J.,* **12**, 34–42.
44. Panasyuk, V.V., Teterko, A.Ya., Pokhodnya, I.K. et al. (1975) Continuous control of the filling of a flux-cored wire charge in the process of its manufacture. *Avtomaticheskaya Svarka*, **5**, 48–49 [in Russian].
45. Uchanin, V.N., Ostash, O.P. (2002) Tubular samples for complex evaluation of heat exchanger tube material by fracture mechanic and nondestructive test methods. In: *Proc. of 8th Europ. Conf. on NDT, Barcelona*. www.ndt.net

ORCID
V.M. Uchanin: 0000-0001-9664-2101

CORRESPONDING AUTHOR
V.M. Uchanin
G.V. Karpenko Physico-Mechanical Institute of the NASU
5 Naukova Str., 79060, Lviv, Ukraine.
E-mail: vuchanin@gmail.com

SUGGESTED CITATION
V.M. Uchanin (2025) Methodology of using standard specimens with defects for eddy current inspection: Classification, typical examples, signals research and statistical method for parameters assessment. *The Paton Welding J.*, **10**, 36–48.
DOI: https://doi.org/10.37434/tpwj2025.10.06

JOURNAL HOME PAGE
https://patonpublishinghouse.com/eng/journals/tpwj

Received: 03.06.2025
Received in revised form: 15.08.2025
Accepted: 18.10.2025